The Density and Velocity Fields of the Local Universe.

by

Luís Filipe Alves Teodoro

A thesis presented for the degree
of Doctor of Philosophy

Department of Physics
University of Durham
Durham DH1 3LE
England

1999

ABSTRACT

Reconstructing the Cosmic Density and Velocity Fields

Luís Filipe Alves Teodoro

We present two self–consistent non-parametric models of the local cosmic velocity field based on the density distribution in the *PSCz* redshift survey of *IRAS* galaxies. Two independent methods have been applied, both based on the assumptions of gravitational instability and linear biasing. They give remarkably similar results, with no evidence of systematic differences and an *r.m.s* discrepancy of only ~ 70 km s^{-1} in each Cartesian velocity component. These uncertainties are consistent with a detailed independent error analysis carried out on mock *PSCz* catalogues constructed from N-body simulations. The denser sampling provided by the *PSCz* survey compared to previous *IRAS* galaxy surveys allows us to reconstruct the velocity field out to larger distances. The most striking feature of the model velocity field is a coherent large–scale streaming motion along a baseline connecting Perseus–Pisces, the Local Supercluster, the Great Attractor, and the Shapley Concentration. We find no evidence for back-infall onto the Great Attractor. Instead, material behind and around the Great Attractor is inferred to be streaming towards the Shapley Concentration, aided by the expansion of two large neighbouring underdense regions. The *PSCz* model velocities compare well with those predicted from the 1.2-Jy redshift survey of *IRAS* galaxies and, perhaps surprisingly, with those predicted from the distribution of Abell/ACO clusters, out to $140\,h^{-1}$Mpc. Comparison of the real-space density fields (or, alternatively, the peculiar velocity fields) inferred from the *PSCz* and cluster catalogues gives a relative (linear) bias parameter between clusters and *IRAS* galaxies of $b_c = 4.4 \pm 0.6$. In addition, we compare the cumulative bulk flows predicted from the *PSCz* gravity field with those measured from the *Mark*III and SFI catalogues of peculiar velocities. A conservative estimate of $\beta = \Omega_0^{0.6}/b$, where b is the bias parameter for *IRAS* galaxies, gives $\beta = 0.76 \pm 0.13$ $(1\text{–}\sigma)$, in agreement with other recent determinations.

Finally, we perform a detailed comparison of the *IRAS PSCz* and 1.2-Jy spherical harmonic coefficients of the density and velocity fields in redshift space. Both the monopole terms of the density and velocity fields predicted from the surveys show some inconsistencies. The mismatch in the velocity monopole terms is resolved by masking the 1.2-Jy survey with the *PSCz* mask and using the galaxies within the *PSCz* survey for fluxes larger than 1.2 Jy. Davis, Nusser and Willick (1996) have found a discrepancy between the *IRAS* 1.2-Jy survey gravity field and the *Mark*III peculiar velocity field. We conclude that the use of the deeper *IRAS PSCz* catalogue cannot alone resolve this mismatch.

Declaration

This thesis is the result of research carried out between October 1992 and October 1998. The work presented in this thesis has not been submitted in fulfilment of any other degree or professional qualification.

The work in Chapters 3, 4 and 5 was undertaken in collaboration with Dr. E. Branchini, Prof. C. S. Frenk and Inga Schmoldt. However the majority of the material presented here is the author's own work.

A number of results presented here have been accepted from publication in the following papers:

I. Schmoldt, E. Branchini, L. Teodoro, G. Efstathiou, C.S. Frenk, O. Keeble, S. Maddox, S. Oliver, M. Rowan-Robinson, W. Saunders, W. Sutherland, H. Tadros, S.D.M. White, 1999, MNRAS, accepted

E. Branchini, L. Teodoro, C. S. Frenk, I. Schmoldt, G. Efstathiou, S. D. M. White, W. Saunders, M. Rowan-Robinson, O. Keeble, H. Tadros, S. Maddox, S. Oliver, W. Sutherland, 1999, MNRAS, accepted

Acknowledgedments

It is a pleasure to thank my supervisor, Prof. Carlos S. Frenk, for his encouragement throughout the course of this work and for sharing with me his expertise from which I have greatly benefited.

Thanks are also due to Drs. Enzo Branchini and Shaun Cole for stimulating and endless discussions during this research.

I would like to express my gratitude to my parents, sister and brother-in-law for their support, my girlfriend, Gillian Telfer, who makes me dream about the impossible, Gustavo Marques and Sérgio "Mendes" who shared with me their love for life and perished during my stay in Durham, and to my friends who have made my life in the U.K. so enjoyable, particularly Roberto Pinheiro, João Prata, Marcos Sampaio, Affonso and Tesesa Brod, Ricardo Alves, Caroline Silva, Rafael Cabanès, Rui and Conceição Neves, Fernando Fernandez, Vincent Eke, Piotr Zycki, Ben Moore, Adrian Jenkins, Carlton M. Baugh, Andrew Ratcliffe, Roger Haynes, Istvan Szapudi and Dimitrios Saltouros.

Finally, I wish to thank J.N.I.C.T. – Junta Nacional de Investicação Científica e Tecnológica, for providing the financial resources to permit this research in the first place.

Dedicated to my parents and Gillian Telfer

Contents

Chapter 1

Introduction

One of the main challenges in developing Cosmology is to understand how small density fluctuations at the recombination epoch have become the intricate hierarchy of galaxies, clusters and superclusters that we observe in the nearby universe.

Despite the growing sophistication of theoretical models and the growing body of observational data, it has been rather difficult to judge the validity of most cosmological models in a definitive way. The major difficulty lies in the fact that theories predict the distribution of dark matter rather than galaxies. Only recently it was possible to gather reliable data extending over all regions of space. The Infrared Astronomical Satellite (*IRAS*) flew in 1983 and because the Galaxy is transparent to the infrared radiation this satellite was able to survey the entire sky.

This thesis focuses on ways of probing the density and velocity fields of the Local Galactic neigbourhood. Specific questions addressed include the following:

- Are the methods employed to reconstruct the *IRAS PSCz* density and velocity fields free of systematic errors? If so, what is their accuracy?
- What are the *IRAS PSCz* redshift survey reconstructed velocity and density fields?
- Are these fields analogous to that predicted by the *IRAS* 1.2-Jy redshift survey?

In this thesis, we will do the following:

Chapters 1 and 2 put the results obtained in this thesis in a larger context. Thus, we review the basics of modern cosmology in § 1 and the different reconstruction schemes in § 2.

In § 3 we examine the methods that we will apply in the reconstruction of the *IRAS PSCz* survey overdensity and velocity fields. To access the reliability of these methods we use mock catalogues extracted from N-body simulations. These mock catalogues mimic

both the mass and the galaxy distribution of the Local Universe. Comparing the real density and velocity fields measured from the N-body simulations with that measured from the reconstructions allows us to quantify the systematic and random errors intrinsic to these techniques.

In § 4, we present two new non-parametric models for the cosmic velocity field based on the recently completed *PSCz* survey of *IRAS* galaxies. A cosmographic tour is performed along with a consistency check between the two *PSCz* velocity models and a comparison between the *PSCz* and 1.2-Jy model velocity fields. We also take advantage of the large depth of the *PSCz* survey to compare the gravity field derived from it with the one derived from the distribution of Abell/ACO clusters. The parameter $\beta \simeq \Omega_0^{0.6}/b$, where b is the linear bias parameter of *IRAS* galaxies and Ω_0 the mean mass density parameter, is obtained by comparing observed and predicted bulk velocity vectors.

In § 5, we present a scheme to compare surveys with different depth and perform a detailed comparison between the spherical modes of the density and velocity fields of the two *IRAS* surveys. Although we find that some discrepancies in the monopole components of the density and velocity the fields predicted from both surveys are consistent.

These chapters are all self-contained and fairly independent, so they can be read in any order.

1.1 Where to read the basics

The basics of modern cosmology can be found in several excellent books. Three early classics are:

- *Gravitation and Cosmology* by Weinberg (1972)
- *Physical Cosmology* by Peebles (1980)
- *Relativistic Astrophysics Vol II* by Zel'dovich and Novikov (1983)

More recent textbooks include

- *The Early Universe* by Kolb and Turner (1990)
- *Structure Formation in the Universe* by Padmanabhan (1993)
- *Cosmology. The origin and evolution of cosmic structure* by Coles & Lucchin (1995)

Conference proceedings

- *Vatican Study Week: Large Scale Motions in the Universe*, edited by Rubin & Coyne (1988)
- *Physics of the Early Universe*, edited Peacock, Heavens and Davies (1990) (see especially the articles by Efstathiou and White),
- *Cosmology and large scale structure*, edited Schaeffer, Silk, Spiro and Zinn-Justin (1996) (see especially the articles by Efstathiou, Bertschinger and White)

1.2 General Relativity and the FRW Metrics

The Standard Hot Big Bang model relies on the assumption that the observable part of the universe can be approximated as part of a homogeneous and isotropic background model on large scales. The assumption of homogeneity and isotropy is often called the *Cosmological Principle*. To this principle we add General Relativity theory to describe the evolution and structure of the space-time. The present paradigm is that we live in a perturbed expanding Friedmann-Robertson-Walker universe in which the perturbations of the metric are small within our horizon. By this we do not mean that the density fluctuations are necessarily small.

The Standard model is supported by three main observations: a) the Hubble flow of galaxies. b) the isotropy of the electromagnetic radiation at wavelengths in the range from millimetres to centimetres, c) the prediction of the existence of an epoch in which the universe was hot enough to allow the nucleosynthesis of the light elements (Wagoner 1973). The predicted abundance are in accordance with the observation (*cf.* Walker 1991)

1.2.1 Friedmann–Robertson–Walker Metric

In General Relativity (GR) events in space-time are labelled by four coordinates $x^\mu = (t, \mathbf{r})$, $x^0 = ct$ (throughout this chapter $c \equiv 1$) and x^1, x^2, x^3 are the space coordinates. The line element ds connecting two events x^μ and $x^\mu + dx^\mu$ is defined by

$$ds^2 = g_{\mu\nu} dx^\mu dx^\nu, \tag{1.1}$$

where repeated suffixes imply summation. $g_{\mu\nu}$ is called the *metric tensor* and describes the space-time geometry. We adopt the convention that the signature of the metric is $(+---)$. If $ds^2 = 0$, the interval is *lightlike*, this means that the two points x^μ and $x^\mu + dx^\mu$ can be connected by a light ray. If $ds^2 > 0$, the interval is termed *timelike* where $|ds^2|^{1/2}$ would be the interval measured by a clock which moves freely between x^μ and $x^\mu + dx^\mu$. If $ds^2 < 0$, then the interval is *spacelike* and $|ds^2|^{1/2}$ represents the length of a ruler with ends at x^μ and $x^\mu + dx^\mu$ measured by the observer at rest with respect to the ruler.

On large scales the universe does not have any privileged position or direction. In cosmology this is known as *Cosmological Principle.* Through a cumbersome but straightforward calculation it is possible to show (*cf.* Weinberg 1972) that for coordinate systems describing isotropic and homogeneous universes the line element takes the simple form:

$$ds^2 = dt^2 - a^2(t)\left\{\frac{dr^2}{1-kr^2} + r^2 d\theta^2 + r^2 \sin^2\theta d\phi^2\right\}. \tag{1.2}$$

where we have used spherical coordinates r, θ and ϕ (called comoving coordinates); while the *expansion factor* $a(t)$ is an unknown function of time to be determined later and the constant k is the *curvature parameter* which can be scaled in such way that takes only the values -1, 0, 1.

The Hubble Law

By definition, the physical or proper distance, d_{ph}, between a point P and another P_0 which we take as the origin of our coordinate system (without loss of generality), at some time t, equals

$$d_{ph} = a(t)\int_0^r \frac{dr'}{\sqrt{(1-kr'^2)}} = a(t)f(r).S \tag{1.3}$$

This is the distance measured by a chain of rulers held by observers which connect P to P_0. From eqn. (1.3) we can notice that the proper distance changes with time. Thus objects that are at fixed comoving coordinates increase their physical separation, the time-dependence of all physical distances scaling as $a(t)$. Hence the radial velocity v_r of a source at P is given by

$$v_r = \frac{\dot{a}}{a} d_{ph} = H(t) d_{ph}, \tag{1.4}$$

where $H(t)$ is called *Hubble constant.* Its present value is $H_0 = 100\ h\,\mathrm{km\,s^{-1}\ Mpc^{-1}}$, h almost certainly lies between 0.5 and 1.0. Here and throughout this thesis, the subscript zero on a variable denotes its present value.

The Cosmological Redshift

Let us consider a packet of electromagnetic radiation emitted from a distant source in a definite direction. At time t such a packet passes a comoving observer who measures the wavelength of the radiation to be $\lambda(t)$. At $t + \delta t$ the same packet passes a second observer at a physical distance $d_{pr} = \delta t$ (recall that $c \equiv 1$) away from the first. As already shown in eqn. (1.4) the second observer is moving away from the first at speed $v_r = H d_{pr} = (\dot{a}/a)\delta t$. This implies that the measured frequency will be Doppler shifted and the wavelength increased to

$$\lambda(t+\delta t) = \lambda(t)(1+v_r) = \lambda(t)\left[1 + \left(\frac{\dot{a}}{a}\delta t\right)\right]. \tag{1.5}$$

In expanding the left hand side of this equation to first order in t we obtain a differential equation which when integrated gives

$$\lambda(t) \propto a(t). \tag{1.6}$$

Thus for a universe in expansion, $\dot{a} > 0$, objects moving with the cosmological expansion have their emitted light 'stretched out' towards larger wavelengths. Astronomers define *redshift* z of an object as

$$z = \frac{\lambda(t_o) - \lambda(t_e)}{\lambda(t_e)} \tag{1.7}$$

where t_e and t_o are the time of emission and observation of the objects light signal, respectively. In Cosmology redshift can be often used as a time variable. This is mainly because z corresponds much more directly to what the astronomers actually measure. When we look into the space, we are observing the past.

The Curvature of the space-time

For a given time t the hypersurfaces in the space-time have different geometries according to the value of k (*cf.* eqn. 1.2). Let us choose three points $\mathbf{x}_1$, $\mathbf{x}_2$ and $\mathbf{x}_3$ for a fixed t and connect them in a triangle by three curves of minimum length, the sum of the three internal angles will be smaller than 180° for $k = -1$, equal to 180° if $k = 0$ and greater than 180° for $k = 1$. For $k \leq 0$ the vector $\mathbf{r}$ is allowed to range over the entire space, the space is infinite at all times[1]. If $k = 1$ the hypersurface has the topology of a 3-sphere, the coordinate r is restricted to assume values smaller than 1. In this case the universe is said to be closed and its volume is finite at any time (Weinberg 1972).

The Friedmann Equation

The simplest realization of the stress-energy tensor $T^{\mu\nu}$ consistent with the homogeneity and isotropy of the space-time is that of a perfect fluid:

$$T^{\mu\nu} = (\bar{\rho} + p)u^\mu u^\nu - g^{\mu\nu}p. \tag{1.8}$$

where $\bar{\rho}(t)$ denotes the mass density, p is the pressure and u^μ indicates the four-velocity. In taking it into the Einstein field equations it is found through a tedious calculation that the FRW metric is indeed a solution, provided that the scale factor $a(t)$ satisfies the *Friedmann Cosmological Equation*

$$\left(\frac{\dot{a}}{a}\right)^2 = \frac{8\pi G}{3}\bar{\rho} - \frac{k}{a^2}, \tag{1.9}$$

and the local first law of thermodynamics

$$\dot{\bar{\rho}} = -3(\bar{\rho} + p)\frac{\dot{a}}{a}. \tag{1.10}$$

[1] Cornish, Spergel and Starkman (1998) show that for some compact topologies the space need not to be infinite

The solution to these equations clearly depends on the value of k and the equation of state, the way in which the density $\bar{\rho}$ depends on the scale factor $a(t)$. In many cases of physical interest the equation of state can be expressed expressed by $p = w\bar{\rho}$ (*cf.* Coles & Lucchin 1995) where the parameter w is a constant. For instance, if the density is dominated by non-relativistic matter, particles whose rest mass is much greater than their kinetic energy, $p \approx 0$, it is straightforward to show from eqn. (1.10) that the density drops with the inverse of the volume as the universe expands:

$$\bar{\rho} \propto a^{-3}. \tag{1.11}$$

Also interesting in cosmological terms are the cases in which the density is dominated by relativistic particles ($p = \frac{1}{3}\bar{\rho}$, $w = \frac{1}{3}$), for instance photons,

$$\bar{\rho} \propto a^{-4}, \tag{1.12}$$

or by a third type of "matter" known as *vacuum energy* ($p = -\bar{\rho}$, $w = -1$) the density stays constant as the universe expands. The existence of such "matter" can appear explicitly in the above equations if we apply the following transformations:

$$\bar{\rho} \rightarrow \bar{\rho} + \frac{\Lambda}{8\pi G} \qquad \text{and} \qquad p \rightarrow p - \frac{\Lambda}{8\pi G}, \tag{1.13}$$

(recall, we are assuming $c \equiv 1$) where Λ is the so called *cosmological constant.* With the introduction of the dimensionless parameters

$$\Omega \equiv \frac{\bar{\rho}}{\bar{\rho}_{crit}}, \qquad \lambda = \frac{\Lambda}{3H^2}. \tag{1.14}$$

where

$$\bar{\rho}_{crit} \equiv \frac{3H^2}{8\pi G}, \tag{1.15}$$

the Friedmann equation may then be recast as

$$H^2(t) \equiv \left(\frac{\dot{a}}{a}\right)^2 = H_0^2 \left[\Omega_0 \left(\frac{a}{a_0}\right)^{-3(1+w)} + \lambda_0 - (\Omega_0 + \lambda_0 - 1)\left(\frac{a}{a_0}\right)^{-2}\right]. \tag{1.16}$$

1.3 Perturbing the Universe

There are two crucial observations that any model of structure formation has to explain: the quadrupole anisotropy of CMB, as measured by COBE, is one part in 10^5 (Kogut *et al.* 1996) suggesting that the amplitude of the fluctuations was very small at the epoch of hydrogen recombination, $z_{rec} \approx 1400$; while redshift and velocity surveys of the Local universe show highly inhomogeneous matter distributions over galactic and cluster scales. The *gravitational instability* (GI) is believed to be the physical mechanism which amplifies the small primeval fluctuations into the structure that we observe today.

In eqn. (1.2) the effect of the curvature is small for distances much less than Hubble radius $H_0^{-1} = 3000\,h^{-1}$Mpc (a variety of observations clearly favour $0 < \Omega_0 < 2$

and $\lambda_0 \approx 0.7$ therefore $|k| < H_0^2$). Hence, the FRW metric is well approximated by $ds^2 = dt^2 - a^2(t)(dx^2 + dy^2 + dz^2)$ (the so-called Minkowski metric, recall, $c \equiv 1$), where (x, y, z) denote the comoving Cartesian coordinates. Assuming a conformal Newtonian gauge (*cf.* Padmanabhan 1993) the Einstein field equations applied to the first-order perturbations ϕ of such a metric yield the Poisson equation of Newtonian gravity:

$$\nabla^2\phi = 4\pi a^2 G\delta\bar{\rho}, \tag{1.17}$$

where $\delta\bar{\rho} \equiv \rho(\mathbf{x}, t) - \bar{\rho}(t)$ indicates the fluctuation of the mass density and ϕ is interpreted as the Newtonian potential. Note that eqn. (1.17) does not assume that $\delta\rho$ is small.

In the following two subsections we discuss two alternative formulations of the equations of motion of the non-relativistic matter, Eulerian and Lagrangian, §1.3.1 and §1.3.2, respectively. For each we obtain the solutions to the linearized equations of the GI. Some of the non-linear dynamics approximations are introduced in §1.3.3

1.3.1 The Eulerian Formalism

$$a\dot{\delta} + \nabla \cdot [(1 + \delta)\mathbf{v}] = 0 \tag{1.18}$$

$$a\dot{\mathbf{v}} + (\mathbf{v} \cdot \nabla)\,\mathbf{v} + \dot{a}\mathbf{v} = -\nabla\phi - \bar{\rho}^{-1}\nabla p, \tag{1.19}$$

$$\nabla^2\phi = 4\pi a^2 G\delta\bar{\rho}, \tag{1.20}$$

Equations (1.18)-(1.20) are the equations of motion of a non-relativistic perfect fluid in comoving coordinates. Eqn. (1.18) is the continuity equation (expressing mass continuity) and eqn. (1.19) is the Euler equation (conservation of the linear momentum). In this system of differential equations the overdensity field, $\delta(\mathbf{x}, t)$, appears rather than the usual density field,

$$\rho(\mathbf{x}, t) \equiv \bar{\rho}(t)[1 + \delta(\mathbf{x}, t)],$$

and the peculiar velocity, $\mathbf{v}(\mathbf{x}, t)$, is defined as

$$\mathbf{v} \equiv \frac{d\mathbf{r}}{dt} - \frac{\dot{a}}{a}\mathbf{r}, \tag{1.21}$$

over-dots indicate partial time derivatives. The pressure p is related to the density ρ through the equation of state, $p = w\rho$. For *adiabatic perturbations* there are no spatial variations in the equation of state, therefore $\nabla p = w\nabla\rho = w\bar{\rho}\nabla\delta$.

The Linear regime of Adiabatic perturbations

Linearizing our system of equation, we obtain

$$a\dot{\delta} + \nabla \cdot \mathbf{v} \approx 0, \tag{1.22}$$

$$a\dot{\mathbf{v}} + \dot{a}\mathbf{v} \approx -\nabla\phi - c_s^2\nabla\delta, \tag{1.23}$$

$$\nabla^2\phi = 4\pi G a^2 \delta\bar{\rho}. \tag{1.24}$$

Where c_s represents the adiabatic sound speed, $c_s^2 \equiv (\partial p/\partial\rho)_s = w$, and the subscript S indicates constant entropy throughout the space ($\nabla S = 0$).

A general vector field may be decomposed into a (potential) longitudinal and a (rotational) transversal part:

$$\mathbf{v}(\mathbf{x},t) = \mathbf{v}_{||} + \mathbf{v}_{\perp}, \qquad \nabla \times \mathbf{v}_{||} = \nabla \cdot \mathbf{v}_{\perp} = 0, \tag{1.25}$$

From the curl of eqn. (1.23) it follows that

$$\frac{\partial}{\partial t}(a\nabla \times \mathbf{v}) = \frac{\partial}{\partial t}(a\nabla \times \mathbf{v}_{\perp}) = 0. \tag{1.26}$$

This implies that rotational modes are not coupled to density perturbations and decay as a^{-1}. Combining the time derivative of the linearized continuity with the divergence of the linearized Euler (*cf.* eqn. 1.23) we yield the equation of motion for the longitudinal density perturbations

$$\ddot{\delta} + 2\frac{\dot{a}}{a}\dot{\delta} = \left(\frac{c_s}{a}\right)^2 \nabla^2\delta + 4\pi G\delta\rho \tag{1.27}$$

Since the coefficients are spatially homogeneous (independent of $\mathbf{x}$) this equation may be solved by expanding $\delta(\mathbf{x},t)$ in plane waves, $\delta(\mathbf{x},t) = \delta_{\mathbf{k}}(t)e^{i\mathbf{k}\cdot\mathbf{x}}$, $\lambda = 2\pi a(t)/k$, where λ is the proper wavelength. After some straightforward calculations, it is easy to show that the dynamical behaviour of $\delta_{\mathbf{k}}(t)$ obeys the following differential equation:

$$\ddot{\delta}_{\mathbf{k}} + 2\frac{\dot{a}}{a}\dot{\delta}_{\mathbf{k}} = -c_s^2\left(k^2 - k_J^2\right)\delta_{\mathbf{k}} \tag{1.28}$$

where we have defined the comoving Jeans wavenumber k_J by

$$k_J = a\left(\frac{4\pi G\bar{\rho}}{c_s^2}\right)^{1/2}. \tag{1.29}$$

Two qualitative behaviours of the solutions can be easily discerned from eqn. (1.28). For wavenumbers larger than k_J pressure dominates the right hand term and perturbations do not grow, merely oscillate. For $k < k_J$ self-gravity dominates so that gravitational instability can take place. Exact solutions to eqn. (1.28) exist for a variety of cases (see, for instance, Peebles 1980). Since the dynamical behaviour of $\delta_{\mathbf{k}}(t)$ is governed by a second order differential equation, in general, there is one monotonically growing solution and one monotonically decaying solution. In the limit $k \ll k_J$ the effects of the pressure p are negligible and thus all modes grow at the same rate. In this regime, the general solution to eqn. (1.27) is given

$$\delta(t,\mathbf{x}) = A(\mathbf{x})D_+(t) + B(\mathbf{x})D_-(t) \approx A(\mathbf{x})D_+(t) \tag{1.30}$$

where $D_+(t)$ and $D_-(t)$ are the growing and decaying modes, respectively, while $A(\mathbf{x})$ and $B(\mathbf{x})$ are time independent functions (Heath 1977). The decaying solution is a perturbation with initial overdensity and peculiar velocity arranged so its initial velocity quickly

becomes negligible (Peebles 1980). Thus for most of the history of the universe the growing solution quickly comes to dominate. In an Einstein-de Sitter universe $D_+(t) \propto a$ and $D_-(t) \propto a^{-3/2}$. For a dust universe with $\Omega < 1$, the growing mode D_+ is

$$D_+(t) = \frac{3\sinh\eta(\sinh\eta - \eta)}{(\cosh\eta - \eta)^2} - 2. \tag{1.31}$$

μ indicates conformal time $\eta \equiv (-k)^{1/2}\int^t dt'/a(t')$.

Given a solution for the density perturbation field $\delta(\mathbf{x}, t)$, the velocity, gravitational potential and gravity field follow. For the longitudinal modes $\mathbf{v} = \mathbf{v}_{||} = -\nabla\phi_v/a$. The gravity field is $\mathbf{g} \equiv -\nabla\phi/a$. Thus, from the system of differential equations, eqns. (1.22)–(1.24), for $k \ll k_J$, we obtain

$$\phi_v = \frac{a^2 H f}{4\pi}\int \frac{\delta(\mathbf{x}')}{|\mathbf{x}' - \mathbf{x}|}d^3x', \qquad \phi = \frac{3}{2}\frac{\Omega H}{f}\phi_{\mathbf{v}}, \qquad \mathbf{g} = \frac{3}{2}\frac{\Omega H}{f}\mathbf{v}. \tag{1.32}$$

Where f is defined by

$$f(\Omega, z) \equiv \frac{d\log D_+}{d\log a} = \frac{\dot{D}_+(t)}{H(t)D_+(t)}. \tag{1.33}$$

The behaviour of $f(\Omega, z)$ at the present epoch (z=0) is very well described by $f \approx \Omega^{0.6}$ in the case of universes with negligible space curvature or rather small cosmological constant (Peebles 1980, Lahav *et al.* 1991, see also Lightman and Schechter 1990 for a slightly different approximation).

1.3.2 The Lagrangian Formulation

The Lagrangian formulation follows the trajectories of individual particles (or fluid elements). The particles are labelled by their initial (Lagrangian) comoving coordinates $\mathbf{q} \equiv \mathbf{x}(t = 0)$ and its trajectories are simply the familiar Newton's laws in an expanding universe:

$$\dot{\mathbf{v}}a + \mathbf{v}\dot{a} = -\nabla\phi, \tag{1.34}$$

$$a\dot{\mathbf{x}} = \mathbf{v}. \tag{1.35}$$

Where the time derivatives are taken at fixed $\mathbf{q}$. As for the Eulerian formalism to obtain the gravitational potential we solve the Poisson equation

$$\nabla^2\phi = 4\pi G a^2 \delta\bar{\rho}. \tag{1.36}$$

This equation requires evaluating the Eulerian density field $\delta\bar{\rho}(\mathbf{x}, t)$. It is straightforward to show that, for a collisionless fluid, the mass in a given Eulerian volume is obtained by

$$\rho(\mathbf{x}, t)d^3x = \bar{\rho}d^3q. \tag{1.37}$$

Where $\bar{\rho}$ is the mean density of the universe. In computing the Jacobian of this last transformation we obtain

$$\delta(\mathbf{x}, t) = \frac{\rho(\mathbf{x}, t)}{\bar{\rho}} - 1 = \left\|\frac{\partial\mathbf{x}}{\partial\mathbf{q}}\right\|^{-1} - 1, \tag{1.38}$$

where the double vertical bars denote the Jacobian of the determinant.

Our system of equations is thus given by the Lagrangian equations of motion for the particles (eqns. 1.34-1.35), mass conservation (eqn. 1.38) and the Poisson equation (eqn. 1.36).

Linear Solution

In the limit of small density perturbations, $\delta^2 \ll 1$ and small displacements between $\mathbf{x}$ and $\mathbf{q}$ the trajectories $\mathbf{x} = \mathbf{x}(\mathbf{q}, t)$ of particles are

$$\mathbf{x}(\mathbf{q}, t) = \mathbf{q} + \mathbf{x}^{(1)}(\mathbf{q}, t) + \mathbf{x}^{(2)}(\mathbf{q}, t) + \ldots . \tag{1.39}$$

Where successive terms are supposed to diminish rapidly. Hence, the the Eulerian over-density field (eqn. 1.38) to first order is then

$$\delta^{(1)} = -\nabla_{\mathbf{q}} \cdot \mathbf{x}^{(1)}(\mathbf{q}, t), \tag{1.40}$$

where the subscript $\mathbf{q}$ in ∇ indicates that the partial derivatives are taken with respect to $\mathbf{q}$. Decomposing $\mathbf{x}^{(1)}$ into its longitudinal and transverse parts

$$\mathbf{x}^{(1)}(\mathbf{q}, t) = \mathbf{x}^{(1)}_{||} + \mathbf{x}^{(1)}_{\perp}, \qquad \nabla \times \mathbf{x}^{(1)}_{||} = \nabla \cdot \mathbf{x}^{(1)}_{\perp} = 0. \tag{1.41}$$

we see that only the longitudinal component generates density fluctuations and gravitational perturbations:

$$\delta^{(1)}(\mathbf{x}) = \nabla_{\mathbf{q}} \cdot \mathbf{x}^{(1)}(\mathbf{q}, t) = \nabla_{\mathbf{q}} \cdot \mathbf{x}^{(1)}_{||}(\mathbf{q}, t) \tag{1.42}$$

$$\nabla\phi = -4\pi G\bar{\rho}a^2\nabla_{\mathbf{q}}^{-1}\left(\nabla_{\mathbf{q}} \cdot \mathbf{x}^{(1)}\right) = -4\pi\bar{\rho}a^2\mathbf{x}^{(1)}_{||}. \tag{1.43}$$

From the equations of motion, to first order,

$$\ddot{\mathbf{x}}^{(1)} + 2\frac{\dot{a}}{a}\dot{\mathbf{x}}^{(1)} = -4\pi G\bar{\rho}\mathbf{x}^{(1)}_{||}. \tag{1.44}$$

Hence it is simple to verify that the transverse part of $\mathbf{x}^{(1)}$ decays with a^{-1} as the universe expands, while the longitudinal part is formally analogous to eqn. (1.27) in a dust universe ($c_S^2 = w = 0$). Therefore, we know that the general solution is similar to eqn. (1.30), with growing and decaying functions $D_{\pm}(t)$ multiplying a function of $\mathbf{q}$. Retaining only the growing mode the solution is then given by

$$\mathbf{x}^{(1)}(\mathbf{q}, t) = \mathbf{q} + D_+(t)\Psi(\mathbf{q}), \tag{1.45}$$

where $\Psi(\mathbf{q})$ is a longitudinal vector field solution called the *growing-mode displacement* field. Finally, from our system of equations we obtain:

$$\delta^{(1)}(\mathbf{q}, t) = -D_+(t)\,\nabla \cdot \Psi(\mathbf{q}), \tag{1.46}$$

$$\mathbf{v}^{(1)}_{||}(\mathbf{q}, t) = \dot{D}_+(t)\,\Psi(\mathbf{q}). \tag{1.47}$$

1.3.3 Beyond the Linear Regime

Linear theory provides us with the dynamical behaviour of the density field and peculiar velocity field and it also relates both fields through a simple and invertible expression (*cf.* eqn. 1.22). However, we should have in mind that such a model is only applicable if $\delta^2 \ll 1$ and therefore can lead to non negligible errors if used to model high density regions. Unlike regions deeply in the non-linear regime (which tend to erase the memory of the initial conditions) mildly non-linear regions still carry crucial information about large scale structure of the universe.

The stepping-stone towards the non-linear regime is due to Zel'dovich (1970) who extrapolate the linear trajectories of eqn. (1.45) into the mildly non-linear regime (Zel'dovich Approximation, ZA).

Nusser *et al.* (1991) shows that the continuity equation (eqn. 1.38) can be expressed as

$$\delta(\mathbf{x}) = \left\| I - (fH)^{-1} \frac{\partial \mathbf{v}}{\partial \mathbf{x}} \right\| \tag{1.48}$$

where I is the unit matrix. From this relation we may compute the overdensity field given the peculiar velocity field. However, it is rather difficult to invert to obtain $\mathbf{v}$ when δ is given. With the purpose of of overcoming this difficulty Nusser *et al.* (1991) proposed the empirical formulae

$$\nabla \cdot \mathbf{v} = \frac{(Hf)\delta(\mathbf{x})}{[1 + 0.18\delta(\mathbf{x})]}. \tag{1.49}$$

A better approximation may be obtained by considering in eqn. (1.39) terms to second order. Gramann (1993a,b) obtains the following expression:

$$\delta(\mathbf{x}) = -(Hf)^{-1}\nabla \cdot \mathbf{v} + \frac{4}{7}(Hf)^{-2} \sum_{i=1}^{3} \sum_{j>i}^{3} \left(\frac{\partial v_i}{\partial x_i} \frac{\partial v_j}{\partial x_j} - \frac{\partial v_i}{\partial x_j} \frac{\partial v_j}{\partial x_i} \right), \tag{1.50}$$

which is also invertible allowing thus to compute $\nabla \cdot \mathbf{v}$ given δ.

Bernardeau (1992) after a mathematical tour de force shows that in assuming Gaussian fluctuations and in the limit of the infinitely small variance of the overdensity field (*cf.* § 1.4) the divergence of the velocity field is given by:

$$\nabla \cdot \mathbf{v} = \frac{3}{2}(Hf)\left\{1 - [1 + \delta(\mathbf{x})]^{\frac{2}{3}}\right\}. \tag{1.51}$$

Bernardeau *et al.* (1999) use third order perturbation theory to generalize this expression both for Gaussian smoothed and top-hat smoothed density fields (*cf.* § 1.4).

Other non-linear approximations will be presented in § 2.

1.4 Random Fields

An n-dimensional *random field* $G(\mathbf{x})$ is an infinite-dimensional random variable, one for each point $\mathbf{x}$ in the n-dimensional real space. This variable is defined by a set of finite-dimensional joint probability distributions of its values at any m points, $m = 1, 2, ...$ Hence, to define a random variable $G(\mathbf{x})$, one must specify the 1-dimensional probability distribution of $G(\mathbf{x}_1)$ for all $\mathbf{x}_1$, the 2-dimensional probability distribution of the vector $[G(\mathbf{x}_1), G(\mathbf{x}_2)]$ for all $\mathbf{x}_1$ and $\mathbf{x}_2$, so forth. A random field is strictly homogeneous (isotropic) if all finite dimensional distributions are translationally (rotationally) invariant. Thus the 1-dimensional probability distribution is independent of $\mathbf{x}_1$ and the 2-dimensional probability distribution will depend only upon the scalar quantity $r = |\mathbf{x}_1 - \mathbf{x}_2|$. In cosmology, the usual random fields are the fluctuations of the density field, δ, the velocity field $\mathbf{v}$ or the gravitational potential ϕ. The n-dimensional space is the physical space at some fixed time instant t.

Ergodicity

The observed universe is unique. This implies that averages have to be spatial ones. Such averages will be equal to an ensemble of universes if the *Cosmic Ergodic Theorem* holds. *Ergodicity* in the cosmological context means that ensemble averaging and spatial averaging are equivalent. Note that, in contrast with the common practice in statistical mechanics, the cosmological Ergodic Hypothesis refers to the spatial distribution of a random field at a fixed time rather than to the time evolution of the system. Thus, for instance, the ensemble average of the random field $\delta(\mathbf{x})$ at a point $\mathbf{x}$, $\langle\delta(\mathbf{x})\rangle$, is simply the expectation value of the random variable $\delta(\mathbf{x})$.

Gaussianity

Let us introduce some of the statistics used by cosmologist to characterize the spatial distribution of matter. We define *r.m.s.* σ_δ fluctuations of a continuous density field $\delta(\mathbf{x})$ as

$$\sigma_\delta^2 \equiv \left\langle \delta(\mathbf{x})^2 \right\rangle, \tag{1.52}$$

and the *correlation function* by

$$\xi(r_{12}) \equiv \left\langle \delta(\mathbf{x}_1)\delta(\mathbf{x}_2) \right\rangle. \tag{1.53}$$

(Note that for a homogeneous and isotropic random process ξ only can depend on the distance between the two points $r_{12} = |\mathbf{x}_1 - \mathbf{x}_2|$.) The correlation function is a measure of the spatial correlation of the field $\delta(\mathbf{x})$.

A random field is said to be *Gaussian* if all N-point multivariate probability distribution functions are multivariate Gaussian distributions defined by their mean vector

$\langle\delta(\mathbf{x}_i)\rangle$ (which the ergodicity implies to be identically zero) and their covariance matrix $M_{ij} = \xi(\mathbf{x}_i, \mathbf{x}_j)$. Gaussianity is a very popular assumption for two reasons. The first one is that the calculations are "easy" to perform. The second reason of their popularity is that some structure formation theories, as we will see, predict that the initial density field is a Gaussian random field. An interesting feature of this assumption is that all homogeneous and isotropic Gaussian random fields are ergodic if and only if the power spectrum is continuous (Adler 1981). We will introduce the power spectrum of a scalar field below.

Power spectrum

If we expand the $\delta(\mathbf{x})$ field in plane waves as

$$\delta(\mathbf{x}) = \frac{V_u}{(2\pi)^3} \int e^{i\mathbf{k}\cdot\mathbf{x}} \delta_{\mathbf{k}} d^3k, \tag{1.54}$$

we see that its Fourier transform $\delta_{\mathbf{k}}$ is given by

$$\delta_{\mathbf{k}} = \frac{1}{V_u} \int e^{-i\mathbf{k}\cdot\mathbf{x}} \delta(\mathbf{x}) d^3x, \tag{1.55}$$

where V_u may be thought of a "fair sample" of the universe. Warning: many authors employ different conventions to place the factors of V_u, 2π and the signs of the exponents. The *power spectrum* of the density field $\delta(\mathbf{x})$ is defined as the expectation of the two-point function in Fourier space, as follows:

$$\left\langle \delta_{\mathbf{k}_1} \delta_{\mathbf{k}_2} \right\rangle \equiv P(k_1) \delta_D(\mathbf{k}_1 - \mathbf{k}_2) \tag{1.56}$$

where δ_D is the well-known Dirac delta function. This implies that even if $\delta_{\mathbf{k}}$ is not a Gaussian distribution, the random variable $\delta(\mathbf{x})$, being an infinite sum of independent random variables, will still be Gaussian by the Central Limit Theorem for some well-behaved power spectra. We can see that the Dirac function in eqn. (1.56) is required because of the translational invariance, $\langle\delta(\mathbf{x}_1)\delta(\mathbf{x}_2)\rangle = \xi(|\mathbf{x}_1 - \mathbf{x}_2|)$. Similarly, we can also see that isotropy implies that $P(k)$ depends only the magnitude of the wave-vector $\mathbf{k}$.

For the growing mode of linear theory, the peculiar velocity is related to the density fluctuations field: $\delta(\mathbf{x}) \approx -\nabla \cdot \mathbf{v}/(aHf)$. It follows that the power spectrum of $\mathbf{v}$ is proportional to the power spectrum:

$$P_v(k) = \frac{a^2 f^2 H^2}{k^2} P(k). \tag{1.57}$$

Window Functions

For some calculations it may be necessary to apply a cutoff at high spatial frequencies. The smoothed field $\tilde{\delta}(\mathbf{x})$ that may be obtained by convolution of the "raw" field with some

weighting function W (called *window function*) having a characteristic scale r_W is given by

$$\tilde{\delta}(\mathbf{x}) \equiv \int \delta(\mathbf{x}')W(\mathbf{x}' - \mathbf{x}, r_W)d^3x', \tag{1.58}$$

has *r.m.s.* $\sigma_{\tilde{\delta}}$ fluctuations given by

$$\sigma_{\tilde{\delta}}^2 = \langle|\tilde{\delta}(\mathbf{x})|^2\rangle = \frac{1}{(2\pi)^3}\int |W(\mathbf{k})|^2 P(k)d^3k. \tag{1.59}$$

Where $W(\mathbf{k})$ is the representation in Fourier space of $W(\mathbf{y}, r_W)$. The window function has the following properties: $W(\mathbf{x}' - \mathbf{x}, r_W) = const. \simeq r_W^{-3}$ if $|\mathbf{x} - \mathbf{x}'| \ll r_W$, $W(\mathbf{x}' - \mathbf{x}, r_W) = 0$ if $|\mathbf{x} - \mathbf{x}'| \gg r_W$, satisfying the relation $\int W(\mathbf{x}' - \mathbf{x}, r_W)d\mathbf{y} = 1$. One of the most common window functions is the "*top hat*" (TH) window function which is defined by the relation

$$W_{TH}(|\mathbf{x} - \mathbf{x}'|; r_{TH}) = \frac{3}{4\pi r_{TH}^3} H(1 - \frac{|\mathbf{x} - \mathbf{x}'|}{r_{TH}}), \tag{1.60}$$

where H denotes the Heaviside step function ($H(y) = 0$ if $y \leq 0$, and $H(y) = 1$ if $y > 0$). Another commonly used window function is the *Gaussian* kernel:

$$W_G(|\mathbf{x} - \mathbf{x}'|; r_G) = \frac{1}{(2\pi r_G^2)^{2/3}} \exp\left(-\frac{|\mathbf{x} - \mathbf{x}'|^3}{2r_G^2}\right). \tag{1.61}$$

1.5 Origin and Nature of the fluctuations

Perhaps the most fundamental difference between models for structure formation lies with their *initial conditions.* Inflation is the only mechanism known of laying down large-scale density or curvature perturbations in the early universe. Models with initial curvature perturbations are usually called *adiabatic* models. The alternative causal models begin with no density or curvature fluctuations on large-scales and are thus called *isocurvature* models. The generation mechanism is also crucial for determining the spectrum and statistics of the fluctuations. The simplest inflationary models predict a primordial power spectrum $P_i(k)$ which is nearly scale invariant and for a Gaussian distribution of fluctuations (Bardeen, Steinhardt and Turner 1983), although higher order effects can break scale-invariance and generate non-gaussianity (Moscardini *et al.* 1991). Topological defect perturbations are intrinsically non-Gaussian but are typically also scale-invariant in the generalized sense of "scaling" (Kibble 1985).

Another important distinction between models is the *perturbation type.* In cosmological perturbation theory any linear fluctuation may be decomposed into scalar (longitudinal modes), vector (transversal modes) and tensor components. These manifest themselves as density, vorticity and gravitational waves respectively and they do not interact in linear theory (Peebles 1993). For the purpose of this thesis we will only consider scalar modes since only these are responsible for the growth of large-scale structure in response to their own self-gravity.

Finally, the nature of *dark matter* components that dominates today's universe determines the history of the equation of state and, therefore the evolution of the power spectrum. The current power spectrum $P(k)$ can be specified by a single function, the *transfer function* $T(k)$, defined so that

$$P(k) \equiv T^2(k)P_i(k), \tag{1.62}$$

where the primordial power spectrum is assumed to be a simple power law:

$$P_i(k) \propto k^n \tag{1.63}$$

for some constant n called *spectral index.*

In summary, the observable properties of structure formation models are encapsulated in the time evolution of metric fluctuations. This in turn is governed by the stress properties of the matter both through its initial conditions and intrinsic properties.

1.5.1 CDM

Currently, there are a plethora of rival theories of structure formation predicting all sorts of power spectra that try to fit the observational facts. The most popular model has been the cold dark matter (CDM) model (Peebles 1982). In this model the primordial fluctuations are usually assumed to be arise from quantum fluctuations during a hypothetical inflationary epoch when the universe was less than 10^{-32} seconds old. These initial fluctuations are adiabatic with an Harrison-Zel'dovich initial power spectrum ($P_i(k) \propto k$). In addition, it is postulated that more than 90 % of the matter is cold dark matter, slow-moving non-baryonic particles interacting only via gravity. In this scenario small perturbations collapse first and larger objects result from the association of many smaller clumps.

1.6 Biasing

We observe galaxies directly, but most of the matter in the universe is in the form of dark matter (either baryonic or non-baryonic). Hence, a connection must be made between the density fields of galaxies and that of the mass. The simplest assumption is that the distribution of galaxies traces that of the mass, with the amplitude of the fluctuations being identical:

$$\delta_g(\mathbf{x}) = \delta(\mathbf{x}) \tag{1.64}$$

However, there is evidence that luminous matter does not trace the mass evenly. In the outermost regions of galaxies the luminous matter decreases relative to the dark matter. On larger scales, estimates of the spatial correlation function for galaxies and clusters do not show the same amplitude. Galaxies and clusters cannot therefore both be good tracers of the mass (Bahcall & Soneira 1983). The first specific model for biasing was introduced

by Kaiser (1984). He addressed the biasing of galaxy clusters relative to mass showing that rich galaxy clusters form only at high-density peaks of the mass distribution. This peaks biasing model makes a definite prediction for the correlation function of clusters, ξ_{cc}, relative to the mass:

$$\xi_{cc}(r) = b^2 \xi(r) \tag{1.65}$$

Where the biasing parameter, b, is related to the density threshold above which galaxy clusters are formed, after smoothing the density fields on a certain scale since the object distributions are samples of discrete particles. Davis *et al.* (1985), Peacock & Heavens (1985) and Bardeen *et al.* (1986) extended this model to the galaxies relative to the dark matter. An even more specific model is that of *linear biasing*, in which

$$\delta_o(\mathbf{x}) = b\delta(\mathbf{x}) \tag{1.66}$$

The subscript o denotes objects (galaxies, clusters or halos). When $b > 1$ this model cannot be strictly correct since values of δ_o below -1 are forbidden. To avoid this problem the scheme

$$1 + \delta_o(\mathbf{r}) = [1 + \delta(\mathbf{r})]^b \tag{1.67}$$

has been sometimes employed in the literature. Coles (1993), Weinberg (1994) and Mo & White (1996) showed empirically that in a wide range of models which invoke *local bias*

$$\delta_o(\mathbf{r}) = g\,[\delta(\mathbf{r})]\,, \tag{1.68}$$

the ratio of the fluctuations $\sigma(R)$ in the objects and dark matter is independent of scale R on scales larger than $\sim 5\,h^{-1}$Mpc. Recently, Dekel & Lahav (1998a) have introduced the concept of *stochastic nonlinear galaxy biasing* which replaces the linear deterministic relationship for galaxies (eqn. 1.66) by a conditional distribution $P(\delta_g|\delta)$. The nonlinearity is characterized by the conditional mean

$$\langle \delta_g|\delta \rangle \equiv b(\delta)\delta, \tag{1.69}$$

where $b(\delta)$ is the *mean biasing function.* The local scatter is represented by the conditional variance $\sigma_b^2(\delta)$ and higher moments. The origin of this scatter may be attributed to hidden factors affecting galaxy formation and the discrete sampling of the density fields by the distribution of galaxies. The formalism still reproduces eqn. (1.66) in the limit of negligible $\sigma_b^2(\delta)$ and the second order moments of $b(\delta)$ and $b^2(\delta)$ being similar.

Chapter 2

The Reconstruction Methods

2.1 Introduction

The aim of this chapter is to present and discuss some of the methods that have been used in the reconstruction of the cosmic density and velocity fields. The term reconstruction is applied in a broad sense: it stands for a procedure which estimates the underlying density and velocity field starting from noisy and incomplete observational data.

In large scale structure studies we would like to be provided with all–sky catalogues of extragalatic objects selected according to the same criteria and observed using a unique experimental apparatus. In practice this is not possible and very often we have to face the problem of merging together several different catalogues to obtain a homogeneous all–sky catalogue. The data available can be divided into two general categories: *redshift surveys* and *peculiar velocity surveys.*

Historically, redshift surveys were carried out to provide us with cosmography of our Galactic neighbourhood. A wide variety of structures including voids, filaments and superclusters have been revealed by redshift surveys. They have also supplied the raw data for several statistical studies that have improved our quantitative understanding of the galaxy distribution. A series of major technological improvements have been providing the astronomical community with a growing wealth of data. For instance, the InfraRed Astronomical Satellite (*IRAS*) surveyed the sky in four broad photometric bands centred roughly at 12, 25, 60, and 100 μm. Because the Galaxy is largely transparent to infrared radiation, the *IRAS* satellite was able to gather information all across the entire sky.

The first large redshift survey of *IRAS* galaxies was compiled by Strauss and collaborators and included all 2658 galaxies down to $f_{60\mu m} = 1.936$ Jy. Fisher *et al.* (1995a) extended this dataset deeper over the same region of sky down to $f_{60\mu m} = 1.2$ Jy, for a total of 5339 galaxies. A parallel effort involving British institutions (Durham, Oxford, Edinburgh, Imperial College and Cambridge) have recently finished a catalogue (Saun-

ders 1998) containing $\sim$ 15 500 *IRAS* galaxies with a $f_{60\mu m} \geq 0.6$ Jy, on average depth of $\sim 100\,h^{-1}$Mpc covering 80% of the sky. This survey was preceded by QDOT (Queen Mary and Westfield College, Durham, Oxford and Toronto), which is a sparser sample of one in six of the same database to an identical flux limit. This last survey covers the sky with 2184 galaxies; the median redshift is $84\,h^{-1}$Mpc.

To compute the radial peculiar velocity of an extragalactic object we need both its redshift distance and its true distance, d. This has become possible with the development of methods for inferring distances independent of the redshift based on intrinsic relations between galaxy quantities. Tully & Fisher (1977) found that the absolute blue magnitudes of spiral galaxies were strongly correlated with the rotational velocity inferred from their deprojected 21 cm linewidths. Faber & Jackson (1976) established a similar relationship for elliptical galaxies; the absolute magnitude correlates with the internal velocity dispersion, such that $L \propto \sigma^4$. Djorgovski & Davis (1987) and Dressler *et al.* (1987) noted that the scatter in the Faber-Jackson relationship could be reduced by combining isophotal diameters with the internal velocity dispersion of a galaxy, the so called D_n–σ relation. There is now a rapidly growing database of galaxies with measured peculiar velocities, *Mark*III (Willick *et al.* 1995; 1996; 1997a) and SFI (Giovanelli *et al.* 1998). Excellent reviews of peculiar velocities measurements are given by Dekel (1994) and Strauss & Willick (1995a).

The layout of the present chapter is as follows: in section § 2.2 we present some of the techniques applied for recovering $\delta(\mathbf{x})$ from all–sky redshift surveys. In the following section, § 2.3, we briefly discuss methods to reconstruct the true density field from the observed peculiar velocity field. Finally, in the last section, § 2.4, we refer to some of the techniques used to trace the present-time density field back in time to the linear regime.

2.2 Reconstructing $\delta(\mathbf{x})$ from the redshift space distribution

In practice, we have a collection of point–like particles which are transformed into a continuous smoothed overdensity field by applying

$$\hat{\delta}(\mathbf{s}) = \frac{1}{\bar{n}} \sum_{i}^{N} W\left(|\mathbf{s} - \mathbf{s}_i|; r_{sm}\right) \frac{1}{\phi(\mathbf{s}_i)} - 1. \tag{2.1}$$

Where $W(|\mathbf{x}|; r_{sm})$ is the *window function* characterized by a smoothing length r_{sm} normalized to be unit integral, $\mathbf{s}_i$ denotes the redshift of the particle i, N is the number of objects within the volume V of the catalogue, $\bar{n}$ the average galaxy number density, given by

$$\bar{n} \equiv \frac{1}{V} \sum \frac{1}{\phi(\mathbf{s}_i)}. \tag{2.2}$$

Where $\phi(s)$ is the *selection function*, defined as the fraction of galaxies at distance s which meet the selection criteria. The density estimator $\hat{\delta}(\mathbf{s})$ is going to be different from the

underlying density field, $\delta(\mathbf{x})$, since the former is subject to a number of different sources of uncertainty:

- *Sky Coverage.* Even the so called all–sky catalogues have incomplete sky coverage. The unsurveyed regions are either due to Galactic extinction (or cirrus emission) near the Galactic plane or due to instrumental limitations or failure to look at parts of the sky (for instance, the *IRAS* satellite ran out of cryogen before completing its survey of the sky).

- *Shot-noise.* Galaxies sample the underlying density field sparsely. Therefore a smoothing volume only contains a finite number of objects. The uncertainties raised by this fact in the density fields are termed *shot-noise.* The contribution to the total error on the fluctuations of the density field, is simply

$$\left\langle \delta^2(\mathbf{x}) \right\rangle_{sn}^2 = \frac{1}{\bar{n}} \left\{ \sum_{i=1}^{N} \left[W\left(|\mathbf{x} - \mathbf{x}_i|; r_{sm}\right) \frac{1}{\phi(x_i)} \right]^2 \right\}, \tag{2.3}$$

  (because we assume that the sampling of the underlying density field by galaxies is a Poisson point process). This source of error is particularly important in a flux limited catalogue because it increases with the sparseness of the sampling, $\sim 1/\phi(r)$.

- *Redshift Distortions.* The s–space coordinate, $\mathbf{s}_i$, of an object is not in general equal to its r–space coordinate. The peculiar velocity field, $\mathbf{v}(\mathbf{x})$, maps onto the real r–space coordinate x_i as follows:

$$s_i = H_0 x_i + \hat{\mathbf{x}}_i . \Big[\mathbf{v}(\mathbf{x}_i) - \mathbf{v}_{LG} \Big], \tag{2.4}$$

  where $\mathbf{v}_{LG}$ denotes the Local Group peculiar velocity, $\hat{\mathbf{x}}_i$ the unit vector along the object's vector position $\mathbf{x}$ while $s_i \equiv |\mathbf{s}_i|$. Hence, peculiar velocities driven by large-scale structure will change the pattern of clustering. For instance a galaxy on the far side of a cluster will have a negative peculiar velocity, and appear closer to us in redshift space than in real space. A galaxy between us and the cluster in question will have a positive peculiar velocity and appear further away than its actual distance. On small scales, velocity dispersions create triple-valued regions (TVR) in which the same redshift arises at three distinct distances along the line of sight.

2.2.1 Filling-in the unsurveyed regions.

Ignoring unsurveyed regions altogether will cause systematic errors in any dynamical modeling. A number of filling techniques have been devised with the purpose of solving this problem. We may fill unsurveyed regions with a random distribution of objects whose mean number density has been estimated from the rest of the survey. Yahil *et al.* (1991, YSDH) developed a cloning procedure, in which galaxies are replicated from neighbouring low–latitude regions into the unsurveyed zones. Some more sophisticated schemes using

spherical harmonics, masked regions filled in uniformly according to the mean and Wiener filter have also been employed by Lahav *et al.* (1994) and Saunders *et al.* (1999). Using $l \leq 15$ spherical harmonics (*cf.* Jackson 1962)) this procedure was tested with *IRAS* 1.2 Jy mock catalogues reconstructing masked regions $|b| < 15°$ successfully (Lahav *et al.* 1994).

The best, although extremely difficult alternative to the above techniques is to survey the ZoA and other missing regions themselves. In recent years various studies have been attempt to unveil the galaxy distribution behind the Galaxy (see Balkowski & Kraan-Korteweg 1994 for an early review of the subject, and also Kraan-Korteweg *et al.* 1998 for an updated listing of the surveys underway and their respective limitations and selection effects).

2.2.2 Shot-Noise

The shot noise problem can be minimized by properly filtering the data. In a flux limited sample, the mean interparticle separation increases with the distance from the origin, $\propto [\bar{n}\phi(r)]^{-1/3}$ (since $\phi(r)$ decreases monotonically with r), and therefore the shot noise in the measured density field also increases. Several approaches to deal with this problem have been proposed. YSDH employ a top-hat variable smoothing length proportional to the interparticle separation thus keeping the level of shot-noise nearly constant throughout the volume of the survey. Nusser & Davis (1994) expand the density field in spherical harmonics and, in addition, apply a variable Gaussian with a smoothing length which is half of the interparticle separation. Fisher *et al.* (1995a) perform a similar expansion, but apply a Wiener Filter (WF) to smooth the density field.

We can model the observed density field, $\hat{\delta}(\mathbf{x})$, as being related to the true density field, $\delta(\mathbf{x})$, by

$$\hat{\delta}(\mathbf{x}) = \delta(\mathbf{x}) + \mu(\mathbf{x}), \tag{2.5}$$

where μ is the shot noise, which is assumed to be uncorrelated with the true signal and independent of the position. The WF can be formalized as the function $\mathcal{F}_{WF}$ that minimizes $Var \equiv \langle |\delta(\mathbf{r}) - \mathcal{F}_{WF}(\mathbf{r})\hat{\delta}(\mathbf{r})|^2 \rangle$ (Rybicki & Press 1992), where $\langle ... \rangle$ means ensemble average. In practice, we can use the cosmological ergodicity to express Var as an integral over the observable Universe, i.e.

$$Var = \int \left[\delta(\mathbf{r}) - \mathcal{F}_{WF}(\mathbf{r})\hat{\delta}(\mathbf{r})\right]^2 d^3r = \int \left[\delta(\mathbf{k}) - \mathcal{F}_{WF}(\mathbf{k})\hat{\delta}(\mathbf{k})\right]^2 d^3k. \tag{2.6}$$

Where the second identity in eqn. (2.6) follows from Parseval's theorem. The functional derivative of the right hand side in eqn. (2.6) yields (see Zaroubi *et al.* 1995, Lahav *et al.* 1994 for details)

$$\mathcal{F}_{WF}(\mathbf{k}) = \frac{\left\langle \delta^2(\mathbf{k}) \right\rangle}{\left\langle \hat{\delta}^2(\mathbf{k}) \right\rangle} = \frac{\left\langle \delta^2(\mathbf{k}) \right\rangle}{\left\langle \delta^2(\mathbf{k}) \right\rangle + \left\langle \mu^2 \right\rangle}, \tag{2.7}$$

where $\langle \delta^2(\mathbf{k}) \rangle$ is proportional $P(k)$. Thus the WF requires a prior model for $P(k)$. In the limit of large shot noise, $\langle \mu^2 \rangle \gg 1$, (little information on the underlying overdensity field)

the WF has the inconvenient tendency of vanishing and yielding a null field as the best estimate for the density field. In formal terms it is possible to overcome this disadvantage by applying a modified WF (see Andrews & Hunt 1977). A recent application of a modified WF has been performed by Yahil (private communication, see also Sigad *et al.* 1998). This filter is defined as the square root of the WF and it preserves the second moment of the overdensity field.

For a flux-limited catalogue the level of shot-noise varies with the distance to the origin. The eqn. (2.7) only holds if the level of shot-noise is independent of the position. A way of overcoming this difficulty is to interpolate between maps filtered with eq (2.7) at different levels of noise.

2.2.3 Redshift Distortions

Eqn. (2.4) shows that the information contained within a redshift survey alone is not enough to compute the peculiar velocity field. We need to have the additional information provided by the actual galaxy distance. Linear Gravitational Instability theory plus a prescription for biasing enable us to construct a model to correct for the redshift distortions on large scales (typically larger than about 5 h^{-1}Mpc).

Since the distribution of galaxies is specified in redshift space, the radial peculiar velocity, $u(\mathbf{x}) \equiv \hat{\mathbf{x}} \cdot [\mathbf{v}(\mathbf{x}) - \mathbf{v}_{LG}]$, where $\mathbf{v}_{LG}$ is the velocity of the Local Group, can be computed from

$$\mathbf{v}(\mathbf{x}) = \frac{H_0 \beta}{4\pi} \int \delta(\mathbf{x}') \frac{(\mathbf{x}' - \mathbf{x})}{|\mathbf{x}' - \mathbf{x}|} d^3\mathbf{x}', \tag{2.8}$$

assuming that $\delta(\mathbf{x}) = \hat{\delta}(\mathbf{s})$. The estimate of $\mathbf{v}(\mathbf{x})$ at the positions of the particles is then inserted in eqn. (2.4) to improve the estimate of the s–positions for the galaxies within the catalogue. This procedure is repeated until the distance estimates converge. Several authors (YSDH, Hudson 1993a, 1993b, Freudling, da Costa & Pellegrini *et al.* 1994, Branchini & Plionis 1996, Sigad *et al.* 1998) have implemented techniques with the same physical basis but different numerical approaches with the aim of reducing both possible bias and sources of error. In a seminal paper Kaiser (1987) shows that the estimate of the density in r–space, $\rho_r(\mathbf{x}) = n_r(\mathbf{x})/\phi(x)$, and the corresponding quantity in s–space, $\rho_s(\mathbf{s}) = n_r(\mathbf{s})/\phi(s)$, are related via the Jacobian of eqn. (2.4) and $n_s(\mathbf{x})d^3r = n_r(\mathbf{s})d^3s$. So, to first order in perturbation theory we have

$$\hat{\delta}(\mathbf{s}) = \delta(\mathbf{x}) - \frac{\partial u}{\partial r} - \left[2 + \frac{d\ln\phi(r)}{d\ln r}\right]\frac{u}{r}, \tag{2.9}$$

(for a detailed discussion of this approximation see also Cole, Fisher & Weinberg 1994 and Tegmark & Bromley 1995). The peculiar velocities are then computed assuming that the redshift density field approximates the real-density field, calculating the peculiar velocity field from eqn. (2.8), then correcting for the density in eqn. (2.9) accordingly. The procedure is repeated until $\delta(\mathbf{x})$ and the velocity field converge to a solution that is consistent with the observed redshifts.

So far we have been discussing iterative methods to correct the redshift distortions on scales larger than 5 h^{-1}Mpc. A different strategy has been developed by Nusser & Davis (1994) and Fisher *et al.* (1995b) in which the velocity and density fields are computed applying non-iterative techniques. Nusser and Davis (1994) have used the Zel'dovich approximation for relating the initial position of an object, at $t = 0$, with its s–space position. Conservation of the number of galaxies and the additional assumption that the velocity field in redshift space remains irrotational allows one to derive a differential equation for the velocity potential, $\Phi_{\mathbf{v}}$, in s–space. The source term for such an equation is given by the fluctuations in the overdensity field, $\delta(\mathbf{s})$, corrected for the *rocket effect* (Kaiser 1987; Kaiser and Lahav 1989). Decomposing the velocity potential and the overdensity on a sphere in spherical harmonics, Y_{lm}, yields:

$$\frac{1}{s^2}\frac{d}{ds}\left(s^2\frac{d\Phi_{\mathbf{v},lm}}{ds}\right) - \frac{1}{1+\beta}\frac{l(l+1)\Phi_{\mathbf{v},lm}}{s^2} = \frac{\beta}{\beta+1}\left(\hat{\delta}_{lm} - \frac{1}{s}\frac{d\ln\phi}{d\ln s}\frac{d\Phi_{\mathbf{v},lm}}{ds}\right). \qquad (2.10)$$

$\Phi_{\mathbf{v},lm}$ and $\hat{\delta}_{lm}$ are the (lm)–spherical harmonic coefficients (*cf.* Jackson 1962) for the velocity potential and the overdensity field, respectively. The velocity field is then derived by differentiation from $\mathbf{v}(\mathbf{s}) = -\nabla\Phi_{\mathbf{v}}(\mathbf{s})$. For more details see chapter § 3. Fisher *et al.* (1995b) have based their method on an expansion of the overdensity field in orthogonal radial and angular functions. For all–sky surveys the peculiar velocities only couple radial modes leaving the angular modes of the overdensity field modes unaffected. Furthermore, the matrix distortion, $(\mathbf{Z}_l)_{mn}$, which connects the (n,l,m)–modes of the real and redshift space overdensity fields is invertible and its inverse allows us to compute the real density field. Thus, they have performed an inversion regularized by the Wiener filter

$$\delta_{lmn} = \sum_{n',n''}(\mathcal{F}_{WF})_{ln'n''}(\mathbf{Z}_l^{-1})_{n''n}\hat{\delta}_{lmn}, \qquad (2.11)$$

where $(\mathcal{F}_{WF})_{ln'n''}$, δ_{lmn} and $\hat{\delta}_{lmn'''}$ denote the Wiener Filter, r–space and s–space overdensity field spherical harmonics coefficients, respectively.

Other iterative approaches to real space reconstruction were introduced by Taylor & Rowan–Robinson (1993) and Gramann (1993b). They use the Zel'dovich approximation to extend the Kaiser *et al.* (1991) and YSDH procedures, respectively, into the mildly non linear regime.

The smoothing applied in the calculation of the measured overdensity field, $\hat{\delta}$, generally accounts for any deviations from linear dynamics. Unfortunately, it is not adequate around overdensities, which may be high enough to be surrounded by triple-valued regions. The crudest solution is to replace the objects belonging to a cluster with a single particle at the cluster centre. YSDH described a distance–averaging procedure to deal with TVR (see also Freudling, daCosta & Pelligrini 1994 for a slightly different approach). Willick *et al.* (1997b) introduced a probabilistic technique in which given estimates of the overdensity and peculiar velocity fields we may calculate the probability function of a given object being between x and $x+dx$. This shares the probability among the three possible solutions within the TVRs.

2.3 Reconstructing $\delta(\mathbf{x})$ from measured radial velocities

This section provides a brief discussion of the methods applied in the reconstruction of the overdensity field given measured peculiar velocities u_i sparsely sampled at positions $\mathbf{x}_i$ over a large volume, with random errors σ_i.

Since the rotational part of the velocity field decays with the expansion of the universe the velocity fields can be described by a velocity potential $\varphi_{\mathbf{v}}$. Bertschinger and Dekel (1989) have developed a technique that exploits this property of the cosmic velocity field predicted by linear theory which they called POTENT. The velocity potential is evaluated from a smoothed map of the radial peculiar velocity, $u(\mathbf{x})$:

$$\varphi_{\mathbf{v}}(\mathbf{x}) = -\int_0^r u(r', \theta, \phi) dr', \tag{2.12}$$

where r', θ, ϕ are the spherical coordinates of $\mathbf{x}$. The missing components of the velocity field are then recovered by differentiating this potential along the transverse directions. The mass density fluctuations are computed from the velocity field using the Zel'dovich-continuity approximation proposed by Nusser *et al.*(1991)

$$\delta(\mathbf{x}) = \left\| I - (fH)^{-1} \frac{\partial \mathbf{v}}{\partial \mathbf{x}} \right\| - 1, \tag{2.13}$$

where double vertical bars denote the determinant and I is the unit matrix. In practice we do not measure $u(\mathbf{x})$. Instead we have to perform the non-trivial step of smoothing the discrete data into a continuous radial peculiar velocity field defined onto some regular grid. The idea is that of reproducing the radial velocity field that would have been obtained had the true $\mathbf{v}(\mathbf{x})$ been sampled densely and uniformly, and smoothed with a Gaussian window of radius r_{sm}.

The radial velocity field at $\mathbf{x}_c$ is taken to be the value of an appropriate *local* velocity field model $\mathbf{v}(\alpha_k, \mathbf{x} - \mathbf{x}_c)$ at $\mathbf{x} = \mathbf{x}_c$. The model parameters α_k are obtained by minimizing the weighted sum of residuals

$$\sum_i W_i \left[u_i - \hat{\mathbf{x}}_i \cdot \mathbf{v}(\alpha_k, \mathbf{x}_i - \mathbf{x}_c) \right]^2, \tag{2.14}$$

within an appropriate local window function $W_i \equiv W(|\mathbf{x}_i - \mathbf{x}_c|; r_{sm})$, where the sum is over the galaxies in the catalogue. The window function is a Gaussian ($W_i \propto \exp[-(\mathbf{x}_i - \mathbf{x}_c)^2/2r_{sm}^2]$), modified such to reduce the following source of errors:

- *Tensor window bias.* Because the radial peculiar velocity vectors are not parallel, the u_i's cannot be averaged as scalars. Thus POTENT uses a tensor window coupled with the model for $\mathbf{v}(\alpha_k, \mathbf{x} - \mathbf{x}_c)$. The conical symmetry of the tensorial window may cause spurious flows if an improper velocity model is assumed.

- *Malmquist bias.* POTENT is subject to Malmquist bias, both homogeneous and inhomogeneous (for a comprehensive review see Strauss & Willick 1995a, Dekel 1994),

since it utilizes peculiar velocities obtained from "forward" distance estimates. This problem can be solved by using a Malmquist–free inverse–analysis (Schechter 1980) in which we minimize an expression the analogous of eqn. (2.14) both for the parameters of the distance indicator relation and for the parametric velocity field.

- *Random errors.* The galaxy distances are assumed to have standard error σ_i proportional to the distance $x_i = |\mathbf{x}_i|$: $\sigma_i = x_i\Delta$, where Δ indicates the *relative distance error* ($\Delta \approx 0.15$ and $\Delta \approx 0.21$ for the TF and D_n–σ, respectively)
- *Sampling Gradient.* The sampling gradient bias which is due to the inhomogeneous sampling of the velocity field within the smoothing window function.

Initial apparent inconsistencies between the mass density field obtained with the POTENT analysis (Dekel, Bertschinger & Faber 1990) and the *IRAS* 1.2-Jy survey have disappeared in subsequent more careful analyses (Dekel *et al.* 1993, Sigad *et al.* 1998, Dekel *et al.* 1998). An excellent agreement between the POTENT density field obtained from *Mark*III and the optical galaxies density field, reconstructed using iterative techniques, was also obtained by Hudson *et al.* (1995).

The similarity between the matter density field derived by POTENT and the density fields sampled by optical and *IRAS* galaxies is the best evidence that the linear bias prescription cannot be strongly violated on scales larger than $\sim 12\,h^{-1}$Mpc (the POTENT smoothing scale)

An alternative approach was introduced by Kaiser & Stebbins (1991) and Stebbins (1994). The observed radial velocities u_i^o are related to the true underlying velocity field $\mathbf{v}$ sampled at positions $\mathbf{x}_i$ via

$$u_i^o = \mathbf{v}(\mathbf{x}_i)\cdot\hat{\mathbf{x}}_i + \sigma_i \equiv u_i + \sigma_i. \tag{2.15}$$

Having a specific theoretical prior for the power spectrum $P(k)$ and assuming that the peculiar velocity field $\mathbf{v}(\mathbf{x})$ and the density field $\delta(\mathbf{x})$ are related via linear gravitational instability the minimum-variance estimation of the overdensity field is given by the following Wiener filter (WF):

$$\delta(\mathbf{x}) = \Big\langle \delta(\mathbf{x})u_i \Big\rangle \Big\langle u_i^o u_j^o \Big\rangle^{-1} u_j, \tag{2.16}$$

where $\langle ... \rangle$ indicates an ensemble average. The covariance matrix of the data $\langle u_i^o u_j^o \rangle$, which needs to be inverted in this last equation, can be cast as follows:

$$\Big\langle u_i^o u_j^o \Big\rangle = \Big\langle u_i u_j \Big\rangle + \Big\langle \sigma_i \sigma_j \Big\rangle = \hat{\mathbf{x}}_i \Big\langle \mathbf{v}(\mathbf{x}_i)\mathbf{v}(\mathbf{x}_j) \Big\rangle \hat{\mathbf{x}}_j + \sigma_i^2 \delta_{ij}, \tag{2.17}$$

To obtain the right term we applied eqn. (2.16).The last term is the diagonal matrix of error covariance while $\Big\langle u_i u_j \Big\rangle$ is computed from the assumed power spectrum (*cf.* Zaroubi, Hoffman and Dekel 1998 for details). As pointed out in § 2.2.2 WFs have the disadvantage that their statistical properties are not spatially uniform (a null field as the best estimate for the density field when the noise is dominant). Recently Zaroubi, Hoffman and Dekel (1998) have supplemented the WF with constrained realisations which compensate for this effect and produced random realisations which are statistically uniform in space.

2.4 Back-in-time

The problem of reconstructing the density field back in time is intimately related with that of removing the non–linear effects that spoil the simple proportionality between the initial (for instance at the recombination epoch) and the evolved density field. Several methods for modelling the non–linear gravitational clustering have been introduced in the recent past (see Sahni & Coles 1995 for a review of this subject). Tracing the evolution of the density field back in time, assuming that gravity is responsible for the growth of large scale structure, is a problem in which some of the boundary conditions are fixed at the present, the positions of the particles, and some others at early times, a vanishing velocity field. We cannot simply integrate backwards in time the gravitational instability system of differential equations by analytic approximations. This is completely hopeless in collapsed and virialized systems where the memory of the initial conditions has been lost. The major problem is the presence of the decaying mode that, having left no detectable effect at present, would amplify the noise in a backward integration. A possible solution to this problem is to study the evolution of velocity and gravitational potentials using first-order differential equations that only have growing mode solutions. If the velocity field has no vorticity it is straightforward to show, from the pressureless fluid equations, that the velocity potential, φ_v, obeys the Bernoulli equation

$$\frac{\partial \varphi_v}{\partial D_+} - \frac{1}{2}v^2 + \frac{3\Omega}{2f^2(\Omega)}\frac{(\varphi_v - \varphi_g)}{D_+} = 0. \tag{2.18}$$

where we have redefined the gravitational potential, $\varphi_g \rightarrow \varphi_g 4\pi G\bar{\rho}D_+/a$, and the peculiar velocity field, $\mathbf{v} \rightarrow \mathbf{v} \equiv d\mathbf{x}/dD_+ \equiv -\nabla\varphi_v$; recall that $D_+(t)$ is the growing mode, see § 1. Nusser & Dekel (1992) showed that under the assumption that Zel'dovich displacements obey momentum conservation the gravitational and velocity potential are analogous, $\varphi_v = \varphi_g$, and the Bernoulli equation takes the simple form

$$\frac{\partial \varphi_v}{\partial D_+} - \frac{1}{2}v^2 = 0. \tag{2.19}$$

which only allows for growing modes. This last equation can be integrated backwards to obtain ϕ_v. Considerations of continuity in the context of the Zel'dovich approximation led Gramann (1993a,b) to insert a correction term, C_g, in the right hand side of eqn. (2.19):

$$\frac{\partial \varphi_v}{\partial D_+} - \frac{1}{2}v^2 = C_g. \qquad \varphi_v = \varphi_g + D_+ C_g. \tag{2.20}$$

Where the function C_g is determined from the equation:

$$\nabla^2 C_g = \sum_{i=1}^{3}\sum_{j=i+1}^{3}\frac{\partial^2\varphi_g}{\partial x_i^2}\frac{\partial^2\varphi_g}{\partial x_j^2} - \left(\frac{\partial^2\varphi_g}{\partial x_i \partial xj}\right)^2, \tag{2.21}$$

In both approaches since the gravitational potential is recovered backwards in time one can infer the density field from the redefined Poisson equation, $\delta = D_+(t)\nabla^2\varphi_g$.

A natural way to deal with a mixed boundary value problem is provided by the least action formalism. Peebles (1989; 1990) applied such a scheme to the gravitational growth of density fluctuations in an expanding universe. Assuming that the mass is associated with the visible galaxies and that they preserve their individuality at early times then we may obtain the orbits of the galaxies back in time by minimizing the action S of the system in question

$$S \equiv \int_0^{t_0} \sum_i \left[\frac{1}{2} m_i a^2 \dot{\mathbf{x}}_i^2 - m_i \varphi_g(\mathbf{x}_i)\right] dt, \tag{2.22}$$

to determine the free parameters. In the previous equation the sum is over the particles in the system, while m_i is the mass of the particle i. The orbit of this particle $\mathbf{x}_i$ is modelled as $\mathbf{x}_i(t) = \mathbf{x}_i(t_0) + \sum_n f_n(t)\mathbf{C}_{i,n}$, where $f_n(t)$ satisfy the boundary conditions: $f_n(t_0) = 0$, and $\lim_{t\to 0} a^2 \dot{f}_n = 0$; and $\mathbf{C}_{i,n}$ are the parameters to be determined. Giavalisco *et al.* (1993) have shown that the Least Action Principle can be regarded as a high order Zel'dovich approximation if $f_n = (D_+(t) - D_+(0))^n$. Such an approach is exact in regions where orbit crossing has not happened. This method has primarily been applied to trace back the orbits of the LG members (Peebles 1989, 1990). A preliminary application of this method in a cosmological context was performed using a redshift sample by Shaya, Peebles & Tully (1994; 1995) and Peebles (1994).

Weinberg (1989; 1992) used a series of numerical tests to show that the rank order of the density field is not affected even when the structure becomes non-linear. The non-Gaussian present day distribution of galaxies in cells only needs to be *Gaussianized* in a rank preserving way: the densities are reassigned to fit the s form of the Gaussian cumulative distribution function. This primordial density field can then be evolved forward using a N-body code and compared with the observed density field. The details of this method depend on assumptions about galaxy biasing and the power spectrum. Weinberg (1989) applied this recipe on a volume-limited subsample of the Perseus-Pisces survey of Giovanelli-Haynes. The best solution found was for a standard CDM with $b = 2$. In a recent paper Narayanan & Weinberg (1998) have improved this technique by combining it with the aforementioned dynamical schemes by Nusser & Dekel (1992) and Gramann (1993a).

Chapter 3

The Reliability Tests

3.1 Introduction

The main goal of this chapter is to test the reliability of the reconstruction methods which we are going to apply in the reconstruction of the *IRAS PSCz* density and velocity fields. Ideally, we would like to compare our predictions with the "right answer". As a basic test we are going to compare our predictions for N-body models with the true velocities measured in such models. In this chapter we describe our N-body tests in detail. The reader should note that we are not trying to test the cosmologies from which the mock catalogues are drawn, but rather to quantify the random and systematic errors intrinsic to the reconstruction techniques. The current analysis uses the iterative method introduced by Yahil *et al.* (1991) and the non-iterative technique devised by Nusser & Davis (1994).

The main questions that we want to answer in this chapter are the following: a) Do we recover the correct density field? b) How well can our techniques estimate the peculiar velocity field of the observer? c) How well can we reconstruct the bulk flow of the 'Local Universe'? d) How well can our procedures predict the global velocity field?

In § 3.2 we describe our suite of mock catalogues. In section § 3.3 we give a lengthy description of the methods applied in the reconstruction of the overdensity and velocity fields. Our basic tests are introduced in § 3.4. We look for possible systematic effects on the reconstructions of the N-body models § 3.5. Our error analysis is perfomed in § 3.6. Finally, we conclude in § 3.8.

3.2 The Mock Catalogues

Recovering the cosmic density and velocity fields from redshift surveys is a complex procedure. Both observational biases that affect the original dataset and intrinsic theoretical limitations introduce random and systematic errors in the reconstructed density and ve-

Table 3.1: Cosmological Models.

Model	Ω_o	Λ	Γ	σ_8	V_{bulk} [km/s]	σ_{3D} [km/s]	$\sigma_{3D}^{1.5}$ [km/s]
LCDM	0.3	0.7	0.25	1.13	120	700	500
SCDMG	1.0	0.0	0.25	0.55	100	580	480
SCDMC	1.0	0.0	0.50	1.10	80	1400	900

locity fields. The key point in setting up a reconstruction procedure is therefore that of minimizing these errors. The calibration of reconstruction methods relies on artificial catalogues in which both the true mass and velocity fields are known and the observational errors are properly mimicked. The best approach to this problem will be, of course, to have a mock catalogue which mimics both the mass and galaxy distribution in the Local Universe. Kolatt *et al.* (1996) have followed this approach. They fed a "Zel'dovich time machine" (Nusser & Dekel 1992) with the smoothed and Wiener filtered density field from the *IRAS* 1.2-Jy redshift survey data (Fisher *et al.* 1995b). The output of such a procedure was subsequently *gaussianized* and its small scales filled as a Gaussian random realization of a prior power spectrum. Using the density and velocity fields they generated a particle distribution as initial conditions of an N-body code. Given the complexity of the whole procedure the Kolatt *et al.* (1996) method has only been applied within the context of one cosmological scenario. However, our ignorance of the underlying cosmological model makes it important to test the reliability of the reconstruction methods within different frameworks. Following a simpler route (e.g. Davis, Strauss & Yahil 1991) a number of different mock catalogues resembling the *PSCz* redshift survey have been extracted from N-body simulations of different cosmologies.

3.2.1 Making Mock Catalogues

Mock *PSCz* catalogues have been extracted from the N-body simulations performed by Cole *et al.* (1997). They used the AP^{3}M code of Couchman (1991) loaded with 192^3 particles in a box of comoving size of $345.6\,h^{-1}$Mpc. The particle mass is $1.62\times10^{12}\,\Omega_0 h^{-1} M_\odot$. Further details can be found in Cole *et al.* (1997). For the present analysis we have considered three different cosmologies (*cf.* Table 3.1): a flat model $\Omega = 0.3$ and cosmological constant term, $\Lambda c^2/3H_0^2 = 0.7$, a critical density universe ($\Omega = 1.0$) with power spectrum shape parameter, $\Gamma = 0.25$ and a standard CDM universe. In the two first cases, the fluctuation amplitude was normalized by the observed abundance of galaxy clusters This requires setting $\sigma_8 = 0.55\Omega_m^{-0.6}$ (Eke, Cole & Frenk 1996), where σ_8 is the linear rms mass

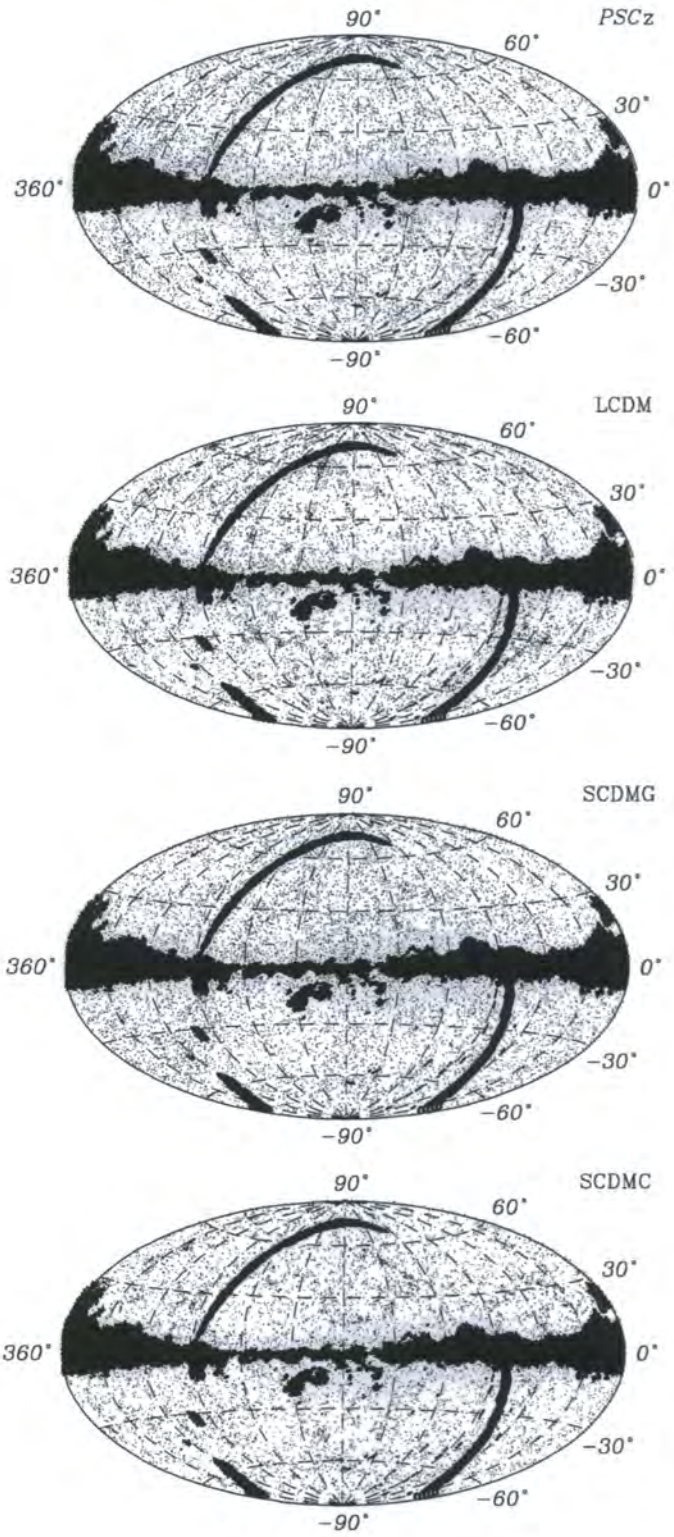

Figure 3.1: Sky distribution of galaxies in the *PSCz* and in three N-body mock-catalogues. From the top to the bottom we illustrate mocks drawn from the LCDM, SCDMG and SCDMC cosmologies, respectively. The Aitoff projection is in Galactic coordinates.

density fluctuation in top hat spheres of radius $8\,h^{-1}$Mpc while the third one is normalised to match the multipole amplitude of the 2 year COBE data (Sugiyama 1995). Galaxies were identified with random particles from the simulations (so that $b = 1$ by construction).

The relevant details of the three cosmological models explored are summarised in Table 3.1 which lists the main cosmological parameters, the bulk flow in a sphere of $100\,h^{-1}$Mpc and the asymptotic 3D velocity dispersion of the unsmoothed and 1.5-TH smoothed peculiar velocity fields (1.5-TH stands for a Top-Hat filter with characteristic radius $1.5\,h^{-1}$Mpc). Prior to generating the mock catalogues, we smoothed the velocities in the simulations using a top hat filter of radius 1.5 h^{-1}Mpc. This brings $\sigma_{12}(1)$, the pairwise velocity dispersion of objects whose projected separation is $\leq 1\,h^{-1}$Mpc, down to ~ 250 km s^{-1}(when only particles within $30\,h^{-1}$Mpc from the observer are considered). This value is in accordance with the recent analysis of the Optical Redshift Survey of Santiago *et al.*(1995, 1996) by Strauss, Ostriker & Cen (1998) for galaxies outside high density regions. A similar agreement is found with $\sigma_{12}(1)$ estimated using only late type galaxies in the Perseus–Pisces redshift catalogue (Guzzo *et al.* 1997). Both these observations refer to 'field' galaxies, and therefore compare well with the late type *IRAS* galaxies of the *PSCz*catalogue.

Ten different mock catalogues, which we will refer to as LCDM0i, SCDMG0i, and SCDMC0i, $\{i = 0, ..., 9\}$, have been extracted from each of the above models. Since the main purpose of those mocks is to test the *intrinsic* reliability of the reconstruction methods we have identified the galaxies with the particles in the simulations. This makes effective the assumption that galaxies trace the mass.

To extract a generic *PSCz* mock catalogue we have adopted the following procedure :

- A population of particles with properties similar to those of the Local Group (LG) is identified. A LG-like observer is defined by implementing three observationally based constraints: the peculiar velocity of the point must be $\mathbf{v}_{LG} = 625 \pm 25$ km s^{-1}, and the particle must be located in a region for which the fractional overdensity δ averaged in a radius of $5\,h^{-1}$Mpc is in the range $-0.2 < \delta < 1.0$. Furthermore, we require the shear in the same volume to be small, $|\mathbf{v}_{LG} - \langle \mathbf{v} \rangle| \leq 0.3|\mathbf{v}_{LG}|$, where $\langle \mathbf{v} \rangle$ is the mean velocity within the averaging sphere (Brown & Peebles 1987). A subset of these 'observers' have been selected with the further observational constraint of having a cluster of galaxies with size comparable to an Abell richness class 1 (i.e. the Virgo cluster), in a distance range $10\,h^{-1}$Mpc $< d < 20\,h^{-1}$Mpc from the observer.

- A sphere of $120\,h^{-1}$Mpc radius is drawn around the LG-like observer and the whole frame is rotated so that the motion of the observer is in the direction ($l = 276°, b = 30°$), the direction of the LG peculiar velocity with respect to the CMB frame (e.g. Wilkinson 1988).

- A friends-of-friends algorithm is implemented to find galaxy clusters. The clusters

are identified in real space using a linking length of ~ 0.2 times the average inter-particle separation, $\bar{n}^{-1/3}$, in the simulation. To guarantee that the same number of clusters is selected (chosen to match the spatial density of Abell richness 1 clusters) the minimum allowed number of particles in each cluster varies for the different simulations according to their cosmology. For LCDM, SCDMG and SCDMC we use 180, 40 and 200 particles, respectively, which leads to a spatial density of mock clusters similar to the one observed for the Abell-ACO richness ≥ 1 clusters (Abell 1958).

- The number density of particles in the simulation is $\sim 0.039\ h^3\mathrm{Mpc}^3$ while the number density given by the *PSCz* selection function exceeds this density closer than some critical distance. Thus, the simulations are volume-limited for distances less than $10.9\,h^{-1}\mathrm{Mpc}$, where the *PSCz* number density (Saunders *et al.* 1999) matches the N-body one. For distances greater than this the simulated surveys follow the *PSCz* number density.

- A Monte Carlo rejection was used to choose particles according to the *PSCz* selection function (Saunders *et al.* 1999). We have fitted this selection function with the Yahil *et al.* (1991) functional form for $r \geq 10.9\,h^{-1}\mathrm{Mpc}$:

$$\phi(r) = \left(\frac{r_o}{r}\right)^{2\alpha} \left(\frac{r_\star^2 + r_o^2}{r_\star^2 + r^2}\right)^{\beta}. \tag{3.1}$$

  The optimal parameters are listed in Table 3.2. For $r \leq 10.9\,h^{-1}\mathrm{Mpc}$ the mock catalogues are volume-limited and thus $\phi(r) = 1$. A random flux consistent with the *PSCz* selection function is then attributed at each selected galaxy.

- Despite of the large sky coverage, *PSCz* is not a full-sky catalogue. Unsurveyed regions are present both at high and low galactic latitudes that need to be accounted for to properly reproduce the existing observational biases. We have therefore rejected all the galaxies in these masked areas causing the final sky coverage to be $\approx 84\%$ complete.

- As a final step we accounted for the well known lack of early type galaxies in the original *IRAS* galaxy sample which causes large overdensities to be underestimated. To mimic this bias we define the "field population" to be all those galaxies not belonging to clusters. We assume that in the field the fraction of early type galaxy is constant ($\leq 10\%$, according to Dressler 1980). In clusters we assume instead that the average early type fraction is $\sim 40\%$. Thus we mimic the *IRAS* morphological bias by Monte Carlo rejecting the appropriate fraction of points in clusters.

The final mock catalogue contains the positions of the galaxies in redshift-space and their "observed" flux. The galaxy redshifts are assigned by adding the line-of-sight component of the peculiar velocity to the recession velocity. Fig. 3.1 shows the Aitoff projection of the *PSCz* sample (upper panel) compared with three mock catalogues extracted from the LCDM, SCDMG and SCDMC N-body simulations.

Table 3.2: Selection Function Parameters for Eqn. (3.1)

α	β	$r_\circ$ $[h^{-1}\mathrm{Mpc}]$	$r_\star$ $[h^{-1}\mathrm{Mpc}]$
0.53	1.90	10.90	86.40

3.3 The Reconstruction Methods

By reconstruction we mean a phenomenological procedure through which, starting from the galaxy redshift distribution, we attempt to recover the true cosmic overdensity and velocity fields. These methods comprise of two steps. First, we have to account for the unobserved parts of the sky: *Geometrical Reconstruction.* Second, as we have seen in § 2 the clustering pattern is systematically different from the true clustering since we are considering galaxies at their redshift positions. To obtain the real-space galaxy distribution we need to make some assumptions about the underlying dynamics which have given rise to the velocities: *Dynamical Reconstruction.*

3.3.1 Geometrical Reconstruction

The *PSCz* redshift survey covers 84% of the sky, and it is necessary to model the remaining 16%. We do this by adding galaxies within the regions which are not included in the survey. In the *PSCz* survey there are two kinds of region: the high-latitude regions, $|b| > 8°$ and the Galactic strip $|b| < 8°$. Both the Perseus-Pisces and Hydra-Centaurus superclusters appear to extend across the Galactic plane (Dressler 1988, Kraan-Korteweg *et al.* 1996). This motivates us to apply a scheme to clone the structures in the neighbourhood of the plane. Thus we adopt an improved version of the procedures used by Yahil *et al.* (1991) and Branchini & Plionis (1996). The masked regions at $|b| > 8°$ are filled randomly by a population of synthetic objects whose mean number density $\bar{n}$ is derived from the observed part of the sky. In order to measure the mean density we used

$$\bar{n} = \frac{1}{V} \sum_i \frac{1}{\phi(r_i)}, \tag{3.2}$$

where the sum is over all the galaxies within the sample volume V (Davis & Huchra 1982). We then divide the Galactic strip in 36 bins of 10° in longitude. In each of these bins we divide the radial distances range into bins of $1000\,\mathrm{km\,s^{-1}}$. The synthetic galaxies are sampled from a homogenenous distribution with mean number density $\bar{n}$ set equal to the mean number density in the corresponding longitude/distance bins in the two adjacent

strips $15° > |b| > 8°$. The number of synthetic galaxies in each bin is set equal to a random Poisson deviate whose mean equals the expected number. Finally, the few real galaxies within the $|b| < 8°$ are used to replace an equal number of synthetic objects located at their observed positions.

3.3.2 Dynamical Reconstruction

The purpose of the Dynamical Reconstruction is to eliminate the redshift space distortions and to recover the particles' position in real space along with their peculiar velocities. In the following subsections we describe in detail the methods which we are going to use to solve such a problem.

The Iterative Particle Method – Method 1

In linear theory the model velocity field can be obtained by iteratively solving the system of equations:

$$\mathbf{v}(\mathbf{r}) = \frac{H_0\beta}{4\pi}\int d^3\mathbf{r}'\frac{\mathbf{r}'-\mathbf{r}}{|\,\mathbf{r}'-\mathbf{r}\,|^3}\delta^g(\mathbf{r}') \tag{3.3}$$

and

$$H_0\mathbf{r} = cz - \hat{\mathbf{r}}\cdot[\mathbf{v}(\mathbf{r}) - \mathbf{v}_{LG}]\,, \tag{3.4}$$

where $\mathbf{v}(\mathbf{r})$ is the peculiar velocity of a tracer object at the position $\mathbf{r}$; $\mathbf{v}_{LG}$ is the peculiar velocity of the Local Group; while $\beta \approx \Omega^{0.6}/b$ and b the biasing parameter. During each iteration, the selection function, ϕ, and the mean number density, $\bar{n}$, of the population of displaced objects are recomputed. Eqn (3.3) is only valid in the linear regime and so the force field needs to be smoothed so as to eliminate nonlinear effects. We adopt a "top hat" filter with a smoothing radius

$$r_{sm}(r) = max\left\{5, [\bar{n}\phi(r)]^{-\frac{1}{3}}\right\}\ h^{-1}\mathrm{Mpc} \tag{3.5}$$

This choice eliminates most of the nonlinear contributions and keeps the shot noise at a constant level. To improve numerical convergence we slowly, "adiabatically", increase the value of β at each of ten iterations, from 0.1 to 1.0 (Strauss *et al.* 1992). The resulting model velocity field does not depend on the input value of β since, to first order, the amplitude of the velocity vectors scales linearly with β. In spite of the smoothing applied some nonlinear effects may remain. For example, around high density regions, such as clusters, there may be triple–valued regions in which the same redshift is observed at three different positions along a given line-of-sight. We correct for this by collapsing the galaxies within clusters and implementing Yahil *et al.* (1991) "robust procedure" (their "method 2") to handle galaxy positioning inside triple–valued regions.

The Direct Particle Method – Method 2

This procedure is based on the method proposed by Nusser and Davis (1994). In linear theory, the velocity field in redshift space is irrotational and thus may be derived from a velocity potential:

$$\mathbf{v}(\mathbf{s}) = -\nabla\Phi(\mathbf{s}). \tag{3.6}$$

Therefore, if one expands the potential and the galaxy overdensity field, δ^g, in spherical harmonics, and uses the Zel'dovich approximation (Zel'dovich 1970), then the two fields obey a Poisson–like equation:

$$\frac{1}{s^2}\frac{d}{ds}\left(s^2\frac{d\Phi_{lm}}{ds}\right) - \frac{1}{1+\beta}\frac{l(l+1)\Phi_{lm}}{s^2} = \frac{\beta}{1+\beta}\left(\delta^g_{lm} - \frac{1}{s}\frac{d\ln\phi}{d\ln s}\frac{d\Phi_{lm}}{ds}\right), \tag{3.7}$$

where δ^g_{lm} and Φ_{lm} are the spherical harmonic coefficients of the galaxy density and velocity potential fields, respectively. These coefficients are given by

$$\delta^g_{lm}(s) = \int \delta^g(\mathbf{s})Y^*_{lm}(\hat{\mathbf{s}})d\Omega \qquad \Phi_{lm}(s) = \int \Phi(\mathbf{s})Y^*_{lm}(\hat{\mathbf{s}})d\Omega \tag{3.8}$$

in redshift shells; where * denotes complex conjugate and $Y_{lm}, (l = 0, .., \infty; |m| \leq l)$ are the spherical harmonics (*cf.* Jackson 1962). The integrals in eqns. (3.8) are computed over 4π steradians in 72 bins in redshift space out to 17 000 km s^{-1}. The radial bin size increases in proportion to the *IRAS PSCz* inter-particle spacing $[\bar{n}\phi(s)]^{-1/3}$. The Gaussian-smoothed galaxy density field at a grid point n is given by

$$1 + \delta^g(\mathbf{s}_n) = \frac{1}{(2\pi)^{3/2}r^3_{sm,n}}\sum_i \frac{1}{\phi(s_i)}\exp\left[-\frac{(\mathbf{s}_n - \mathbf{s}_i)^2}{2r^2_{sm,n}}\right] \tag{3.9}$$

where the sum is over all particles in the catalogues. The smooth width for the cell n, $r_{rm,n}$ is equal to

$$r_{sm}(s_n) = max\left\{3.2, 0.64\,[\bar{n}\phi(s_n)]^{-\frac{1}{3}}\right\}\ h^{-1}\mathrm{Mpc}. \tag{3.10}$$

Since $\delta^g_{lm}(\mathbf{s})$ is known in redshift shells, we then solve eqn. (3.7) for $\Phi_{lm}(\mathbf{s})$, and then compute the full three–dimensional velocity field in redshift space using eqn. (3.6). Galaxy positions and peculiar velocities at the real-space positions, $\mathbf{r}$, are obtained by assuming a one-to-one mapping between $\mathbf{r}$ and $\mathbf{s}$ along the line-of-sight. We minimize the problem of triple–valued regions by adopting the same cluster–collapsing scheme as Yahil *et al.* (1991) for collapsing the fingers of God associated with the clusters present in the simulation.

We reconstruct the overdensity and peculiar velocity field from the mock catalogues by summing over the harmonics up to $l_{\max} = 15$

$$\delta(\mathbf{s}) = \sum_{l=0}^{l_{\max}}\sum_{m=-l}^{l}\delta_{lm}(s)Y_{lm}(\hat{\mathbf{s}}), \qquad u(\mathbf{s}) = \sum_{l=0}^{l_{\max}}\sum_{m=-l}^{l}u_{lm}(s)Y_{lm}(\hat{\mathbf{s}}) \tag{3.11}$$

in angle. This truncation is going to introduce uncertainties in the velocity model: if the expansion is terminated at a low order, structures on a smaller angular scale than the wavelength of the highest harmonic, $\frac{\pi}{l_{\max}}$, will be lost. On the other hand, if the expansion

is continued to a high order, we risk introducing artefacts on scales smaller than the real structures.

Redshift space distortions are only one of several effects that hamper the recovery of cosmic density and velocity fields from observational data. Another source of random and systematic error is the radial selection function which, when coupled to redshift distortions, generates the so called 'rocket effect' discussed by Kaiser and Lahav (1989). This is a spurious acceleration measured from a magnitude-limited sample of galaxies by an observer who has a peculiar velocity unrelated to the true gravitational acceleration. In Method 1 this effect is quantified and corrected for using the mock catalogues discussed below. In Method 2 the rocket effect is explicitly accounted for by the second term in the right hand side of eqn. (3.7).

3.4 Comparing the Methods: the basic tests

3.4.1 The Inferred Radial Density Field

The density field of our N-body models will differ from the true density field of the original cosmological simulation because of three effects: the dilute sampling, errors in the estimation of the mean number density and selection function, and in the predicted velocity field. It is important to quantify such errors because we are interested in comparing the *PSCz* reconstructed density field with that infered from velocity surveys.

We estimate the radial number density, $n(r) \equiv \bar{n}\phi(r)$, in 34 equally spaced bins up to $17\,000\,\mathrm{km\,s^{-1}}$. To estimate $n(r)$ in a bin between r and $r + \Delta r$ we consider

$$n(r) = \frac{1}{\omega\,\Delta r\,r^2} \sum_{i=1}^{N_p} W_n(r, \mathbf{r}_i, \Delta r), \tag{3.12}$$

where $W_n(r, \mathbf{r}_i, \Delta r) \equiv H(r - r_i)H(r_i - r - \Delta r)H(|b_i| - 10°)$, $H(x)$ represents the Heavyside function defined as 1 for $x \geq 0$ and 0 otherwise, ω is the solid angle of the region on the sphere $0° \leq b < 360°$, $|b| > 10°$ while N_p is the number of particles included in the catalogue.

3.4.2 The Reconstructed Dipole

If the CMB defines a cosmological frame, then the dipole pattern observed in its temperature is a direct measure of the LG velocity, $V_{LG} = 627 \pm 22\,\mathrm{km\,s^{-1}}$ towards $(l, b) = (276° \pm 3°,\ 30° \pm 2°)$ (Lineweaver *et al.* 1996), via Doppler shift. Although other interpretations are possible (Paczyncki & Piran 1990) the velocity interpretation of the CMB dipole is the most popular. This is due to the remarkable alignment of the dipole vector with the gravitational acceleration vector measured at the LG location. The gravitational

acceleration is estimated from the distribution of luminous objects in our cosmological neighourhood. Within the linear Gravitational Instability (Peebles 1980) and linear biasing framework we expect that in the linear regime velocity, $\mathbf{v}(\mathbf{r})$, and gravity, $\mathbf{g}(\mathbf{r})$ are parallel and related by equation (*cf.* § 1).

$$\mathbf{v}(\mathbf{r}) = \frac{H_0 f}{4\pi G}\mathbf{g}(\mathbf{r}), \tag{3.13}$$

where f is the linear growing factor, $f \equiv \Omega^{0.6}$. The vector $\mathbf{g}(\mathbf{r})$ is related to the mass density field, δ_ρ by

$$\mathbf{g}(\mathbf{r}) = G\int \delta_\rho(\mathbf{r}')\frac{\mathbf{r}'-\mathbf{r}}{|\mathbf{r}'-\mathbf{r}|^3}d^3\mathbf{r}' \tag{3.14}$$

Since we sample the distribution of galaxies rather than the mass distribution

$$\mathbf{V}_{LG}(r) = \frac{H_0\beta}{4\pi}\sum_{i=1}^{N_p}\frac{W_{LG}(r,r_i)}{\phi(r_i)}\frac{\mathbf{r}}{|\mathbf{r}|^3}. \tag{3.15}$$

The window function, $W_{LG}(r,r_i,r_0) \equiv H(r-r_i)H(r_i-r_0)$ where $r_0 = 500\,\mathrm{km\,s^{-1}}$.

The main sources of uncertainty are: a) Finite sample size. The estimated dipole is a sum over the number of objects within the survey. The volume sampled is thus finite since it extends to the maximum depth of the survey and excludes possible unsurveyed regions. b) Shot noise. At large radii, the sampling of the galaxy distribution becomes more and more sparse. This leads to an increase in the shot noise. c) Modelling of the velocity field. The redshift surveys do not provide us with information on the actual position of the particles but rather their redshift coordinates in redshift space. d) Nonlinear effects. The estimator applied is only valid over the entire volume of the survey and is inaccurate where the density field is high. Nonlinear contributions to peculiar velocities add incoherently to the vector, spoiling the linear relation between velocity and acceleration vectors.

3.4.3 The reconstructed Bulk Flow

In this section we consider the peculiar velocity, $\mathbf{V}_B(r)$, of spheres of radius r centred on the Local Group. This is a low order statistic that can readily be estimated observationally and which has a theoretical counterpart. The expectation value of the bulk velocity, $|\mathbf{V}_B|$, averaged over scale r is:

$$\langle|\mathbf{V}_B(r)|^2\rangle = \frac{\beta^2}{2\pi^2}\int P(k)\widetilde{W}^2(kr)dk, \tag{3.16}$$

where $P(k)$ is the power spectrum of density fluctuations. The window function

$$\widetilde{W}(kr) = 3\,\frac{[\sin(k\,r) - k\,r\cos(k\,r)]}{(k\,r)^3}, \tag{3.17}$$

is the Fourier transform of the spherical top hat window function in real-space which is chosen to allow a straightforward comparison between the theoretical definition eqn. (3.16) and

its observational analogue eqn. (3.18). If the initial fluctuation field obeys Gaussian statistics, then evolution through gravitational instability preserves a Gaussian distribution for the amplitude of each Cartesian component of $\mathbf{V}_B(r)$, so that $|\mathbf{V}_B(r)|$ has a Maxwellian distribution. This property makes it difficult to constrain $P(k)$ from the measured $\mathbf{V}_B(r)$. Nevertheless, comparison of the measured $\mathbf{V}_B(r)$ with the velocities predicted from a redshift survey gravity field allows, in principle, an estimate of the β parameter. We estimate $\mathbf{V}_B(r)$ from the galaxy reconstructed positions and peculiar velocities, in the CMB frame, considering the following estimator:

$$\mathbf{V}_B(r) = \sum_{i=1}^{N_p} \frac{\mathbf{v}_i\, W_B(r, r_i)}{\phi(r_i)} \Bigg/ \sum_{i=1}^{N_p} \frac{W_B(r, r_i)}{\phi(r_i)}. \tag{3.18}$$

Here the sum is over all sources within the catalogue while $W_B(r, r_i) \equiv H(r - r_i)$. This estimator is prone to systematic errors rising mainly from two sources: a) the filling–in procedure for the Zone of Avoidance (ZoA). b) The modelling of the LG velocity, $\mathbf{V}_{LG}$. Since the two reconstruction methods introduced in § 3.3 work in the LG frame, the predicted Local Group velocity vector, obtained from the dipole of the galaxy distribution, must be added to the reconstructed velocities. As a result, errors in the determination of the dipole (arising, for example, from shot noise, finite volume and the "rocket effect" as defined in Kaiser 1987 and Kaiser & Lahav 1988) affect the model bulk velocity vector. The uncertainties due to the filling–in procedure may be minimized by restricting attention to the *SGY* component of the bulk velocity.

3.5 Looking for Systematic Effects

Fig. 3.2 shows the reconstucted overdensity field of the mock *PSCz* LCDM8 simulation overdensity field in the "Supergalactic Plane". In panel a) we plot the real-space data smoothed with a Gaussian filter of radius $6\,h^{-1}$Mpc. In panel b) we plot the same as a) but using raw redshift data smoothed with a Gaussian filter of width $6\,h^{-1}$Mpc. The reconstructed overdensity fields are presented in c) and d), Method 1 and 2, respectively. To smooth the fields we apply the same Gaussian kernel as in the two top panels. The ZoA is indicated by the shaded region in panels b), c) and d). The overall impression is that reconstructions show rather good agreement with the real space overdensity field shown a). The major differences are either within the ZoA or at high density regions. In order to check for possible systematic biases in the methods, we show the difference between the reconstructed and true velocities as a function of both distance and density for the same mock catalogue as in Fig. 3.2. In Fig. 3.3 panels a) and c) there does not appear to be any systematic offset in the mean difference as a function of distance within $140\,h^{-1}$Mpc which might, for example, arise if the monopole of the mean number density was in error. Beyond $150\,h^{-1}$Mpc Method 1 systematically overpredicts the radial velocity field, which we believe is largely due to an edge effect. In the panels b) and d) of the same figure, we plot the same velocity differencies, but now as a function of the reconstructed

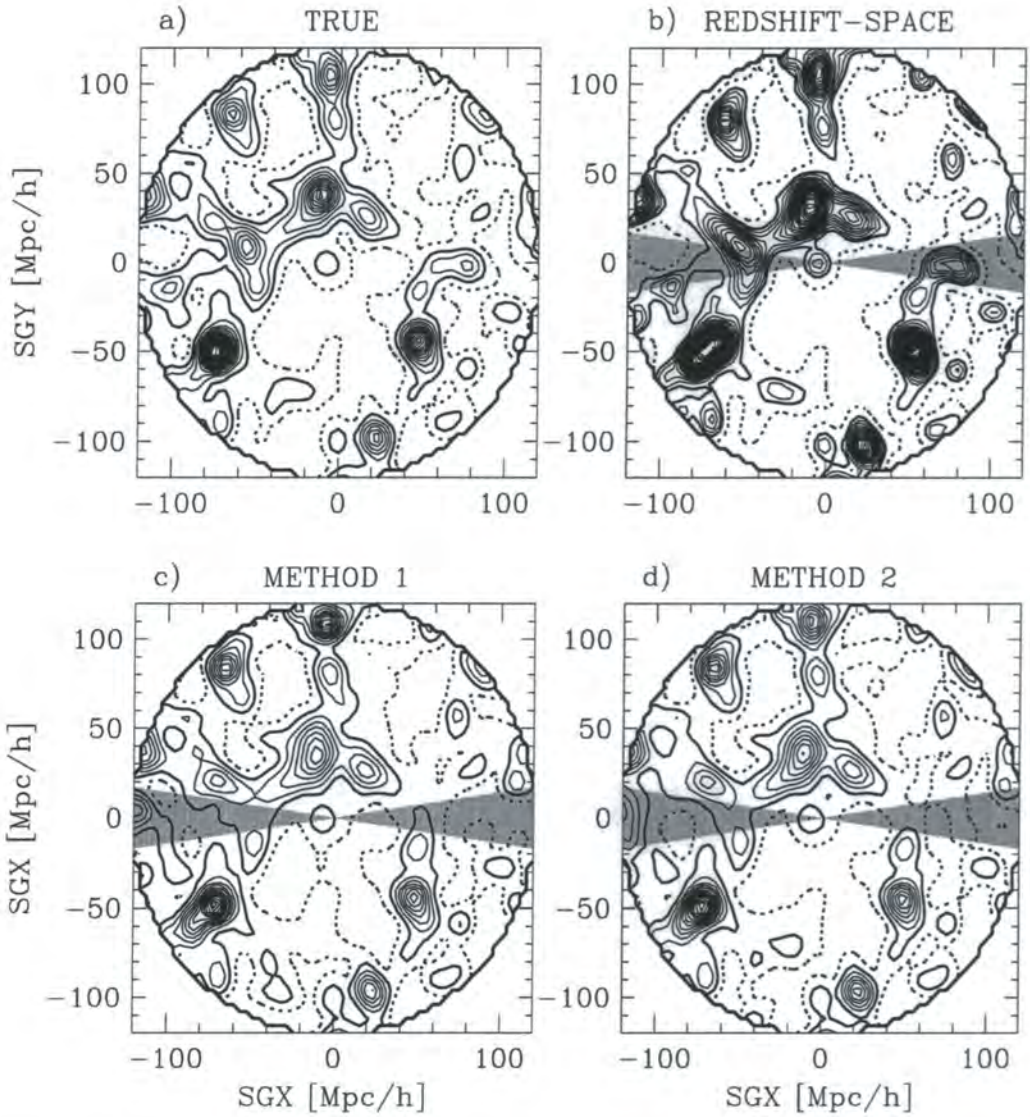

Figure 3.2: Reconstructions of the mock *PSCz* LCDM8 simulation overdensity field in the "Supergalactic Plane". All contours are spaced at $\delta = 0.5$, with solid (dotted) lines denoting positive (negative) contours. The heavy solid contour corresponds to $\delta = 0$. a) Real-space data smoothed with a Gaussian filter of radius $6\,h^{-1}$Mpc. b) Raw redshift data smoothed with Gaussian filter of width $6\,h^{-1}$Mpc. c) Reconstructed overdensity field by Method 1 smoothed with the same filter as in the two top panels. d) Same as in c), but with Method 2 for reconstructing the positions of the particles. The shaded regions in b), c) and d) represent the ZoA.

overdensity field at the position of each particle. The range of probed overdensities extends well into the non-linear regime, but, no systematic trend is evident. The mean difference is consistent with zero over the entire range of densities shown in the figure.

3.6 Error Analysis

Several different effects prevent our reconstruction procedures from recovering the exact galaxy distribution. And less than perfect reconstructions generate both systematic and random errors on the various estimators used in our analysis. Some estimators are also prone to some sort of systematic bias arising from its own nature (*cf.* Kaiser 1987).

To quantify the random and systematic uncertainties we are going to employ the following procedure: we consider a generic *PSCz* mock catalogue and infer the considered estimator from the true all-sky galaxy distribution in real-space or velocity field. Then, we measure the same estimator from the same catalogue, after applying the reconstruction techniques to obtain the real-space positions or the predicted velocity field. The two estimators are equally affected by shot noise, finite sample size and thus the discrepancies can only be blamed on the intrinsic uncertainties of the schemes applied to reconstruct the fields and to the systematic bias that a given estimator is prone to. For each of the catalogues we compute the difference between the two estimates thereby obtaining an estimate for the systematic error. This is then averaged over our suite of mock catalogues (10-LCDM plus 10-SCDMG). The mean discrepancy represents the cumulative effect of the various systematic errors while the dispersion about the mean quantifies the random errors. Throughout this section we are going to present the results of this procedure applied to the estimators described in § 3.4.

3.6.1 The Error in the Inferred Density Field

The quantity $\Psi(r)$ illustrated in Fig. 3.4 is the average value of the systematic error in the mean number density divided by $3.9 \cdot 10^{-2} h^3 \mathrm{Mpc}^{-3}$, the mean number density of the catalogues. The solid (dashed) line is systematic errors in Method 1 (Method 2). The vertical (diagonal) hatched region is the 1-σ random error Method 1 (Method 2) about the systematic error. Our estimates are only presented outside the volume-limited part of the mock catalogues because within this region our N-body models do not mimic the Local Universe properly. Over the range of radius illustrated in Fig. 3.4 there is no sytematic trend evident in the estimates inferred from the reconstructions. Beyond $15\,h^{-1}\mathrm{Mpc}$ both methods reconstruct the density field with an uncertainty of better than 10 %. The scatter for $r \leq 10.9\,h^{-1}\mathrm{Mpc}$ is $\sim 30\%$ with very little difference between the reconstruction schemes. This error is due to the coupling between $\bar{n}$ and ϕ and it shows how poorly $\bar{n}$ is determined locally since $\phi(r) \equiv 1$ by definition.

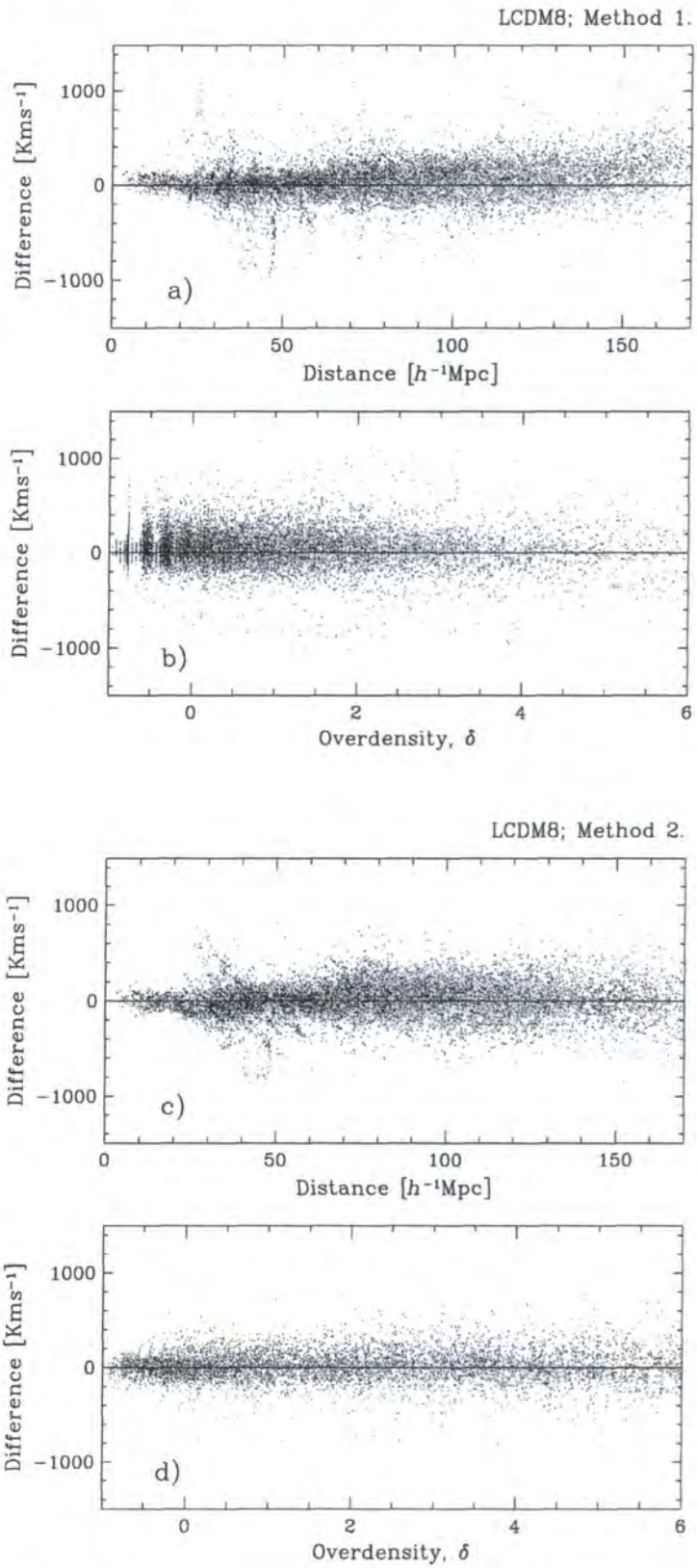

Figure 3.3: a) The difference between the velocity field reconstructed by Method 1 and the true peculiar velocity (in Local Group frame) versus distance for the mock *PSCz* LCDM8 simulation. b) The same velocity differences as in a) shown as function of the velocity field reconstructed overdensity. c) The difference between the velocity field reconstructed by Method 2 and the true peculiar velocity (in Local Group frame) versus distance for the same mock catalogue. d) The same as in b) but for Method 2.

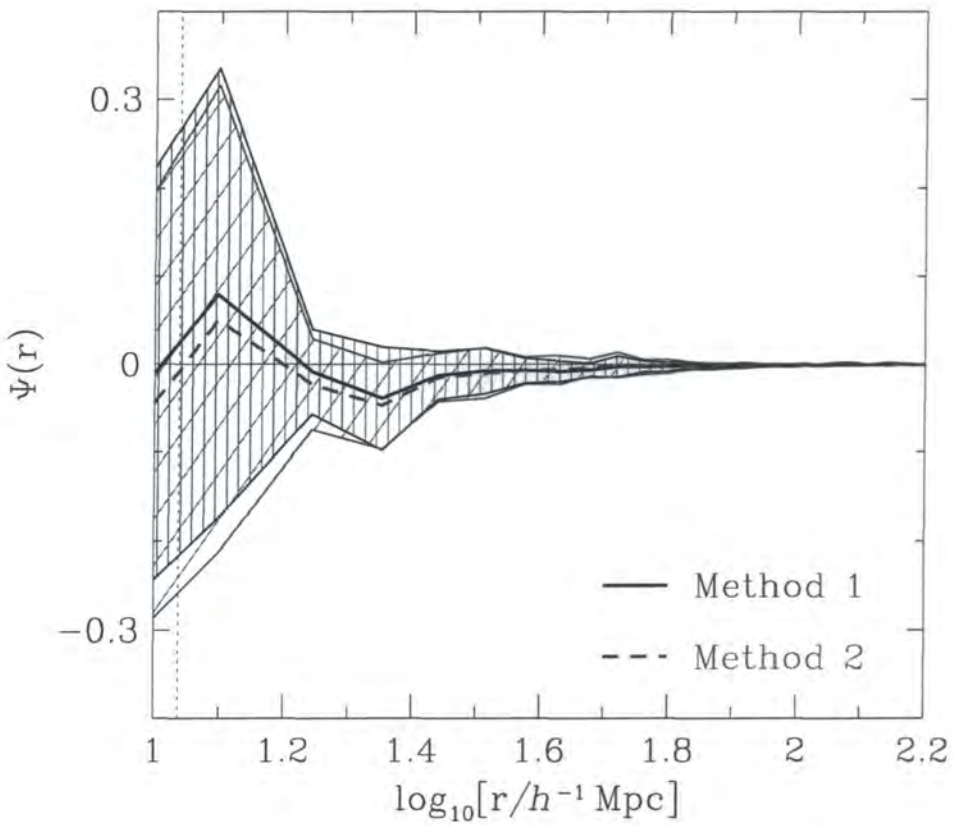

Figure 3.4: Systematic and random errors of the radial density field $n(r)$. The solid (dashed) line illustrate Methods 1 (Method 2) systematic error. We also show the random errors about the respective systematic errors: vertical (oblique) hatched region indicate Method 1 (Method 2) dispersion. Vertical dotted line represents the outermost radius, $r_{VL} = 10.9\,h^{-1}$Mpc, of the volume-limited region of the catalogues.

3.6.2 The Error in The Inferred Dipole

To quantify the uncertainties in the reconstructed dipole, we computed the systematic and random errors of its amplitude, SGY-component and its direction as function of the distance. In the top (bottom) row of Fig. 3.5 we plot the systematic and random errors of the estimators using Method 1 (Method 2). The heavy line (shaded) histograms represent the distribution of systematic errors in the amplitude (SGY-component) at distances of 60 (left column) and $120\,h^{-1}$Mpc (central column). In these estimates there is no evidence of a systematic trend and we are able to reconstruct the dipole of the galaxy distribution with $100\,\mathrm{km\,s^{-1}}$ accuracy. Finally, in the right hand column we show the inferred systematic and random errors in the longitude and latitude of the predicted dipole direction on the sky at 60 (solid circles) and $120\,h^{-1}$Mpc (open circles). The accuracy of the reconstructed dipole direction is $\sim 15°$ over the range of distances probed.

3.6.3 The Error in the Inferred Bulk

To diagnose the uncertainties in the reconstructed bulk flows we calculate the systematic and random errors of its amplitude, SGY-component and its direction as function of the distance. In the top (bottom) row of Fig. 3.6 we plot the systematic and random errors of the estimators using Method 1 (Method 2). The heavy line (shaded) histograms represent the distribution of systematic errors of the amplitude (SGY-component) at the distances of 30 (left column) and $60\,h^{-1}$Mpc (central column). There is a small systematic offset of $\sim 50\,\mathrm{km\,s^{-1}}$ in the amplitude at $60\,h^{-1}$Mpc with a scatter of $\sim 100\,\mathrm{km\,s^{-1}}$. The SGY-component, however, is reconstructed within $80\ \mathrm{km\,s^{-1}}$ and shows no evident systematic trend. This suggests that the offset in the amplitude of the bulk flow is mainly due to the filling-in procedure since from the three components of the reconstructed bulk flow SGY is the least affected by it. The accuracy of the direction of the bulk flow, shown in the right hand column, is $\sim 20°$ in Galactic latitude and roughly twice as much as in Galactic longitude. Once again, this reflects the uncertainties due to the filling-in scheme.

In Fig. 3.7 we extend the analysis of the previous figure to a larger range of depths. The regions of the panels between solid (dotted) lines illustrate the bulk (SGY-component) random error about the systematic error. We confirm the trend already seen in Fig. 3.6: the bulk flow amplitude presents a systematic error of $\sim 50\,\mathrm{km\,s^{-1}}$ which is almost as large as its random error beyond $80\,h^{-1}$Mpc, independently of the reconstruction technique applied. The SGY does show an absence of systematic trend being reconstructed with a ~ 40 (~ 80)$\,\mathrm{km\,s^{-1}}$ for Method 1 (Method 2) accuracy within $120\,h^{-1}$Mpc.

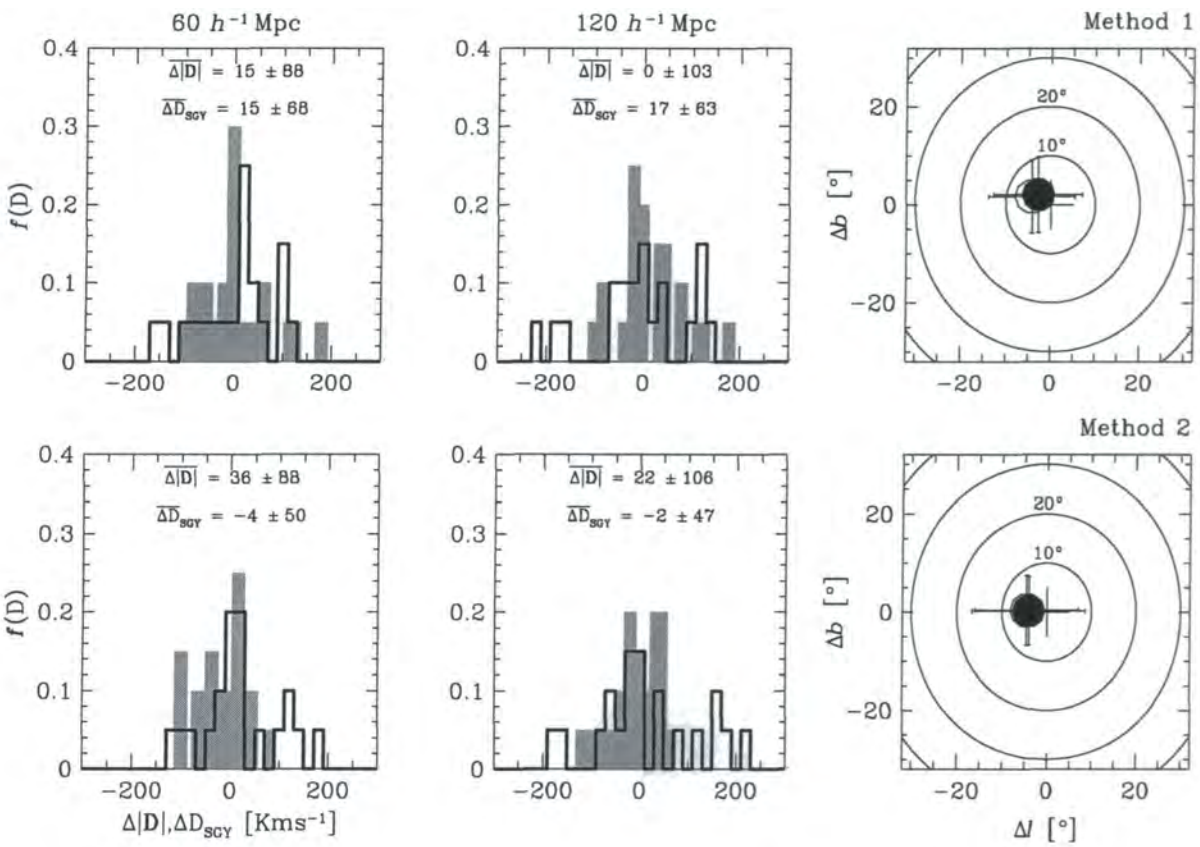

Figure 3.5: Systematic and random errors in the reconstructed dipole amplitude, *SGY*-component and direction on the sky versus distance. The top (bottom) row illustrates the error in the estimates inferred from the Method 1 (Method 2) reconstructions. Left hand (central) column plots the distribution of residuals of the amplitude (heavy line histogram) and *SGY*-component (shaded histogram) at $60\,h^{-1}$Mpc ($120\,h^{-1}$Mpc). The right hand column illustrates the residuals of the dipole directions at $60\,h^{-1}$Mpc (solid dot) and $120\,h^{-1}$Mpc (empty circle).

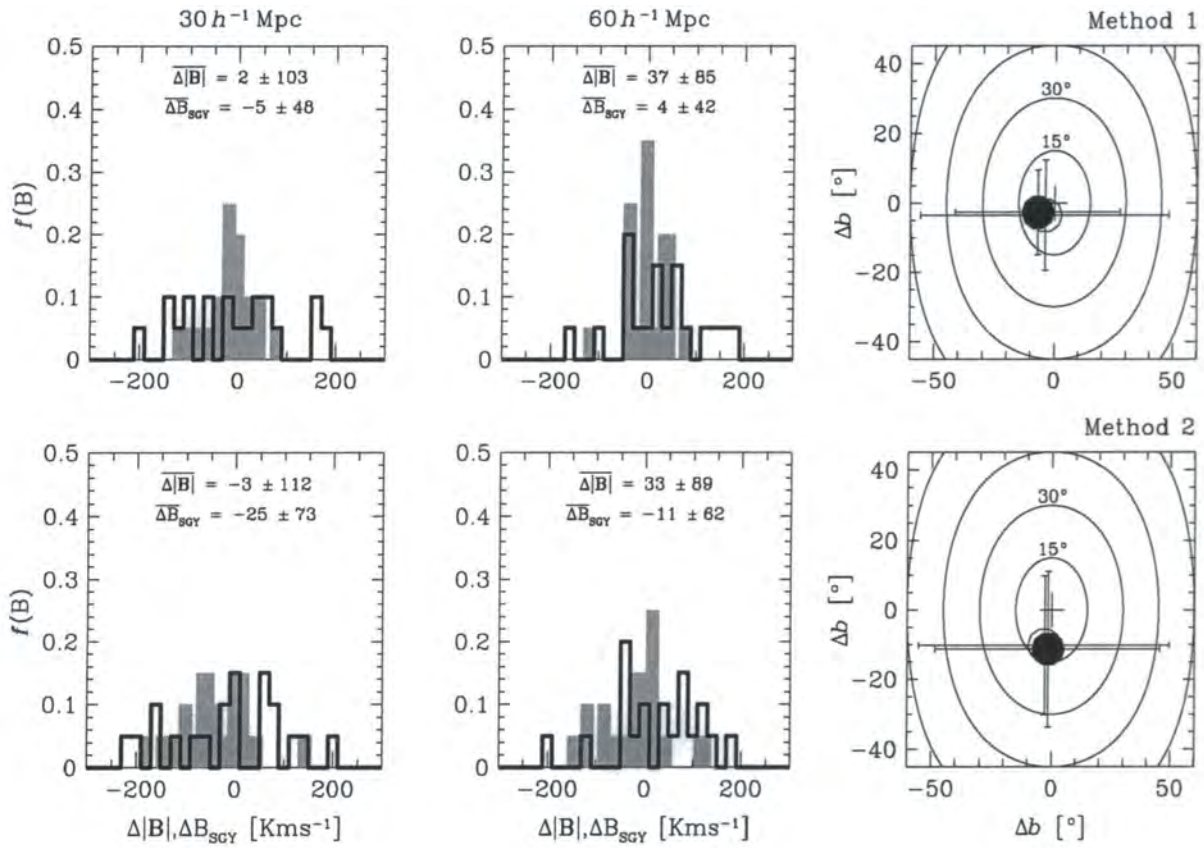

Figure 3.6: Systematic and random errors in the reconstructed bulk flow amplitude, *SGY*-component and direction on the sky versus distance. The top (bottom) row illustrates the error in the estimates inferred from the Method 1 (Method 2) reconstructions. Left hand (central) column plots the distribution of residuals of the amplitude (heavy line histogram) and *SGY*-component (shaded histogram) at $30\,h^{-1}$Mpc ($60\,h^{-1}$Mpc). The right hand column illustrates the residuals of the bulk directions at $30\,h^{-1}$Mpc (solid dot) and $60\,h^{-1}$Mpc (empty circle).

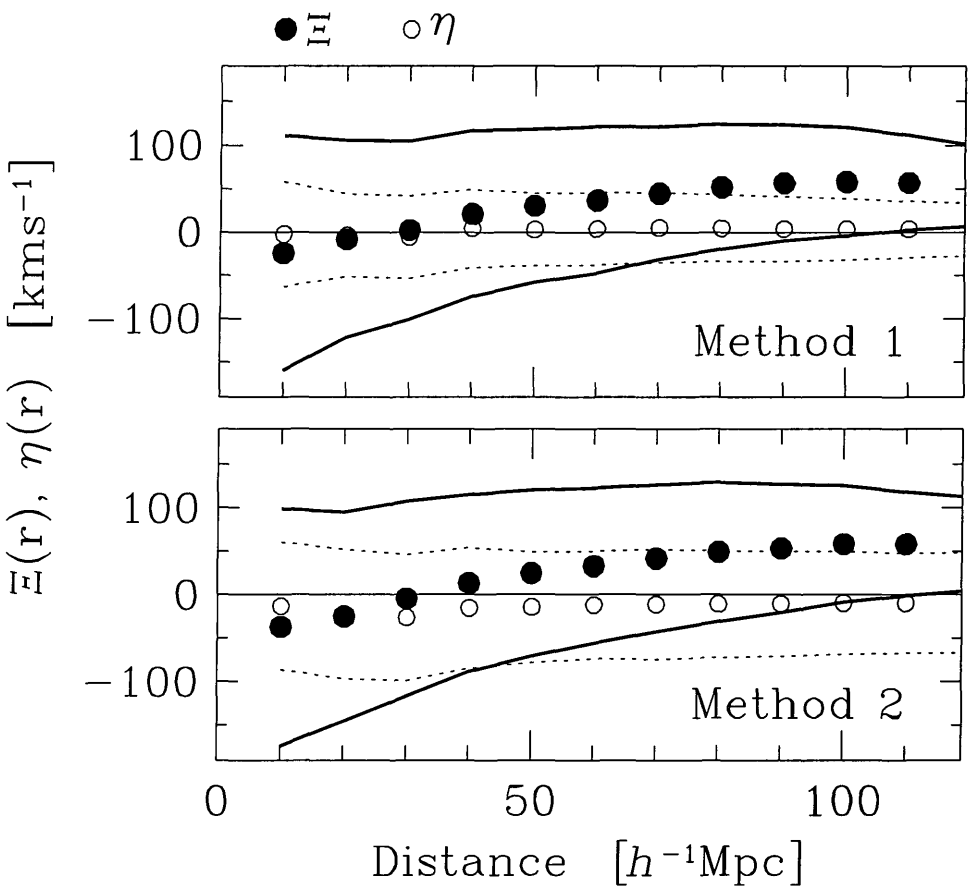

Figure 3.7: Systematic errors of the reconstructed bulk flow amplitude, $\Xi(r)$, and *SGY*-component, $\eta(r)$, versus distance. The top (bottom) panel illustrates such errors inferred from the Method 1 (Method 2) reconstructions. The regions between solid (dotted) lines indicate the 1-σ random errors about $\Xi(r)$ $[\eta(r)]$.

3.7 The v–v comparison.

In the framework of linear gravitational instability and linear bias a detailed comparison of the predicted velocity field with that observed allows one to measure $\frac{\Omega^{0.6}}{b}$. In the context of this chapter, this comparison is applied with the goal of diagnosing the goodness of the velocity field reconstructions. Mock catalogues are drawn from N-body experiments in which the structure grows in response to the self-gravity of fluctuations in a given cosmological background (the various parameters are fixed by ourselves). Thus a comparison between velocities that are the output of an N-body experiment and that are predicted by our geometrical and dynamical reconstruction may give us a clear indication of the intrinsic reliability of these last schemes.

The major sources of error in the predicted velocity field are: a) Non-linear effects: as already mentioned for the reconstructed dipole, non-linear contributions to peculiar velocities add incoherently to the predicted velocity field leading to a systematic bias in the prediction. b) Shot noise: in a flux-limited catalogue the interparticle distance grows with the distance from the origin. Thus, as we sample the underlying density field using galaxies we introduce uncertainties in the peculiar velocity field due to discreteness. c) Volume sampling: the estimate of the velocity field at the position of a probe particle involves an integral (or any other appropriate dynamical prescription) over the entire space. In using a redshift survey with finite depth, we introduce uncertainties in the inferred velocity field. e) Rocket effect: a less than correct selection function when coupled with redshift distortions produces a systematically different inferred velocity field.

We model the real velocity u_r as $u_r = \beta_t u_p + \delta u_r$ where β and δu_r are obtained minimizing a least squares fitting and u_p is the predicted radial velocity field. The scatter around this fitting is named d. In table 3.3 we present β_t, δv_r and d resulting from the following v-v comparisons for the LCDM, SCDMG and SCDMC *PSCz* mock catalogues: 1) T: all galaxies within $120\,h^{-1}$Mpc; 2) R1: all galaxies within $60\,h^{-1}$Mpc; 3) R2: all galaxies between 60 and $120\,h^{-1}$Mpc; 4) D1 all galaxies with $\delta < 1$; 5) D2: all galaxies with $\delta > 1$; 6) O: all galaxies with -1 $< \delta <$ 1 and within $60\,h^{-1}$Mpc.

In table 3.3 we show that when considering all galaxies within $120\,h^{-1}$Mpc the (row 'T' of the respective cosmologies) Method 1 is able to recover the right value of β for the LCDM mock catalogues only, while Method 2 performs well in the context of all cosmologies. Considering only sources within 60 h^{-1}Mpc brings the predicted radial velocity fields of Method 1 into good agreement with the real radial velocities for the SCDMG *PSCz* mock catalogues. An analysis performed with the galaxies within a shell between $60\,h^{-1}$Mpc and $120\,h^{-1}$Mpc shows that Method 1 tends to overpredict the radial velocity field beyond $60\,h^{-1}$Mpc in SCDMG mock catalogues. Considering only galaxies outside δ >1 regions (rows 'D1') does not show an improvement in the estimate of β inferred from the Method 1 SCDMG reconstructions. In high density regions the linear relation between acceleration and velocity is spoilt (linear theory over-predicts the velocity field in these regions). Hence

we do not expect that Method 1 infers the right value of β when considering galaxies within such regions. However, since Method 2 assumes the Zel'dovich approximation to describe the growth of the structure we expect that the parameter β inferred from the Method 2 reconstructions is still similar to the real one. This is confirmed in the various 'D2' rows in the table. Finally, if we only consider galaxies within $60\,h^{-1}$Mpc from the origin and outside regions with $|\delta| > 1$ (rows 'O'), Method 1 predicted velocity fields which have the right value.

3.8 Conclusions

We have estimated the reliability of two methods for modelling the peculiar velocities of galaxies from the observed distribution in redshift space. Our goal is to apply the two algorithms to the recently completed *PSCz* redshift survey. We have created a series of mock *PSCz* catalogues extracted from N–body simulations of different CDM cosmologies, carefully designed to reproduce the dynamical properties of our local universe. We cross–calibrate the accuracy of the algorithms by applying them to the mock datasets. The methods reproduce the density field to within 30% within the volume-limited part the catalogues and 10 % in the remaining parts of the sampled volume. The dipole of the mass distribution is also successfuly inferred with a $\sim 100\,\mathrm{km\,s^{-1}}$ accuracy in amplitude and $\sim 15^\circ$ in direction, with no evidence for systematic effects. Similar considerations apply for the direction of the bulk velocity vector. The scatter in its amplitude is $\sim 100\,\mathrm{km\,s^{-1}}$ but with a small systematic offset of $\sim 50\,\mathrm{km\,s^{-1}}$ beyond $\sim 60\,h^{-1}$Mpc. Model velocities can be compared with observed ones to determine the $\beta \approx \Omega^{0.6}/b$ parameter. The distribution of the inferred βs is not offset systematically from the true value of β in our LCDM and SCDMG *PSCz* mock catalogues. These models are however responsible for a random error that can be reduced to a level ≤ 9 and 12% for models predicted by Method 1 and 2, respectively, by excluding large density regions within 60 h^{-1}Mpc from the velocity–velocity comparison.

I	II	Method 1			Method 2		
		$\beta_t \pm \sigma_{\beta_t}$	$\delta v_r \pm \sigma_{\delta v_r}$	$d \pm \sigma_d$	$\beta_t \pm \sigma_{\beta_t}$	$\delta v_r \pm \sigma_{\delta v_r}$	$d \pm \sigma_d$
LCDM	T	0.95±0.10	-30±75	182±16	1.08±0.17	-3±71	172±16
	R1	0.95±0.11	-35±49	157±21	1.06±0.17	-6±45	144±26
	R2	0.95±0.13	-28±105	196±17	1.11±0.19	-3±101	187±15
	D1	0.97±0.11	-34±98	176±18	1.12±0.16	-12±56	124±14
	D2	0.89±0.11	-31±83	218±20	1.04±0.17	8±82	206±20
	O	0.99±0.10	-26±52	131±13	1.13±0.16	-9±48	109±16
SCDMG	T	0.88±0.08	-81±71	200±16	0.99±0.09	-25±50	187±12
	R1	0.92±0.09	-66±51	173±18	1.02±0.07	-17±33	160±14
	R2	0.85±0.08	-95±96	218±19	0.98±0.12	-33±74	206±13
	D1	0.84±0.08	-92±86	223±20	1.04±0.08	-27±37	149±13
	D2	0.81±0.08	-85±79	240±17	0.94±0.09	-9±62	226±16
	O	0.94±0.09	-62±50	155±17	1.06±0.08	-19±30	132±12
SCDMC	T	0.71±0.06	18±69	394±32	0.92±0.11	9±84	356±42
	R1	0.71±0.14	-37±61	363±39	0.87±0.17	-21±63	328±48
	R2	0.70±0.06	68±86	405±43	0.96±0.11	39±109	373±50
	D1	0.74±0.05	33±75	375±27	0.98±0.09	-19±68	282±35
	D2	0.63±0.07	31±71	453±38	0.87±0.14	18±83	395±52
	O	0.76±0.10	-35±66	328±37	0.98±0.12	-31±77	277±39

Table 3.3: Predicted versus real radial velocity in the LG frame as function of the cosmology, distance and overdensity.

Column I
- LCDM: $\Lambda = 0.7$, $\Omega = 0.3$;
- SCDMG: $\Gamma = 0.25$;
- SCDMC: Standard CDM COBE normalized.

Column II
- T: all galaxies within $120\,h^{-1}$Mpc;
- R1: all galaxies within $60\,h^{-1}$Mpc;
- R2: all galaxies between 60 and $120\,h^{-1}$Mpc;
- D1: all galaxies with $\delta_5 < 1$;
- D2: all galaxies with $\delta_5 > 1$;
- O: all galaxies with $-1 < \delta_5 < 1$ and within $60\,h^{-1}$Mpc.

Chapter 4

The *PSCz* velocity and density fields

4.1 Introduction

The art of modelling the cosmic velocity field, which originates from the desire to interpret observed deviations from a uniform Hubble expansion, has developed rapidly over the past few years. There are two main reasons for this. One is an increase in the quantity and quality of measured galaxy peculiar velocities. The other is the advent of near all–sky, flux–limited, redshift surveys that allow self–consistent theoretical predictions to be made with the requisite accuracy.

Although other possibilities have been proposed (e.g. Babul *et al.* 1994), the gravitational instability theory (Peebles 1980) has proven to be the most successful theoretical framework in which to interpret peculiar velocities in relation with inhomogeneities in the mass distribution. Early attempts to account for observed velocities within this general framework were rather simplistic due to incomplete knowledge of the distribution of galaxies in the local universe. Thus, simple parametric models were developed to account for cosmic flows in terms of infall onto one or more spherical overdensities like the Virgo Cluster, the Great Attractor or the Perseus–Pisces supercluster (Davis & Peebles 1983, Lynden–Bell *et al.* 1988, Peebles 1988, Han & Mould 1990). The situation changed dramatically when statistically complete, near all–sky, redshift catalogues of galaxies were constructed as it then became possible to predict peculiar velocities directly, assuming that luminous objects trace the underlying density field in some fashion. Since then, several modelling procedures have been developed which are generally based on the simplifying assumption that the gravitating mass is distributed just like the tracer objects (galaxies or clusters), although the relative amplitude of the deviations from uniformity, usually called the bias, is taken to be a free parameter. In addition to this "linear bias model", current methods also assume gravitational instability in the linear or mildly nonlinear regime (e.g. Yahil *et al.* 1991, Kaiser *et al.* 1991, Nusser & Davis 1994, Fisher *et al.* 1995b, Sigad *et*

al. 1998), therefore requiring smoothing over scales where non-linear effects are important. This requires the additional assumption that smoothing a distribution that has evolved to a nonlinear state gives a result that can be modelled by linear or quasilinear evolution from smoothed initial conditions.

Because of their large sky coverage, the most extensively used redshift surveys are those based on the "Point Source Catalogue" (PSC) of *IRAS* galaxies (e.g. the 1.9 Jy survey of Strauss *et al.* 1990, the 1.2-Jy catalogue of Fisher *et al.* 1995a, or the deeper but sparser QDOT survey of Rowan-Robinson *et al.* 1990). Other catalogues containing different kinds of objects such as optically selected galaxies (e.g. Shaya, Tully and Pierce 1992, Hudson 1994b, Baker *et al.* 1998) or clusters of galaxies (Branchini & Plionis 1996) have also been used to produce model velocity fields on scales up to $200\,h^{-1}$Mpc.

Comparison of a model velocity field with directly measured peculiar velocities provides a means to constrain the density parameter, Ω_m. It also tests the gravitational instability hypothesis and the assumed biasing scheme. A successful model for the peculiar velocity field may be used to recover the distribution of galaxies or clusters in real space, directly from their measured redshift. This, in turn, allows investigation of the statistical properties of the objects' distribution, free from the effects of redshift space distortions. Overall, model velocity fields constructed using different surveys have proved to be remarkably consistent with one another (Baker *et al.* 1998) and have been successful in reproducing most of the characteristics exhibited by maps made directly from observed peculiar velocities. There are, however, two major exceptions: the large bulk motion on very large scales claimed by Lauer & Postman (1994; LP94) and a prominent feature in the *Mark*III catalogue of peculiar velocities compiled by Willick *et al.* (1997a) at distances larger than $30\,h^{-1}$Mpc, consisting of a strong shear in the Hydra–Centaurus region (Davis, Nusser and Willick 1996).

Here we present a new nonparametric model for the cosmic velocity field based on the recently completed *PSCz* survey of *IRAS* galaxies. This is the last of the near all-sky redshift surveys based on the *IRAS* catalogue and supersedes both the 1.2-Jy and the QDOT catalogues which it contains. The denser sampling and lower flux limit of the *PSCz* survey allows one to model the peculiar velocity field to large scales without excessive shot noise.

The outline of this chapter is as follows. In § 4.2 we describe the *PSCz* dataset as well as two other redshift catalogues that we use to construct independent model velocity fields. Two methods for generating the *PSCz* peculiar velocity fields have been implemented in order to keep track of systematic errors. These are presented in § 4.3, together with a detailed error analysis. A cosmographic tour is performed in § 4.4 along with a consistency check between the two *PSCz* velocity models and a comparison between the *PSCz* and 1.2-Jy model velocity fields. In § 4.5 we take advantage of the large depth of the *PSCz* survey to compare the gravity field derived from it with the one computed from the distribution of

Abell/ACO clusters. An estimate of the parameter $\beta \simeq \Omega_m^{0.6}/b$, where b is the linear bias parameter of *IRAS* galaxies, is obtained in § 4.6 by comparing observed and predicted bulk velocity vectors. In § 4.7 we discuss our results further and summarize our main conclusions.

4.2 The Datasets

The main dataset used in this work is the recently completed *PSCz* redshift survey described in detail by Saunders *et al.* (1999). The main catalogue contains some 15,500 *IRAS* PSC galaxies with 60 μm flux, f_{60}, greater than 0.6 Jy. To avoid cirrus contamination only PSC objects with $f_{100} < 4f_{60}$ were selected. Stars were excluded by requiring that $f_{60} > 0.5f_{25}$. For our purposes, one of the most important properties of the *PSCz* catalogue is its large sky coverage. The only excluded regions are two thin strips in ecliptic longitude that were not observed by the *IRAS* satellite, the area in the galactic plane where the V–band extinction exceeds 1.5 magnitudes, and a few small isolated spots on the celestial sphere. Overall, the *PSCz* catalogue covers $\sim 84\%$ of the sky. Although we will occasionally consider galaxies with recession velocity as large as 30000 $\mathrm{km\,s^{-1}}$, for the most part we will use the *PSCz* subsample within 20000 $\mathrm{km\,s^{-1}}$, containing 11206 objects. The distribution on the sky of *PSCz* galaxies in shown in galactic coordinates (Aitoff projection) in the upper part of Fig. 3.1. The lower part of Fig. 3.1 shows ΛCDM, SCDMG and SCDMC *PSCz* mock catalogues (for more details of these mock catalogues see § 3.2).

For comparison purposes, we have also applied our analysis to the similar, but shallower, *IRAS* 1.2-Jy redshift survey (Fisher *et al.* 1995a). Galaxies in this catalogue were selected from the same *IRAS* PSC but using a higher (ADDscan) flux limit, $f_{60} > 1.2$ Jy, and different criteria for minimizing contamination by galactic cirrus. This catalogue has a somewhat larger sky coverage of $\sim 88\%$. Here we will use the 4939 *IRAS* 1.2-Jy galaxies within 20000 $\mathrm{km\,s^{-1}}$of the Local Group.

Finally, in an attempt to extend our analysis, we use a completely different set of mass tracers consisting of a volume–limited sample of optically–selected galaxy clusters extracted from the Abell (1958) and the Abell, Corwin & Olowin (1989; hereafter ACO) catalogues. These were cross–calibrated according to the prescription described by Branchini and Plionis (1996; hereafter BP96). The sample has a limiting depth of $250\,h^{-1}$Mpc and contains 493 clusters of richness class $R \geq 0$ at $|b| \geq 13°$, and $m_{10} < 17$, where m_{10} is the magnitude of the tenth brightest galaxy in the cluster.

The number of galaxies in a flux limited sample decreases with distance, as may be seen in Fig. 4.1 for the *PSCz* (upper histogram) and 1.2-Jy (lower, shaded histogram) surveys. We define a selection function, $\phi(r)$, as the fraction of galaxies that can be seen out to a redshift distance $r = cz/H_o$ (expressed in h^{-1}Mpc). To determine $\phi(r)$ we use

Table 4.1: Selection Parameters: *IRAS* Galaxies

Sample	α	β	r_s	$r_\star$	$\bar{n}$
z-*IRAS PSCz*	0.55	1.83	6.0	87.00	$6.22 \cdot 10^{-2}$
R-*IRAS PSCz*	0.52	1.92	6.0	90.75	$5.52 \cdot 10^{-2}$
z-*IRAS* 1.2-Jy	0.49	1.80	6.0	72.90	$5.21 \cdot 10^{-2}$
R-*IRAS* 1.2-Jy	0.47	1.87	6.0	52.50	$4.61 \cdot 10^{-2}$

the parametric maximum likelihood estimate proposed by Yahil *et al.* (1991), in which the following analytic form for the selection function is assumed:

$$\phi(r) = \left(\frac{r_s}{r}\right)^{2\alpha} \left(\frac{r_\star^2 + r_s^2}{r_\star^2 + r^2}\right)^{\beta} \quad \text{if } r > r_s. \tag{4.1}$$

In this work we arbitrarily set $\phi(r) = 1$ if $r \leq r_s$ with $r_s = 6\,h^{-1}$Mpc. This choice is equivalent to imposing a lower cutoff in the 60 μm luminosity which in turn avoids giving too much weight to faint, nearby *IRAS* galaxies that do not reliably trace the galaxy distribution in the nearby regions (Rowan–Robinson *et al.* 1990). The relevant parameters have been determined via likelihood analysis using only the objects within $100\,h^{-1}$Mpc. The results are displayed in Table 1 for the *PSCz* and 1.2-Jy surveys, both in redshift (z-) and real (R-) space (i.e. after correction for redshift space distortions as discussed in § 3.3). The predicted number density of galaxies as a function of redshift distance, predicted from eqn. 4.1, is shown in Fig. 4.1, superimposed on the observed N vs. r histograms. The theoretical curves provide a good description of the data.

Our estimator for the selection function is independent of clustering but requires a prior knowledge of the evolutionary rate of the galaxy population. Springel & White (1998) have recently developed a new technique to estimate the rate of evolution of the selection function. Their application to the 1.2-Jy catalogue shows rather strong evolution which becomes even more dramatic when applied to the *PSCz* catalogue (Springel & White 1998). Ignoring such an effect would potentially cause spurious streaming motions in the model velocity. However, as we have verified, our selection function for *PSCz* turns out to be very similar to the one obtained by Springel & White (1998) within the scales relevant for our analysis. The difference between the two selection functions increases with the distance but only up to a 5 % level at $200\,h^{-1}$Mpc. Strong evolutionary effects become important only beyond these scales and therefore we will neglect them when modelling the *PSCz* velocity field.

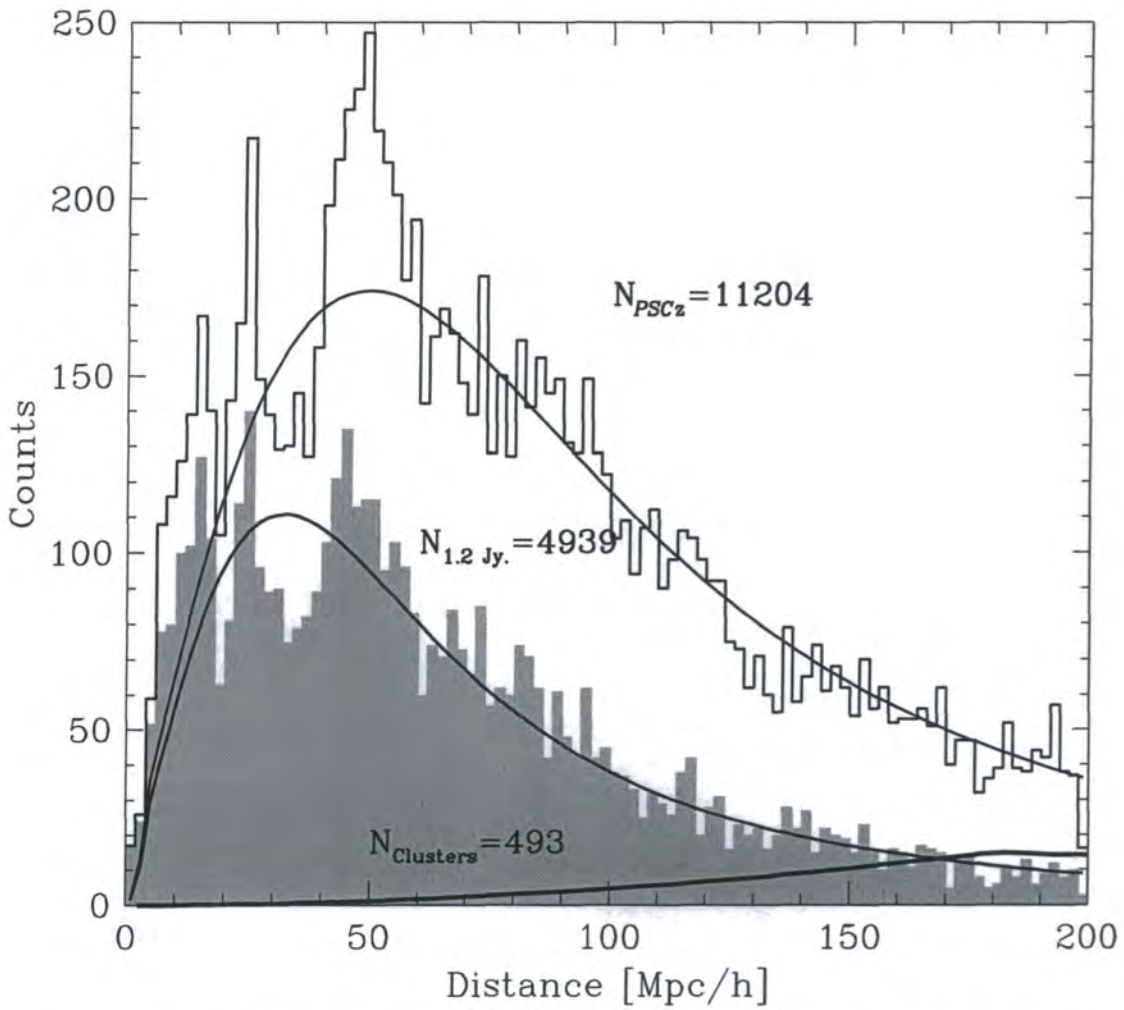

Figure 4.1: Redshift distribution for galaxies. The number of galaxies as a function of redshift distance in the *PSCz* (upper histogram) and 1.2 Jy (lower, shaded histogram) samples. The curves show the expected counts as a function of distance estimated from the selection functions. The heavy line at the bottom shows the predicted distance distribution of Abell/ACO clusters. The labels give the total number of objects in each sample.

Table 4.2: Parameters for the selection function of Abell/ACO clusters

Sample	r_{o1}	r_{o2}	r_{c1}	r_{c2}	A_1	A_2	$\bar{n}$
Abell/ACO	31.8	44.0	180	235	125	289	$4.61 \cdot 10^{-5}$

For the Abell/ACO composite sample we adopt the selection function derived by BP96:

$$\phi(r) = \begin{cases} 1 & \text{if } r \leq r_{c1} \\ 0.5(1 + A_1 \exp(-r/r_{o1})) & \text{if } r_{c1} < r \leq r_{c2} \\ 0.5(A_2 \exp(-r/r_{o2}) + A_1 \exp(-r/r_{o1})) & \text{if } r > r_{c2} \end{cases} \quad (4.2)$$

The estimated values of the parameters are listed in Table 4.2, and the expected number of clusters as a function of redshift distance is shown in Fig. 4.1 as a thick line.

The mean separation, l, of the objects in a population of tracers limits the intrinsic resolution with which they probe the underlying cosmic fields. A natural smoothing length, $r_{sm} = l$, has therefore to be used to reflect the sparse sampling and correct for shot noise errors. In a magnitude limited survey, l increases with distance r according to:

$$l(r) = [\bar{n}\phi(r)]^{-1/3}, \quad (4.3)$$

where the average number density of objects $\bar{n}$ can be estimated from

$$\bar{n} = \frac{1}{V} \sum_{i=1}^{N_g} \phi(r_i)^{-1}, \quad (4.4)$$

and the sum extends to all the N_g objects contained within the sampled volume V. The values of the mean galaxy separation at $100\,h^{-1}$Mpc have been reported in Table 1 both for the *PSCz* and 1.2-Jy samples. Fig. 4.2 shows the mean inter-object separation as a function of r for the three samples considered. Because of the shallower depth of the 1.2-Jy sample, its inter-galaxy separation increases much more steeply with distance than in the *PSCz* sample. Thus, at a fixed resolution, the *PSCz* survey probes cosmic structures at larger distances than the 1.2-Jy survey without an increase the shot noise. The dot-dashed line in Fig. 4.2 shows the Abell/ACO mean intercluster separation. Locally, this is much larger than the corresponding separation for the galaxy surveys, but on scales greater than $170\,h^{-1}$Mpc, clusters start to become more effective than *IRAS* 1.2-Jy galaxies in tracing the cosmic density fields.

4.3 Non–parametric Models of the Cosmic Velocity Field

The main aim of this chapter is to obtain a self–consistent, non–parametric model of the velocity field in the local universe (i.e. for $r < 150\ h^{-1}$Mpc). We do this by removing

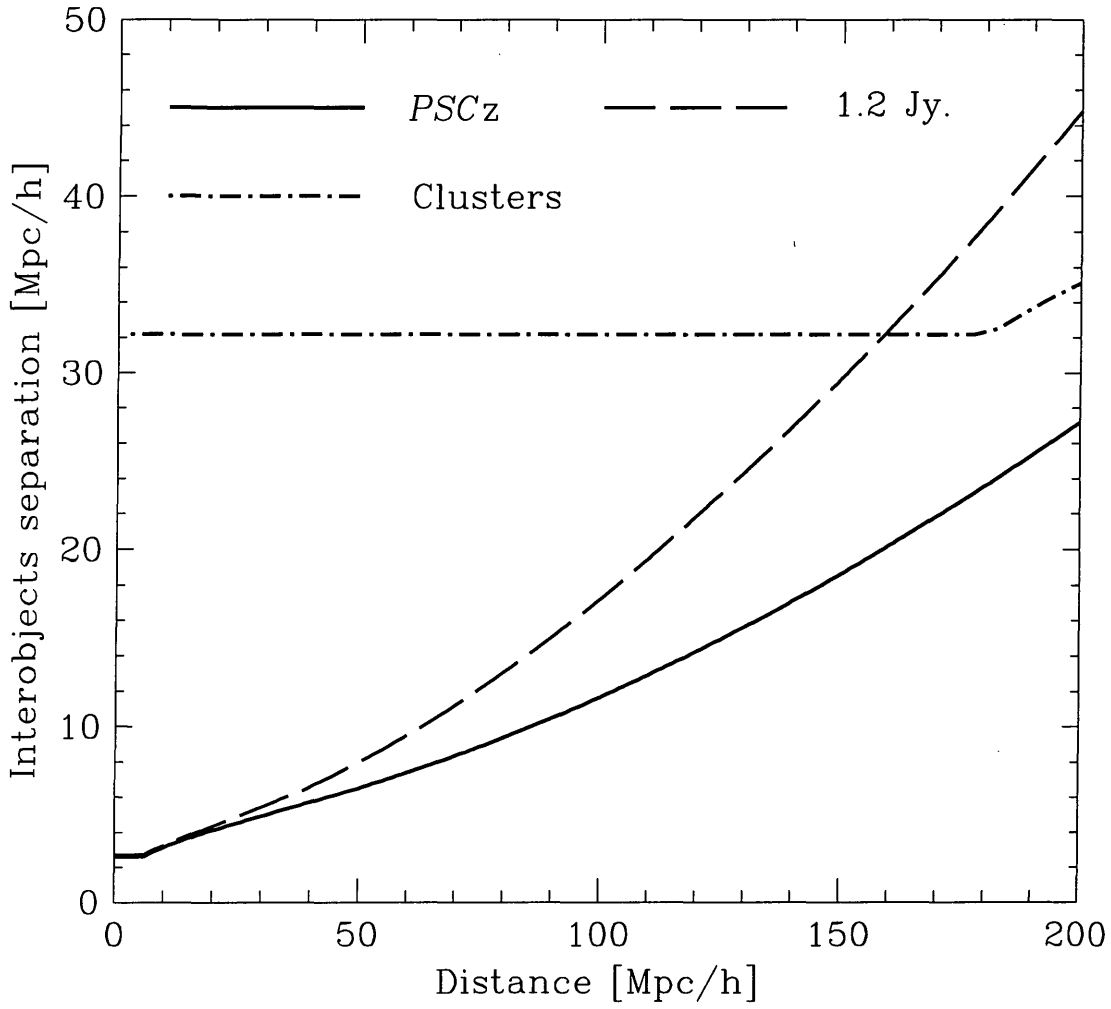

Figure 4.2: Mean separation as a function of radial distance (in h^{-1}Mpc) of objects in the three samples considered in this chapter *PSCz* galaxies (continuous line), 1.2-Jy galaxies (dashed line) and Abell/ACO clusters (dot–dashed line).

the redshift space distortions that affect the radial galaxy distribution in the survey using two different procedures. The first is the iterative technique pioneered by Strauss & Davis (1988), applied by Yahil *et al.* (1991), and further refined by Sigad *et al.* (1998). Most of the results presented here were obtained using this technique. The second procedure, used here primarily to check for possible systematic effects, is the non–iterative technique introduced by Nusser and Davis (1994) (*cf.* § 3.3 for further details of these two methods).

4.3.1 Error estimates using mock catalogues

We have used a suite of large cosmological N-body simulations to generate mock galaxy catalogues that mimic the main properties of the 1.2-Jy redshift surveys. We use these to quantify random and systematic errors in our reconstructed velocity fields. For the fields inferred from cluster catalogues, we adopt the error estimates derived by BP96 and by Branchini *et al.* (1997) on the basis of a hybrid Monte Carlo/mock catalogue technique. The simulations used to generate the mock 1.2-Jy catalogues are LCDM and SCDMG described § 3. In our analysis we use the same *IRAS PSCz* mock catalogues as employed in the previous chapter.

Several constraints were applied to the mock catalogues in order to obtain mass distributions and velocity fields as similar as possible to 1.2-Jy:

- Local Group observers. Hypothetical observers were selected from particles that have a velocity, $\mathbf{v}_{LG} = 625 \pm 25$ km s^{-1}, and lie in regions in which the shear within $5\,h^{-1}$Mpc is smaller than 200 km s^{-1}and the fractional overdensity within the same scale ranges between -0.2 and 1.0 (Brown and Peebles 1987). These constraints mimic the Local Group environment.

- Coherent galaxy dipole. A galactic coordinate system, (l, b), in the (periodic) computational volume was defined such that the velocity of the observer pointed towards $(l, b) = (276, 30)$, the direction of the dipole anisotropy observed in the cosmic microwave background (CMB) radiation. This dipole is known to be approximately aligned with the dipole in the distribution of *IRAS* galaxies (Strauss *et al.* 1992, Schmoldt *et al.* 1998).

- Radial selection. We generated flux–limited "galaxy" samples using a Monte Carlo rejection procedure to select particles in the simulations, assigning them fluxes according to eqn. 4.1. In the vicinity of an observer, the particle number density in the simulation is less than the number density of galaxies in the 1.2-Jy catalogue. We were therefore forced to generate catalogues that are semi–volume limited at a radius of $7.8\,h^{-1}$Mpc for the 1.2-Jy cases.

- Masked areas. To mimic the incomplete sky coverage, we excluded all objects within the unobserved regions in the 1.2-Jy survey.

An illustration of the utility of these mock surveys is provided in Fig. 4.3. The left–hand panel displays density and velocity fields projected onto the mock Supergalactic plane, after smoothing with a Gaussian filter of radius $6\,h^{-1}$Mpc. The right–hand panel shows density and velocity fields reconstructed using Method 1 above. All the main features, as well as most of the small scales structures, are correctly reproduced. Not surprisingly, the main differences occur around SGY= 0, i.e. within the zone-of-avoidance, and close to density peaks. (Very similar results are obtained with Method 2 above.)

A complete error analysis for the Abell/ACO cluster catalogues may be found in Branchini *et al.* (1997).

4.4 A Cosmographic Tour

In this Section we present a qualitative description of the model density and velocity fields of the local universe derived from the *PSCz* survey. We analyse the data using Method 1 above. Visualizing three dimensional structures and the corresponding vector fields, is not easy. Fortunately from this point of view, the most interesting structures in the nearby universe, on scales larger than the Local Supercluster are roughly distributed in a planar structure, de Vaucouleurs' (1948) Supergalactic plane (at supergalactic coordinates SGZ= 0). In this analysis we will mainly follow the somewhat traditional way of displaying the density and velocity features by projecting onto this plane. However the distribution of structures onto planes parallel to the Supergalactic one is discussed as well.

The depth and sampling frequency of the *PSCz* dataset allows a reliable map of the density field to be constructed within a sphere around us of radius $150\,h^{-1}$Mpc. Fig. 4.4 shows the adaptively smoothed overdensity field within this sphere, projected onto the Supergalactic plane. Within $30\,h^{-1}$Mpc a constant Gaussian filter of radius $3\,h^{-1}$Mpc has been used to smooth the field, but beyond that the radius of the filter increases linearly with distance up to $11.25\,h^{-1}$Mpc at $150\,h^{-1}$Mpc. This smoothing maintains a roughly constant sampling error within the volume. The $\delta = 0$ level is indicated by the yellow line. The most striking feature of this map is the large scale coherence of the mass distribution. Interconnected overdensities, separated by very large voids, extend over distances of order of 100 h^{-1}Mpc. The most prominent structure, which plays a major role in the dynamics of the local flow field, is the overdense ridge that extends from the Perseus–Pisces supercluster, close to the centre of the map, all the way to the Shapley concentration near the top left corner.

The *PSCz* survey is large enough to allow the velocity field corresponding to the mass distribution to be reconstructed fairly accurately, with a relative error always smaller than 50 % in the region depicted in Fig. 4.4. This precision, however, is higher than that with which peculiar velocities can be measured at those distances and so we cannot compare our model predictions with velocity data over the entire region of Fig. 4.4. Such a comparison

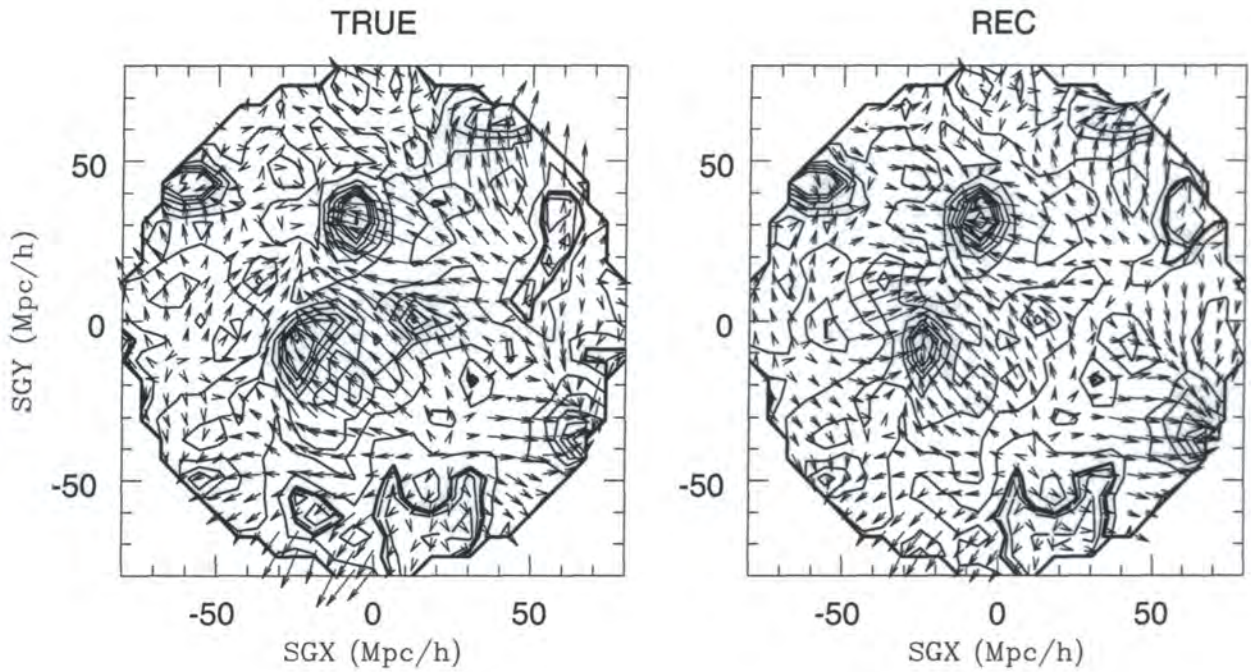

Figure 4.3: Density and velocity fields in a mock *PSCz* catalogue projected onto the mock "Supergalactic" plane. The hypothetical observer is located in a region analogous to the Local Group. Data are shown in a sphere of $120\,h^{-1}$Mpc radius centred on the observer. Both density and velocity fields have been smoothed using a Gaussian filter of radius $6\,h^{-1}$Mpc. The panel a) shows the true fields while the plot b) shows the reconstructed fields using Method 1. Continuous lines represent isodensity contours with a spacing of 0.25 in δ. Solid lines encompass overdensities and dashed lines underdensities. The heavy line indicates the $\delta = 0$ contour level. The amplitude of the velocity vectors is on an arbitrary scale. The panel c) shows the absolute value of the residual between the true an reconstructed density field, $|\delta_{TRUE} - \delta_{REC}|$. Panel d) is the residual velocity field between the true field and the reconstructed field projected onto the "Supergalactic" plane. The shaded regions on panel c) and d) delineate the "Galactic Plane"

can only be carried out reliably over a smaller volume of radius $\sim 80\,h^{-1}$Mpc. For this reason we now describe in some detail our reconstructions within this distance.

4.4.1 The *PSCz* model density and velocity fields within $80\,h^{-1}$Mpc

Fig. 4.5 shows the *PSCz* model density and velocity fields smoothed with a $6\,h^{-1}$Mpc Gaussian and projected onto the Supergalactic plane. Overdensity contours, both positive (continuous lines) and negative (dashed lines), are drawn in steps of $\Delta\delta = 0.5$. The $\delta = 0$ contour is represented by a thick, continuous line. The amplitude of the velocity vectors is on an arbitrary scale.

With a $6\,h^{-1}$Mpc smoothing, the Local Supercluster, centered on the Virgo cluster at $(\mathrm{SGX}, \mathrm{SGY}) = (-2.5, 11.5)$, does not appear as an isolated structure but is connected instead to the prominent Hydra–Centaurus supercluster at $(\mathrm{SGX}, \mathrm{SGY}) = (-35, 20)$. Together with the Pavo–Indus–Telescopium supercluster $[(\mathrm{SGX}, \mathrm{SGY}) = (-40, -15)]$, the latter makes up the well known Great Attractor. The Coma cluster and its neighbour, A1367, appear as a peak at $(\mathrm{SGX}, \mathrm{SGY}) = (0, 75)$, slightly elongated in the SGX direction. The Perseus–Pisces supercluster is clearly visible at $(\mathrm{SGX}, \mathrm{SGY}) = (45, -20)$ and is the second largest peak on the map, well separated from its northern extension $[(\mathrm{SGX}, \mathrm{SGY}) = (45, 20)]$ which is sometimes called the Camelopardalis supercluster. Finally, the Cetus Wall may be seen as an elongated structure around $(\mathrm{SGX}, \mathrm{SGY}) = (15, -50)$. The Sculptor void $[(\mathrm{SGX}, \mathrm{SGY}) = (-20, -45)]$ is the largest underdensity in the map, but is almost matched in size by a void in the background of the Camelopardalis supercluster. Three more underdense regions that exert an important influence on the local dynamics are the voids in the foreground of Coma $[(\mathrm{SGX}, \mathrm{SGY}) = (-10, 50)]$, in the background of the Perseus–Pisces complex $[(\mathrm{SGX}, \mathrm{SGY}) = (50, -50)]$, and behind the Great Attractor $[(\mathrm{SGX}, \mathrm{SGY}) = (-60, 10)]$.

The competing dynamical roles of the various overdense and underdense structures seen in Fig. 4.5. determine the local velocity field in a complex manner that cannot be simply described as a bulk flow or a multi–spherical infall model. The local velocity field implied by the *PSCz* density field is illustrated by the vectors plotted in Fig. 4.5. Its dominant features are the large infall patterns towards the Great Attractor, Perseus–Pisces and Coma. A striking feature is the large-scale coherence of the velocity field, apparent as a long ridge between Cetus and Perseus–Pisces and as a large–scale flow along the Camelopardalis, Virgo, Great Attractor baseline and beyond (see § 4.5). A prediction of the *PSCz* data is the lack of prominent back-infall onto the Great Attractor region. The flow around it appears to be determined by the compressional push of two voids (at $(\mathrm{SGX}, \mathrm{SGY}) = (-10, 50)$ and $(-60, 10)$) and the pull of the Shapley Concentration on much larger scales (see § 4.5). These features are present also when Method 2 is used for the reconstruction (§ 4.4.2), or when the 1.2-Jy survey is used as the input catalogue (§ 4.4.3). As pointed out by Davis, Nusser & Willick (1996), this model velocity field does

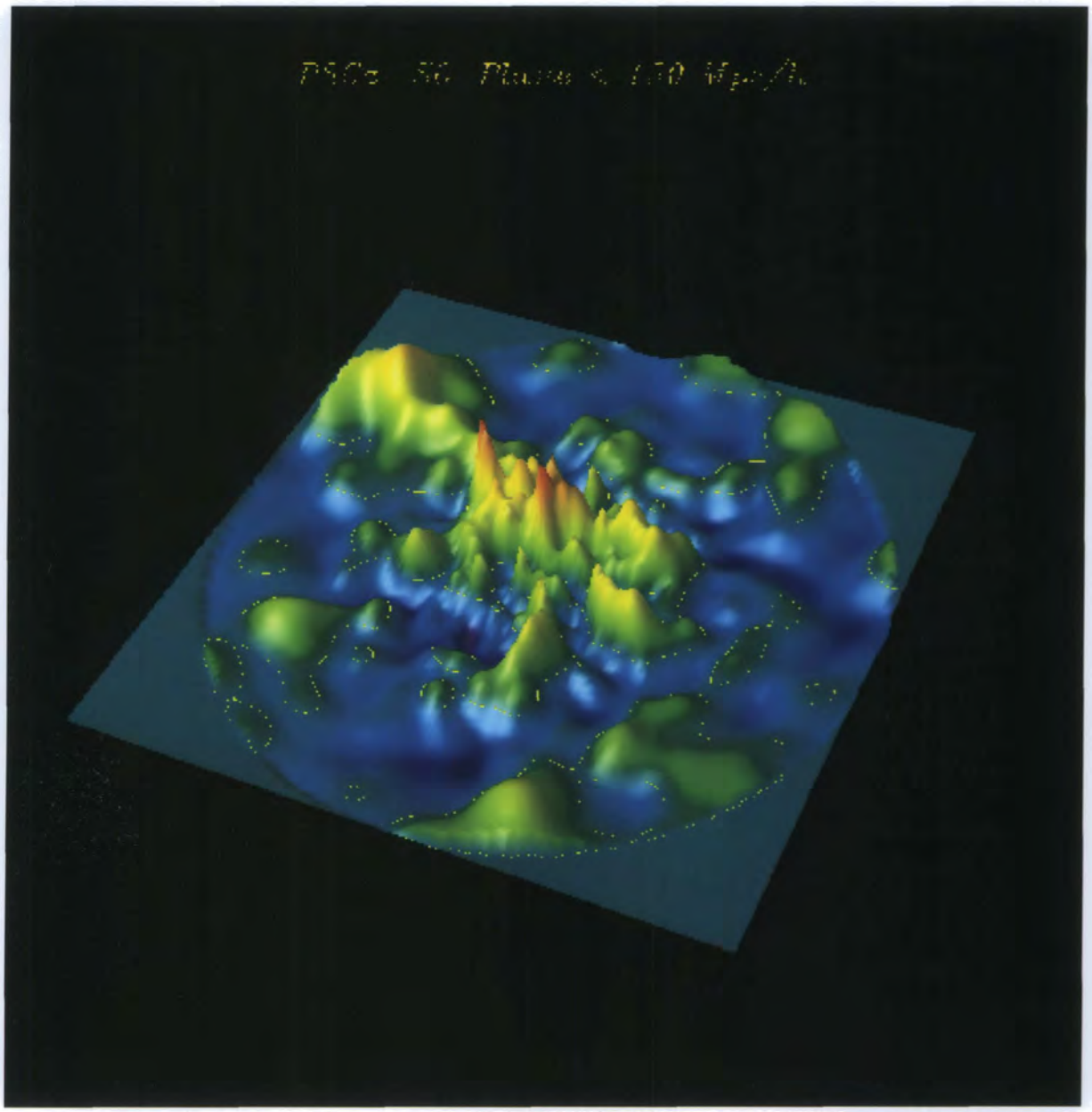

Figure 4.4: Real space density field derived from the PSCz survey. The field has been smoothed with a variable Gaussian filter and projected onto the Supergalactic plane. The smoothing is set at a constant scale of $3h^{-1}$ Mpc within $30h^{-1}$ Mpc and linearly increases with the distance up to a Gaussian of $11.25\,h^{-1}$Mpc at $150\,h^{-1}$Mpc, where the most distant structure are located. The yellow line shows the $\delta = 0$ contour.

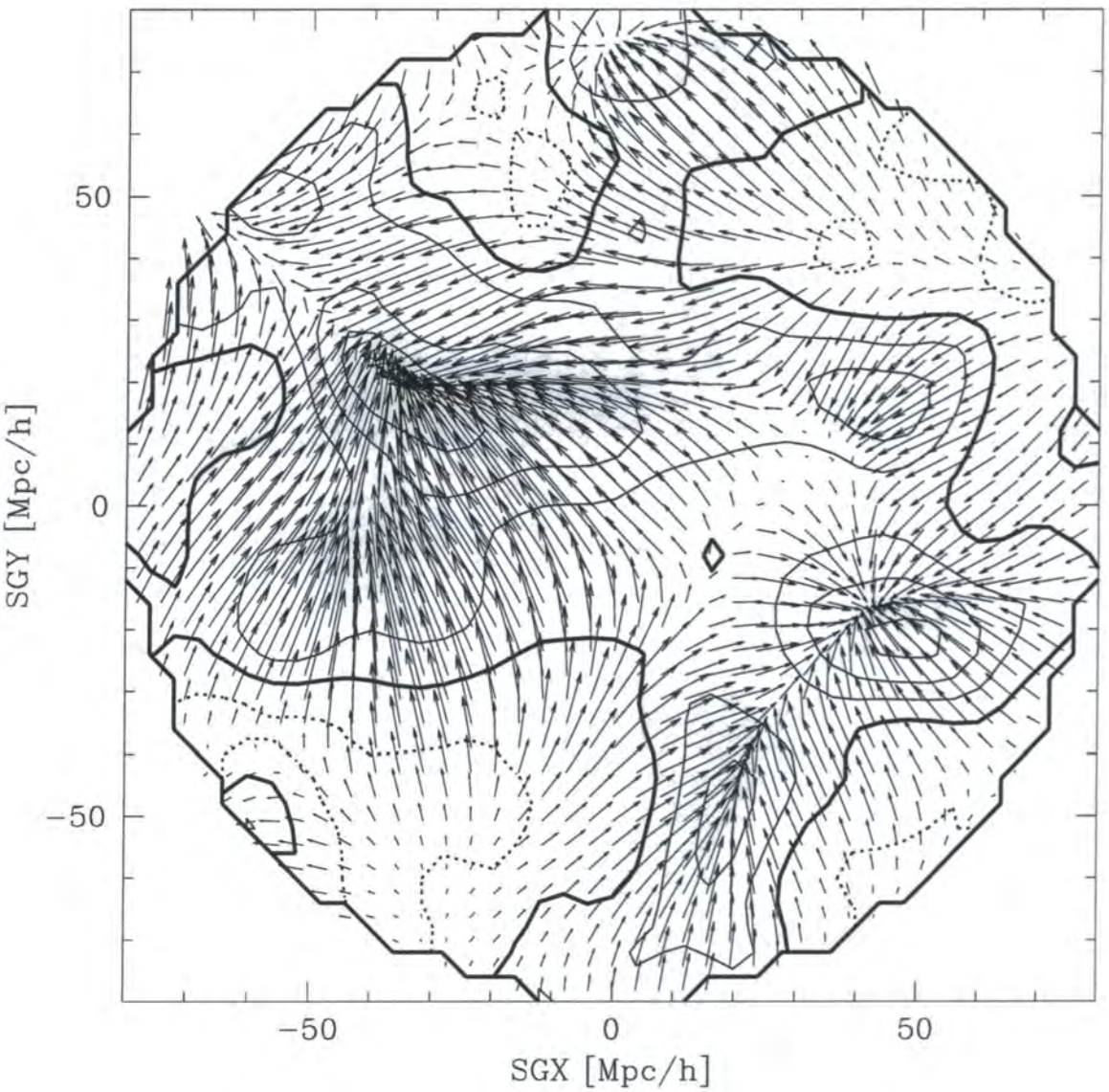

Figure 4.5: Real space density and velocity fields derived from the *PSCz* survey. The fields have been smoothed with a $6\,h^{-1}$Mpc Gaussian and projected onto the Supergalactic plane. The most distant structures are located at $80\,h^{-1}$Mpc. The thick continuous line shows the $\delta = 0$ contour. Positive (continuous lines) and negative (dashed lines) contours are plotted at steps of $\Delta\delta = 0.5$. The amplitude of the velocity vectors is on an arbitrary scale. This reconstruction has been performed using Method 1.

not match the *Mark*III peculiar velocity field (Willick *et al.* 1997a) which exhibits a large outflow away from the Centaurus supercluster and an inflow onto the Hydra complex. Also, there is no evidence for a motion of the Perseus–Pisces supercluster towards us.

Fig. 4.6 extends our qualitative analysis to two planes of constant SGZ, $40\,h^{-1}$Mpc above and below the Supergalactic plane. At SGZ= $+40\,h^{-1}$Mpc the density field (Fig. 4.6b) is dominated by a large void which is connected to the Local Void identified by Tully (1987). The prominent peak at (SGX, SGY) = $(40, -40)$ seems to be an extension of the Perseus–Pisces supercluster. The velocity field (Fig. 4.6a) is still characterized by a coherent, large-scale, flow towards the same direction [(SGX, SGY) = $(-50, 50)$] as the stream seen in the Supergalactic plane. At negative SGZ= $-40\,h^{-1}$Mpc the extensions of the Pavo–Indus–Telescopium $(-50, 15)$ and Perseus–Pisces $(20, -20)$ superclusters are visible. The dynamical effect of these two peaks is evident in the associated large infall patterns (Fig. 4.6c).

4.4.2 Comparison of the two reconstruction methods

A detailed quantitative analysis based on mock *PSCz* catalogues has been performed by Branchini *et al.* (1999) to evaluate random errors. They also showed that the predicted velocity field is not affected by significant systematic bias. To further check this result we have compared the reconstructions produced by the two different methods discussed in § 3.3.2. Figs. 4.7a and 4.7b show the predicted velocity fields smoothed with a $6\,h^{-1}$Mpc Gaussian and projected onto the Supergalactic plane. The two methods succeed in reproducing the main features that we have already highlighted: remarkable large-scale coherence in the velocity field, clear infall patterns onto Coma, Perseus–Pisces and the Great Attractor but no back-infall onto the latter. The only noticeable difference is that Method 2 seems to blur slightly the sharp features (like the Cetus ridge) produced by Method 1 in the velocity field.

Quantitative evidence for the similarity of the two model fields is provided in Fig. 4.7c, which shows a scatterplot of the SGX Cartesian components of the reconstructed velocity fields measured within $80\,h^{-1}$Mpc at gridpoints with SGZ= 0. The peculiar velocities in the two models can be fitted with the linear equation,

$$M_2 = BM_1 + A, \tag{4.5}$$

where M_1 and M_2 denote any of the Cartesian components of the peculiar velocity predicted by Methods 1 and 2, respectively and B is expected to be 1 if no systematic errors are present. The offset A allows for possible differences in the predicted bulk flows in the two models. We obtain the values of A and B by minimizing

$$\chi^2 = \sum_{i=1}^{N_t} \frac{(M_{2,i} - A - BM_{1,i})^2}{(\sigma^2_{M_1,i} + B^2\sigma^2_{M_2,i})}, \tag{4.6}$$

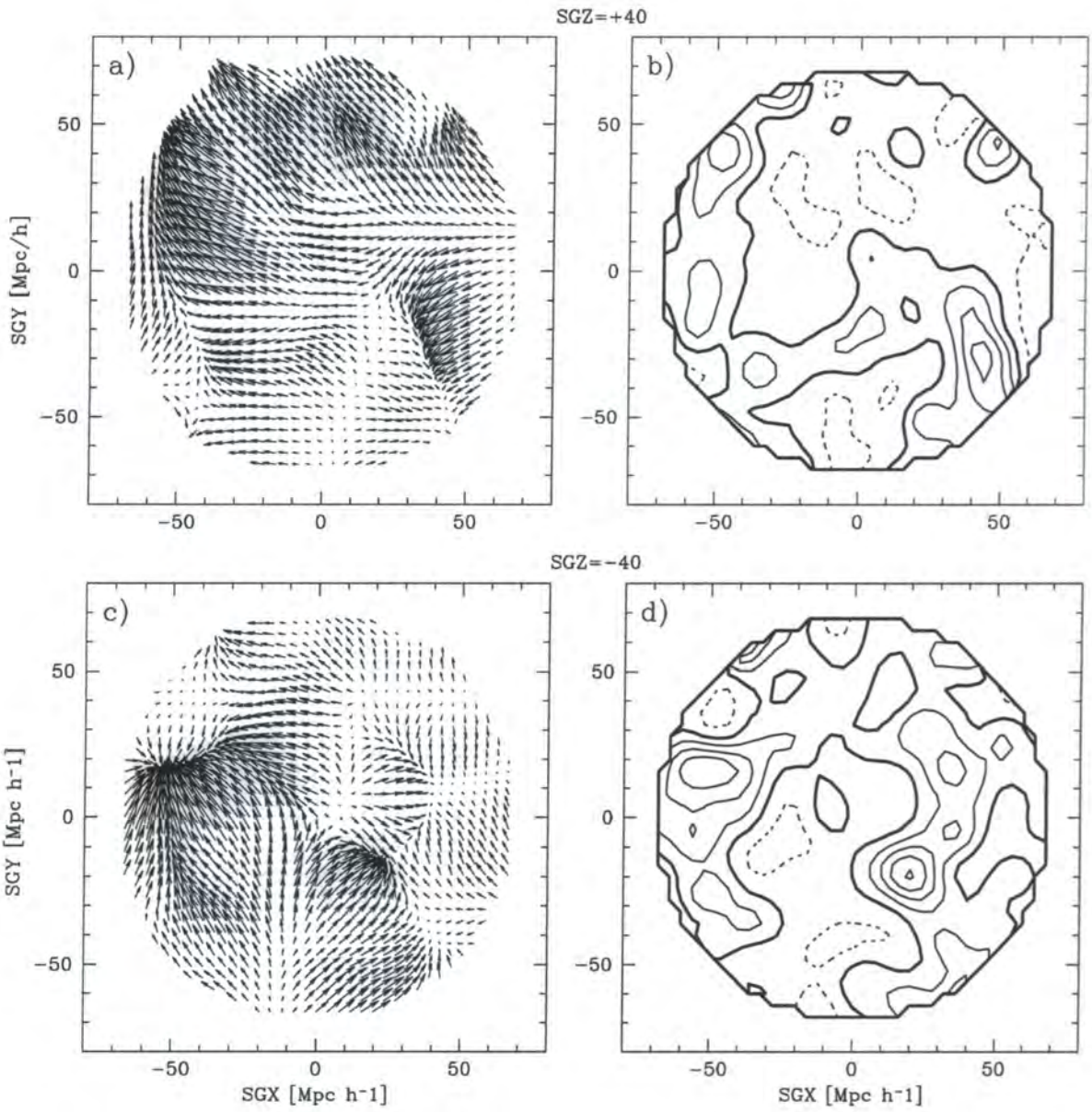

Figure 4.6: Real space density and velocity fields derived from the *PSCz* survey. The fields have been smoothed with a $6\,h^{-1}$Mpc Gaussian and projected onto two slices parallel to the Supergalactic plane. Panels (a) and (b) refer to the slice at SGZ= $+40\,h^{-1}$Mpc, above the Supergalactic plane, while panels (c) and (d) refer to the slice at SGZ= $-40\,h^{-1}$Mpc, below the galactic plane. Density and velocity fields are plotted separately following the same conventions adopted in Fig. 4.5. This reconstruction has been performed using Method 1.

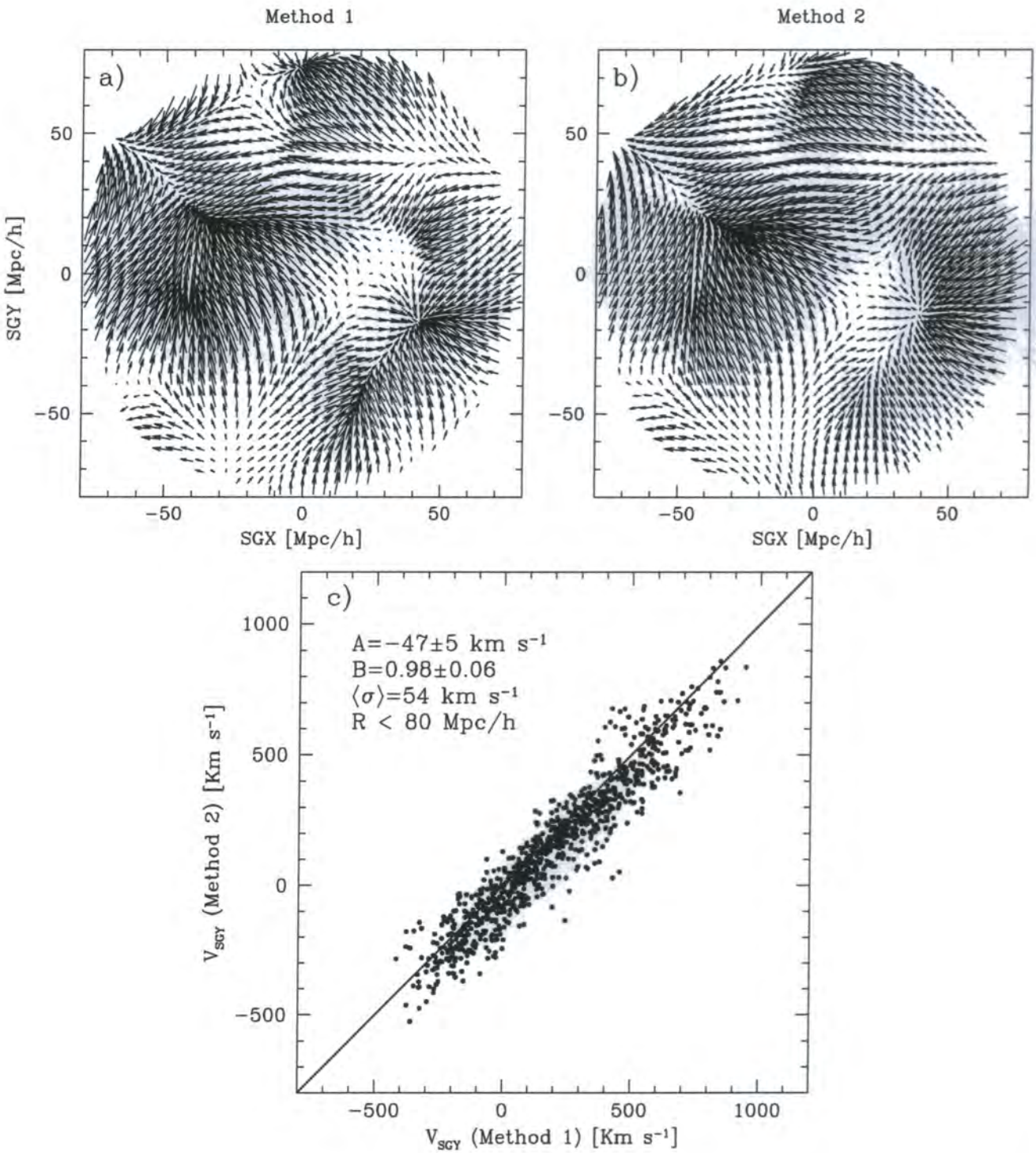

Figure 4.7: The peculiar velocity field reconstructed using Method 1 (top left panel) and Method 2 (top right panel), smoothed with a $6\,h^{-1}$Mpc Gaussian and projected onto the Supergalactic plane. The amplitude of the velocity vectors is on the same arbitrary scale in the two panels. Panel (c) is the scatterplot of the SGX components of the velocity vectors illustrated in the upper panels. Only points within $80\,h^{-1}$Mpc and with SGZ= 0 have been included. The parameters of the linear fit, (A,B), are indicated in the legend along with the scatter in the model velocities, (σ).

where $\sigma_{M_1,i}$ and $\sigma_{M_2,i}$ are the errors in the velocities at a generic gridpoint i in the two methods, and N_t is the total number of points used for the comparison. We assume that $\sigma_{M_1,i} = \sigma_{M_2,i} \equiv \sigma$, so that Eqn. 4.6 becomes

$$\chi^2 = \frac{1}{\sigma^2} \sum_{i=1}^{N_t} \frac{(M_{2,i} - A - BM_{1,i})^2}{(1+B^2)} = \frac{\chi_o^2}{\sigma^2}. \tag{4.7}$$

Only N_i of the N_t points used in the comparison are independent. It can be shown that the quantity $\chi^2_{eff} = (N_i/N_t)\chi^2$ is approximately distributed as χ^2 with $N_{d.o.f} = N_i - 2$ degrees of freedom (e.g. Hudson *et al.* 1995). We can therefore approximately evaluate σ by setting $\chi^2_{eff} = N_{d.o.f}$ so that

$$\sigma^2 = \frac{\chi_o^2 N_i}{N_t(N_i - 2)}. \tag{4.8}$$

We take N_i to be the number of independent volumes within the volume sampled, $N_i \simeq 6\,300$, taking into account the smoothing filter. We then find a regression slope, B= 0.98 ± 0.06, and a negligible zeropoint, A= -47.5 ± 5 km s^{-1}, indicating that there is a systematic difference between the two peculiar velocity fields produced by Methods 1 and 2. This difference is caused by the transformation from the LG frame, where the reconstructions are performed, to the CMB frame, where the comparison is made. The dispersion around the fit for the SGX Cartesian component of the peculiar velocities turns out to be $\sigma_v = 48\beta$ km s^{-1}in both methods. This represents the intrinsic error in the reconstruction procedure and is nearly a factor 2 smaller than the average total error obtained from the error analysis on the mock *PSCz* catalogues (which also accounts for uncertainties in the filling procedures, nonlinearity, finite volume etc.). Similar results are obtained for the SGZ component and even better agreement is found for the SGY component for which the uncertainties in the filling procedure of the zone-of-avoidance are less important.

4.4.3 Comparison of the *PSCz* and 1.2-Jy model velocity fields

Because they were drawn from the same parent catalogue, we expect the *PSCz* and 1.2-Jy catalogues to give consistent model velocity fields, at least in the nearby volume where the sampling by 1.2-Jy galaxies is not too sparse. By analogy with the *PSCz* fields displayed in Fig. 4.5, Fig. 4.8 shows the 1.2-Jy density and velocity fields, smoothed with a $6\,h^{-1}$Mpc Gaussian, and projected onto the Supergalactic plane. Most of the characteristic structures identified in Fig. 4.5 are also visible in Fig. 4.8 except that underdense regions in the 1.2-Jy map appear somewhat more extended than in the *PSCz* map. The overall pattern in the *PSCz* velocity field is reproduced in the 1.2-Jy map although the large-scale coherent flow along the Camelopardalis, Great Attractor baseline is less evident in the 1.2-Jy map. On the other hand, the infall pattern around the Great Attractor in the 1.2-Jy survey spreads out over a larger region. These discrepancies might well be due to the larger shot noise uncertainties in the 1.2-Jy catalogue.

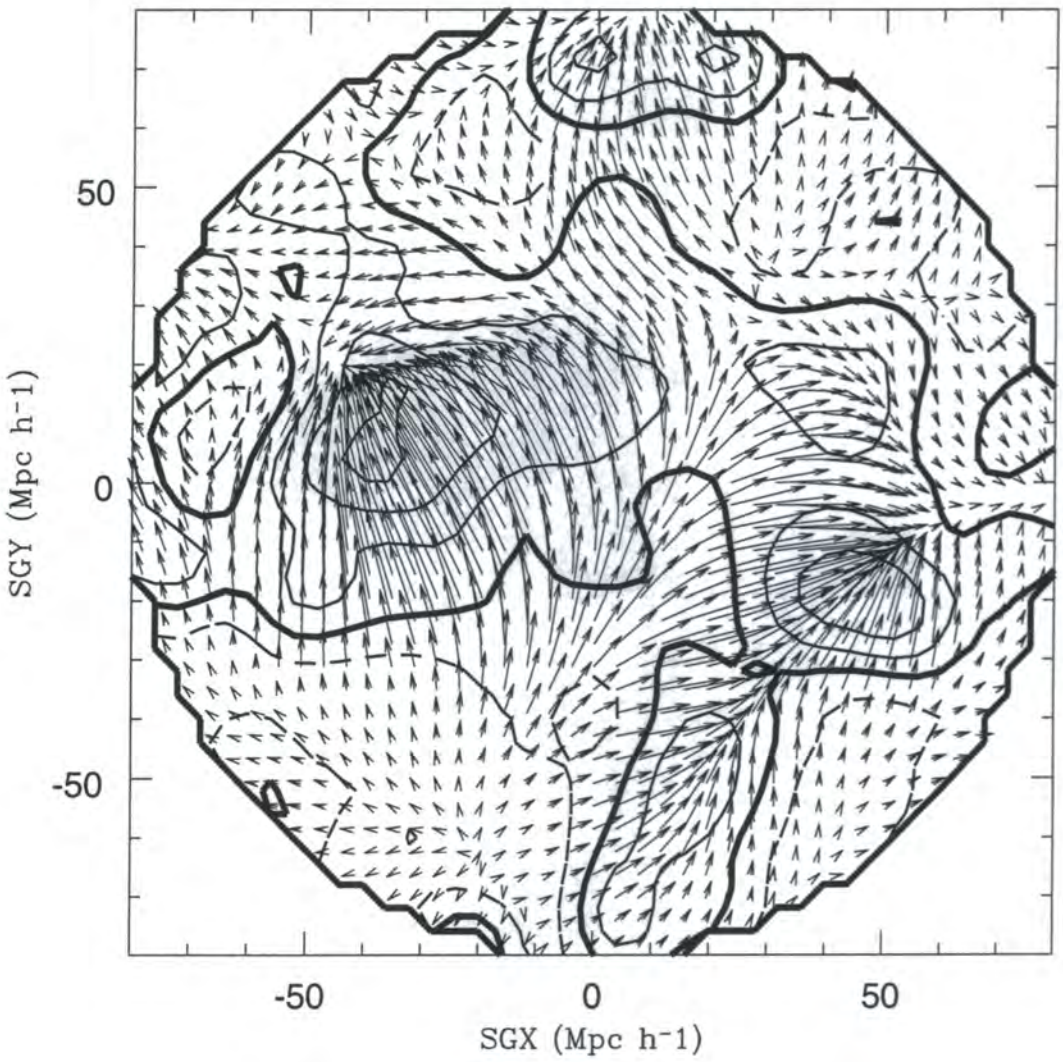

Figure 4.8: Real space density and velocity fields derived from the 1.2-Jy survey. The fields have been smoothed with a $6\,h^{-1}$Mpc Gaussian and projected onto the Supergalactic plane. The overdensity levels and the amplitude of the velocity vectors are as in Fig. 4.5. This reconstruction has been performed using Method 1.

Our 1.2-Jy model velocity field is consistent with that derived independently by Webster, Lahav and Fisher (1997) using the method developed by Fisher *et al.* (1995b). Comparison with their Fig. 4.6d (which assumes a CDM model with $\Gamma = 0.2$ as a prior in the Wiener filtering technique) reveals only one noticeable difference between the two maps. This is in the region of the Great Attractor, where the model of Webster *et al.* predicts a weak back-infall. The discrepancy, however, is small and may simply reflect our use of a constant $6\,h^{-1}$Mpc Gaussian smoothing, which is somewhat larger than the smoothing applied by Webster *et al.* .

Fig. 4.9b shows a comparison between the *PSCz* and 1.2-Jy overdensity fields, both smoothed with $6\,h^{-1}$Mpc Gaussian and tabulated onto 64^3 grids. Only those gridpoints lying along the Supergalactic plane and within $80\,h^{-1}$Mpc of the Local Group position are considered. As in the previous section we fit a straight line to the data and estimate the parameters by minimizing χ^2. The slope of this line is close to unity, indicating that there are no detectable systematic differences between the reconstructions based on the *PSCz* and 1.2-Jy catalogues. The scatter is $\sigma_\delta = 0.16$, and it is likely that most of it is due to shot noise in the 1.2-Jy field. Similar considerations apply to the velocity–velocity comparison in Fig. 4.9a in which, as in Fig. 4.7c, we only show the SGX Cartesian component of the velocity. There is a non–negligible zeropoint offset of 120β km s^{-1}in the SGX components of the cumulative bulk flow in the two models. However, this difference is comparable to the 1–σ uncertainty in the reconstruction of each Cartesian component of the bulk velocity (see § 4.6.1 below). The peculiar features in the velocity–velocity scatterplot reflect correlated velocities within individual cosmic structures. For example, the elongated structure running parallel to the best–fit line corresponds to the infall pattern onto the Perseus–Pisces supercluster which appears to be somewhat more prominent in the 1.2-Jy reconstruction.

4.5 Modelling very large scale motions

The sampling density of the *PSCz* survey is high enough to allow an investigation of the density field out to $\sim 120\,h^{-1}$Mpc even with a $6\,h^{-1}$Mpc Gaussian smoothing. This is illustrated in Fig. 4.10 which displays the usual density and velocity model fields projected onto the Supergalactic plane. The shot noise in this map is still tolerable, at a level comparable to that in the maps discussed in § 4.4.1. The larger volume mapped now reveals the full extent of the coherent streaming involving galaxies from the Camelopardalis Supercluster all the way to the Shapley Concentration (that begins to appear at (SGX, SGY) = $(-100, +60)$), passing through the Local Supercluster and the Great Attractor.

The dynamical sources of the coherent motion seen in Fig. 4.10 are the same ones that we identified earlier as those responsible for the flow pattern behind the Great Attractor. The gravitational pull is mostly due to the Shapley Concentration while the

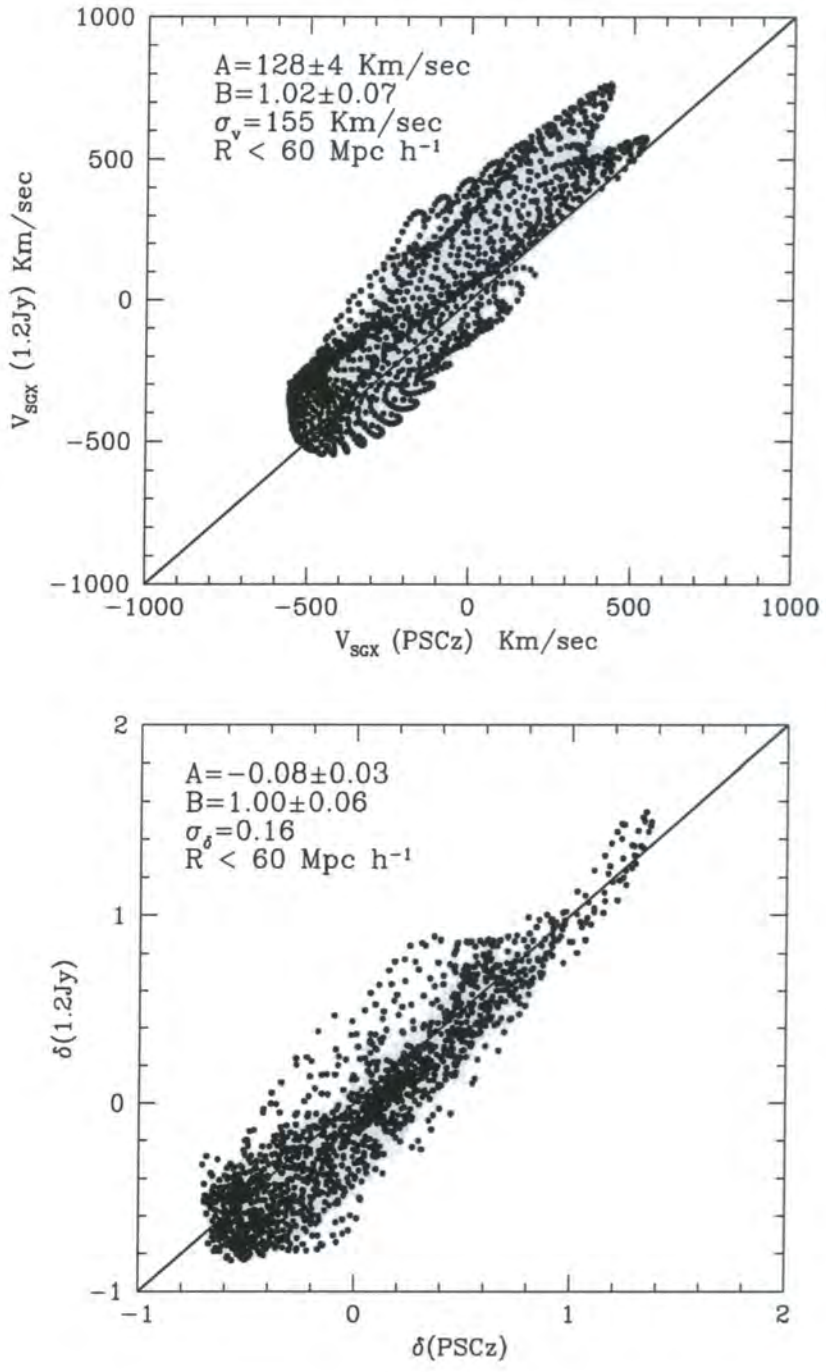

Figure 4.9: Comparison of the 1.2-Jy and *PSCz* density and velocity fields. Densities and velocities are measured at the same grid positions in both cases and only points with SGZ= 0 and distance $\leq 80\,h^{-1}$Mpc are included. The upper panel shows the velocity–velocity comparison using the SGX components of the peculiar velocity, while the lower panel shows the δ–δ comparison. The parameters of the linear regression fit are indicated in both panels.

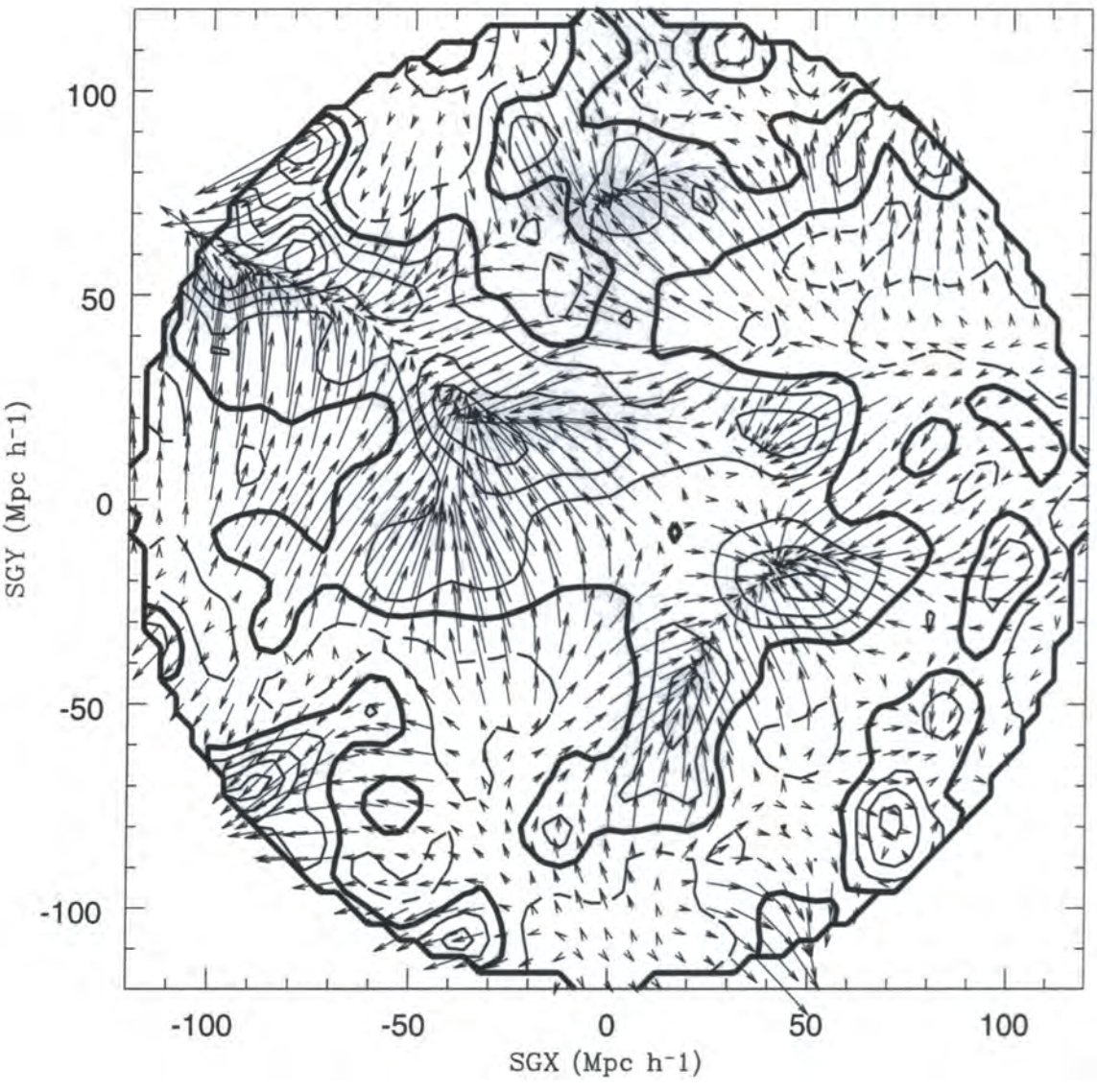

Figure 4.10: Real space density and velocity fields derived from the *PSCz* survey. The fields have been smoothed with a $6\,h^{-1}$Mpc Gaussian and projected onto the Supergalactic plane. This figure is similar to Fig. 4.5, except that it displays data in a larger spherical volume of radius $120\,h^{-1}$Mpc. The thick continuous line shows the $\delta = 0$ contour. Positive (continuous lines) and negative (dashed lines) contours are plotted at steps of $\Delta\delta = 0.5$. The amplitude of the velocity vectors is on an arbitrary scale. This reconstruction has been performed using Method 1.

coherence is aided by the joint push of the two large voids (at (SGX, SGY) = (−80, 10) and (SGX, SGY) = (−50, 70)) that were only partially visible in Fig. 4.5. The map also reveals a large extension to other underdense regions, the Sculptor void and the two connected voids behind the Cetus–Perseus–Pisces–Camelopardalis complex.

In Fig. 4.11 we show the density field projected onto four planes parallel to the Supergalactic one, placed at SGZ= ±40 and SGZ= ±80. Fig. 4.12 shows the related velocity field. The same structures that we have identified in Fig. 4.6 can be now traced over larger scales while keeping the shot noise error at a low level so that we can fully appreciate the large scale coherence of the features both in the density and the velocity field. For example, in Fig. 4.11a the void originally identified in Fig. 4.6b, appears to extend over a much larger region, also along the SGZ axis (Fig. 4.12a and 4.12b). Similarly, the stream towards (SGX,SGY)=(-50,50) that we have identified in the planes at SGZ=0 and SGZ=+40 h^{-1}Mpc it is also present at SGZ=+80 h^{-1}Mpc. No very large scale features are identified on the plane at SGZ=-40 h^{-1}Mpc (Fig.4.11c and 4.12c) which, as we have previously noticed, is dominated by a few infall patterns associated to the southern extensions of Pavo–Indus–Telescopium and Perseus–Pisces superclusters. Coherent structures in the density field and the related streaming motions can be identified on the plane at SGZ=-80 h^{-1}Mpc.

4.5.1 Comparison with the Abell/ACO model fields

Different surveys of *IRAS* and optical galaxies have been used to construct various model velocity fields which have proved to be remarkably consistent (Yahil *et al.* 1991, Kaiser *et al.* 1991, Hudson 1994b, Baker *et al.* 1998). We repeat a similar exercise using a completely different set of mass tracers, the Abell/ACO clusters, to model the density and velocity fields up to very large scales, although with much larger sampling errors. BP96 have already employed the Abell/ACO cluster subsample described § 4.2 to model the density and velocity fields up to scales of 250 h^{-1}Mpc. The reconstruction technique they used is a simplified version of our Method 1 (*cf.* § 3.3.2) in which the selection function (which is nearly constant on the scales of interest) is not iteratively updated and no special treatment is given to triple–valued regions. In order to compare the *PSCz* and cluster model fields we smooth both using a Gaussian of width 20 h^{-1}Mpc. Such a large smoothing is required because of the large intercluster separation.

Fig. 4.13 shows the smoothed density fields projected onto the Supergalactic plane within a distance of 150 h^{-1}Mpc, as derived from the *PSCz* (upper panel) and cluster (lower panel) catalogues. Overdensity contours are plotted in steps of $\Delta\delta = 0.2$, for the galaxy field and $\Delta\delta = 0.88$ for the cluster field. This is equivalent to rescaling the cluster field by a factor $b_c = 4.4$ which is the relative linear biasing parameter inferred in § 4.5.2 below. As before the heavy line traces the $\delta = 0$ contour. The dashed lines show the approximate location of the zone-of-avoidance in the *PSCz* ($|b| \leq 8°$) and cluster

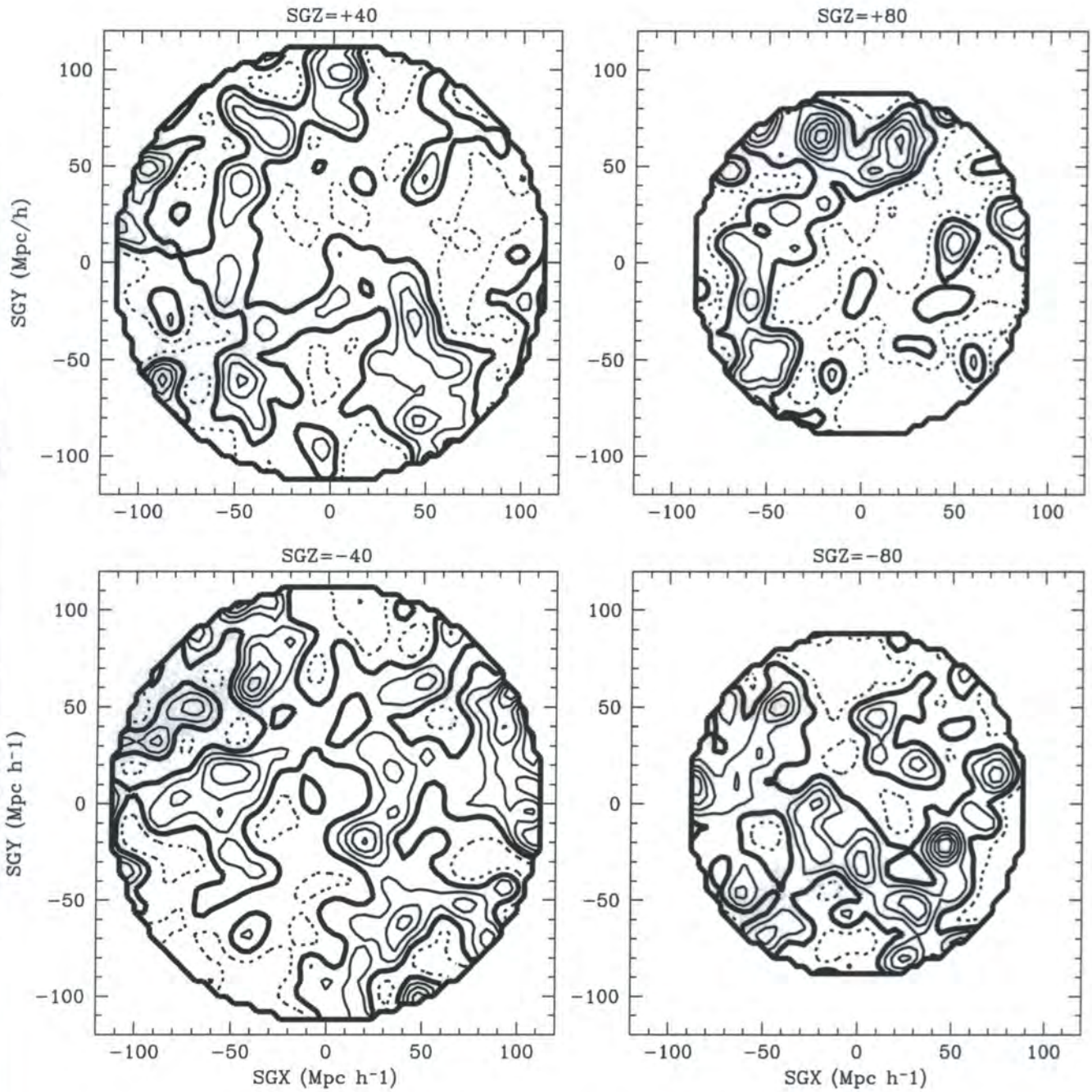

Figure 4.11: Real space *PSCz* density field derived from *PSCz* survey smoothed with a $6\,h^{-1}$Mpc Gaussian and projected onto four slices parallel to the Supergalactic plane. Panels (a), (b), (c) and (d) refers to slices at SGZ=+40, +80, -40 and -80 h^{-1}Mpc, respectively. The same conventions adopted in Fig. 4.6 are adopted.

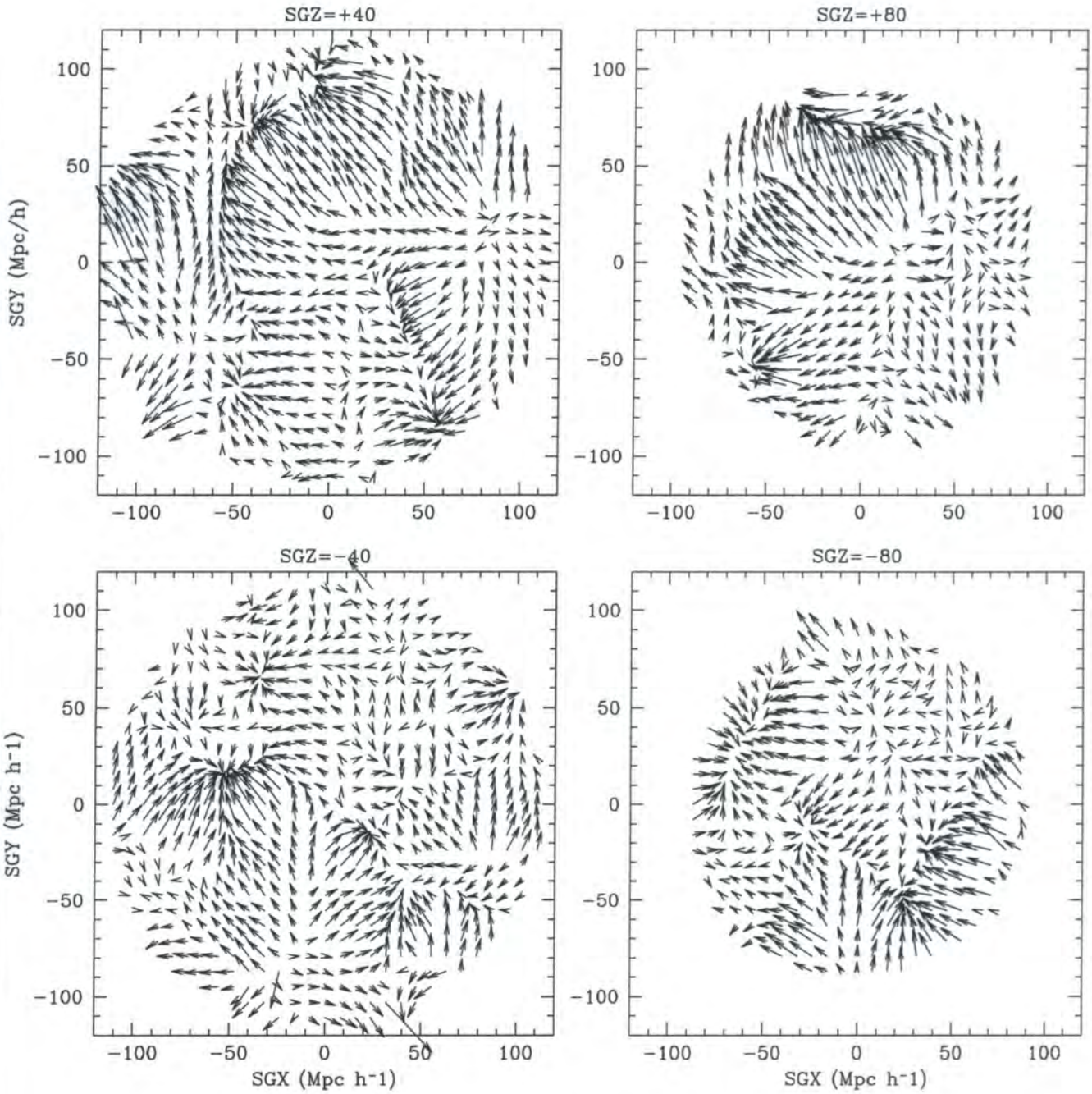

Figure 4.12: *PSCz* velocity field smoothed with a $6\,h^{-1}$Mpc Gaussian and projected onto the four slices displayed in Fig. 4.11

($|b| \leq 20°$) samples.

Despite the $b_c = 4.4$ rescaling, which has been introduced to account for the relative bias between the two populations of objects, the density peaks appear more prominent in the cluster sample than in the *PSCz* map. This may reflect greater undersampling by *IRAS* galaxies of the cores of rich clusters than was indicated by Baker *et al.* (1998), or it may be due to shot noise in the cluster sample which, in spite of the heavy smoothing applied, is still substantial. It should be noted, however, that both the Great Attractor region $(\mathrm{SGX}, \mathrm{SGY}) = (-50, 0)$ and the Perseus–Pisces supercluster $(\mathrm{SGX}, \mathrm{SGY}) = (50, -20)$ where the effect is strongest, both lie within the zone-of-avoidance of the cluster sample. It is therefore possible that the height of these peaks has been artificially amplified by the coupling between shot noise and the filling–in procedure. (For this reason we shall exclude the region at $|b| \leq 20°$ from the quantitative analysis in § 4.5.2 below.) Above $|b| = 20°$ the Shapley Concentration $(\mathrm{SGX}, \mathrm{SGY}) = (-120, 70)$ is the only peak with a larger amplitude in the cluster map than in the *PSCz* map. This comparison could be affected by the fact that beyond $60\,h^{-1}$Mpc we do not perform a cluster–collapsing procedure in Method 1 and so it is possible that the reconstruction method may be placing *PSCz* galaxies at incorrect positions within clusters in the Shapley concentration. Amplitudes aside, the positions of the peaks in the two density maps are very similar. The low density regions are also approximately coincident, although they are less extended in the cluster map in which voids also appear somewhat shallower. The latter effect simply reflects the fact that the assumption of local biasing, $\delta_c = b_c \delta_g$, breaks down at low δ_g because of the constraint $\delta_c \geq -1$.

Fig. 4.14 shows the velocity fields inferred from the two samples, again at a $20\,h^{-1}$Mpc smoothing and projected onto the Supergalactic plane. The amplitude of the velocity vectors is on an arbitrary scale but, in the clusters case, the velocity vectors have been rescaled by $b_c = 4.4$. The two large overdensities lying within the zone-of-avoidance in Fig. 4.14b largely determine the infall patterns at those locations $[(\mathrm{SGX}, \mathrm{SGY}) = (-50, 0)]$ and $[(\mathrm{SGX}, \mathrm{SGY}) = (50, -20)]$. Beyond $|b| = 20°$, however, the galaxy and cluster velocity fields show remarkable similarity. Both exhibit a large coherent flow along the Camelopardalis, Great Attractor, Shapley Concentration baseline. The infall onto the Shapley region is more prominent in the cluster map, but, in general, the velocity field patterns are very similar at positive SGY, with an outflow at positive SGX, and a convergent flow towards the Shapley Concentration at negative SGX. Below the zone-of-avoidance (negative SGY) both maps show outflow from the Sculptor void, but this is less prominent in the clusters case.

4.5.2 The relative linear bias between galaxy cluster and *IRAS* galaxies.

If biasing is a local process (see e.g. Cole *et al.* 1998) then, in the regime where mass fluctuations are small, we expect the level of the bias to be independent of scale. This

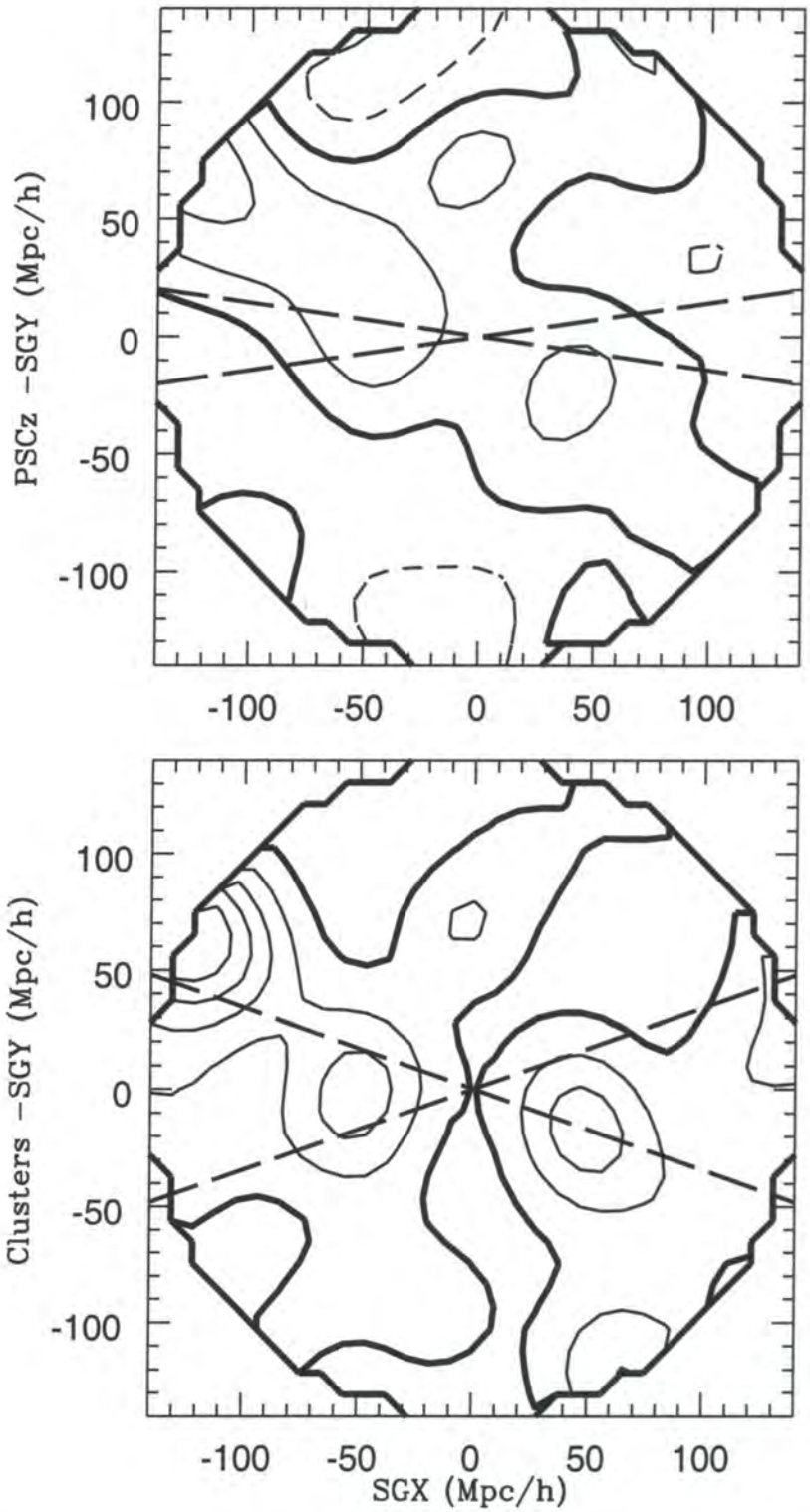

Figure 4.13: Real space density fields derived from the *PSCz* survey (upper panel) and Abell/ACO clusters (lower panel). Both fields have been smoothed with a $20\,h^{-1}$Mpc Gaussian and projected onto the Supergalactic plane within a distance of $140\,h^{-1}$Mpc. The $\delta = 0$ level is indicated by the thick line. Other contours are plotted in steps of $\Delta\delta = 0.2$ for the *PSCz* map and $\Delta\delta = 0.88$ for the clusters map. The dashed lines delineate the zone-of-avoidance in each sample.

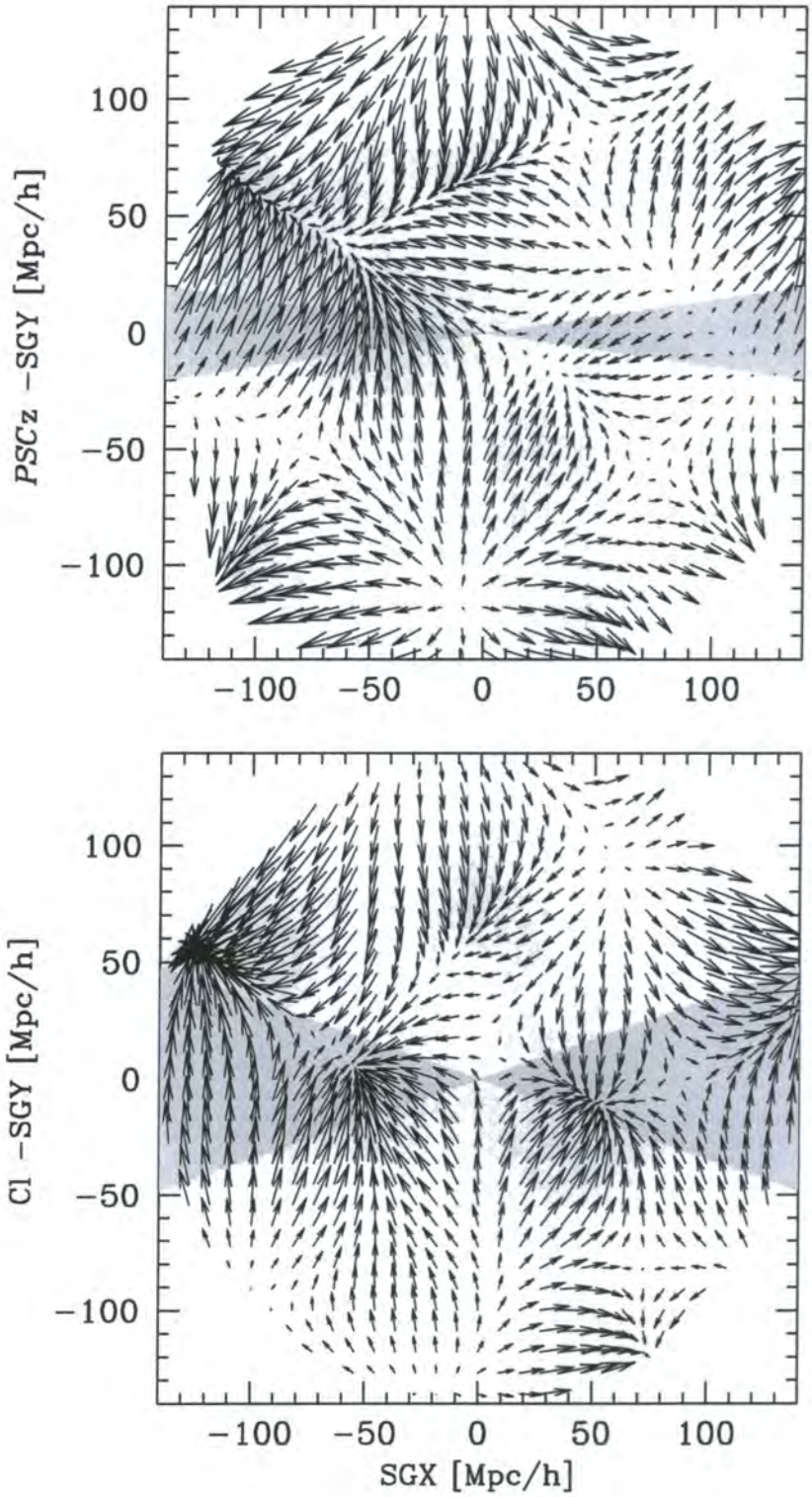

Figure 4.14: Peculiar velocity fields derived from the *PSCz* survey (upper panel) and Abell/ACO clusters (lower panel). Both fields have been smoothed with a $20\,h^{-1}$Mpc Gaussian and projected onto the Supergalactic plane within a distance of $140\,h^{-1}$Mpc. The amplitude of the velocity vectors is on an arbitrary scale, with the clusters' field normalized according to a relative bias parameter, $b_c = 4.4$. The shaded regions illustrate the zone-of-avoidance in each sample.

expectation is consistent with the results of POTENT analyses performed by Dekel *et al.* (1993) and Sigad *et al.* (1998) and we expect it to be valid in the present analysis in which the *PSCz* and cluster density and velocity fields have been smoothed with a $20\,h^{-1}$Mpc filter. Thus, on the scales of interest, we expect the two model density and velocity fields to be linearly related:

$$C = Pb_c + A_c, \tag{4.9}$$

where C and P stand for cluster and *PSCz* and represent either δ or any one of the Cartesian components of the velocity field. The constant b_c is the bias parameter of clusters relative to *IRAS* galaxies and A_c allows for a relative offset in the mean density or bulk velocities of the two fields. For quantitative analyses it is most convenient to use the SGY Cartesian component of the velocity field since this is the least affected by uncertainties in filling in the zone-of-avoidance. To estimate b_c we adopt the strategy of Hudson *et al.* (1995) and Branchini *et al.* (1997), already used in § 4.4.2, of regressing the two model fields by minimising the quantity

$$\chi^2 = \sum_{i=1}^{N_t} \frac{(C_i - A_c - b_c P_i)^2}{(\sigma_{C,i}^2 + b_c^2 \sigma_{P,i}^2)}, \tag{4.10}$$

where the subscript $_i$ refers to any of the N_t gridpoints within the comparison volume. The quantities $\sigma_{C,i}$ and $\sigma_{P,i}$ represent the errors in the cluster and *PSCz* fields, respectively.

The errors in the cluster field, $\sigma_{C,i}$, have been estimated by Branchini *et al.* (1997). They are the sum in quadrature of the intrinsic errors in the reconstruction procedure, as estimated by BP96 using Montecarlo techniques, and the shot noise uncertainties (which dominate the very sparse cluster fields), evaluated using the mock catalogue generated by Kolatt *et al.* (1996) which is designed to reproduce the distribution of structures in our local universe. A typical error in the cluster overdensity field is $\langle \sigma_{C,\delta} \rangle = 0.36$, while for the SGY–component of the velocity field it is $\langle \sigma_{C,v_y} \rangle = 250\beta$ km s^{-1}.

The errors in the *PSCz* fields have been estimated using the mock catalogues described in § 3.2.1. The basic procedure consists of comparing the density and velocity fields obtained by applying Method 1 to the mock galaxy catalogues with the true fields in the parent N–body simulation. We have characterized the reconstruction errors by noticing that the residuals correlate with distance, galactic latitude and, for the velocity field, with the signal itself. From the analysis of the mock catalogues, we have derived two approximate expressions for the errors (valid for $|b| > 20°$):

$$\langle \sigma_{P,\delta} \rangle = 0.11 - 6.7\ 10^{-4} \cdot b + 3.3\ 10^{-4} \cdot r \tag{4.11}$$

and

$$\langle \sigma_{P,v_y} \rangle = 70 + 2.7\ 10^{-1} \cdot r + 0.15 \cdot |v_y|, \tag{4.12}$$

where r is the distance measured in h^{-1}Mpc , b is the galactic latitude in degrees, and $|v_y|$ is the amplitude of the SGY Cartesian component in km s^{-1}. The actual assumed

error at a gridpoint has been generated from a Gaussian distribution centred on $\langle\sigma_P\rangle$ with dispersions of 0.04 for the overdensity and 40 $\mathrm{km\,s^{-1}}$for the v_y field, respectively.

The regression of the *PSCz* and cluster fields uses all the gridpoints within $120\,h^{-1}$Mpc and outside the cluster zone-of-avoidance (i.e. at $|b| > 20°$). As a result of the large smoothing applied not all the gridpoints in the comparison volume are independent. The number of independent points, N_i, can be computed as in Dekel *et al.* (1993),

$$N_i^{-1} = N_t^{-2} \sum_{j=1}^{N_t} \sum_{i=1}^{N_t} \exp(-r_{ij}^2/2r_{sm}^2), \tag{4.13}$$

where r_{ij} is the separation between gridpoints i and j and r_{sm} is the smoothing radius of the Gaussian filter. As in § 4.4.2 we define the $\chi^2_{eff} \equiv (N_i/N_t)\chi^2$ statistics which correspond, in practice, to multiplying the errors σ_P and σ_C by $\sqrt{N_t/N_i}$ in equation (4.10). We use this statistic to assess the errors on b_c and A_c.

Fig. 4.15a shows a δ–δ scatterplot of the model cluster and *PSCz* overdensity fields measured at $\sim$ 1000 randomly selected gridpoints. All 6426 original points are used in the regression analysis. The solid line shows the best fit obtained by minimizing χ^2_{eff} and the parameters of the fit are listed in Table 3. The resulting bias parameter is $b_c^\delta = 4.4 \pm 0.6$. This is compatible with results from independent analyses (e.g. Peacock and Dodds 1994). The parameter $S^\delta = \chi^2_{eff}/N_{dof}$ is close to 1, which may be taken as an indication that the errors have not been grossly over- or underestimated. The systematic difference in the amplitude of the density peaks in the cluster and *IRAS* δ fields, noticed in Fig. 4.13a, manifests itself as a deviation from the best fitting line at large δ_{PSCz}. Restricting the regression to values of $\delta_{PSCz} \leq 0.35$ has a small impact on the final result, returning $b_c^\delta = 4.5 \pm 0.6$, almost identical to the previous value, and $S^\delta = \chi^2_{eff}/N_{dof} = 1.15$. This suggests that the exact weighting of *PSCz* galaxies in high density regions has only a minor effect on the regression analysis, mainly because the overdensity mismatch in large density peaks is restricted to a very few gridpoints. As a further check, we have repeated the δ–δ regression using a *PSCz* velocity model derived without applying our standard procedures for collapsing clusters and handling triple valued regions (which should exacerbate any discrepancies associated with high peaks.) The results, listed in the second row of Table 3, show that the effect on b_c is indeed very small, leading to $b_c^\delta = 4.5 \pm 0.6$.

Fig. 4.15b displays the scatterplot of the SGY Cartesian component of the two velocity fields in which, as in Fig. 4.15a we only show $\sim$ 1000 randomly selected gridpoints to avoid overcrowding. As shown in Table 3 the slope of the best fitting line is $b_c^{v_y} = 4.7 \pm 0.6$ and no significant zeropoint offset is detected, indicating that the SGY components of the cluster and *PSCz* bulk flows are consistent with one another over the scales of interest. However, as indicated in Table 3, the resulting χ^2_{eff} is large, resulting in a $S^{v_y} = 1.55$. This could be the result of underestimating the errors. Indeed, the error analysis by Branchini *et al.* (1997) uses clusters from the Kolatt *et al.* (1996) mock catalogues that do not accurately match the Abell/ACO cluster distribution and velocities. We can obtain $S^{v_y} \simeq 1.0$ if we allow a very reasonable error underestimate in the cluster field of $\sim$ 30%,

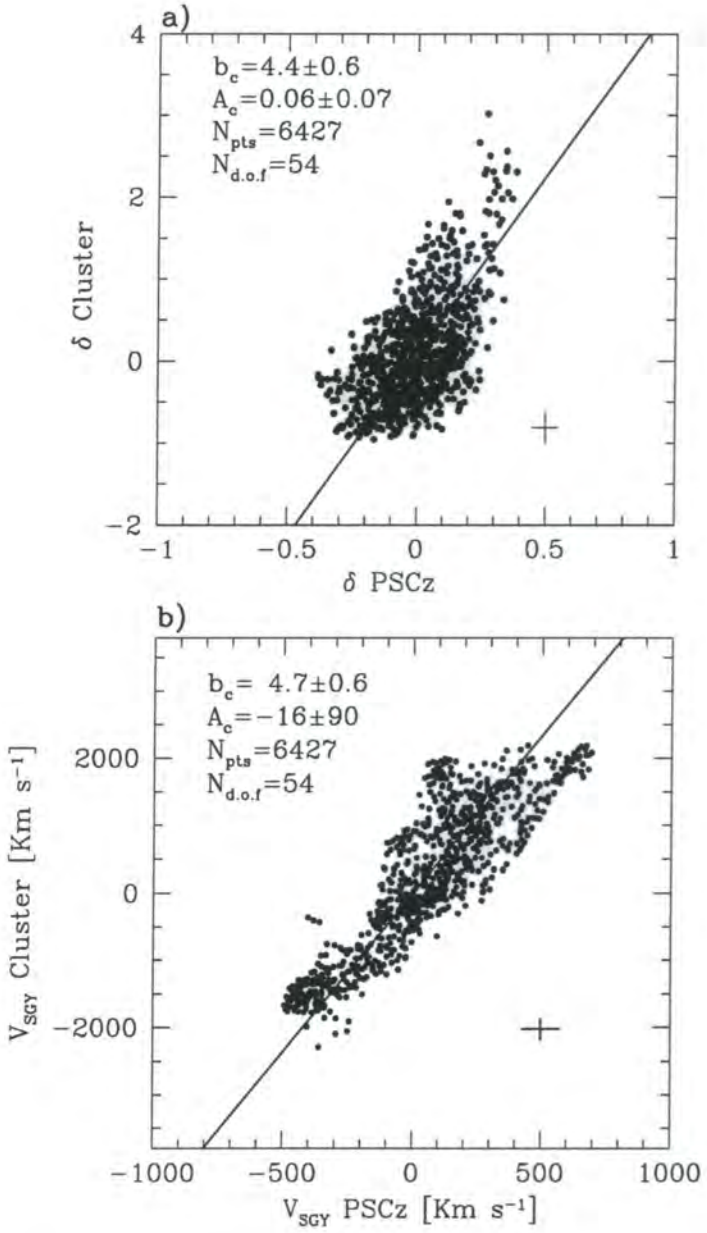

Figure 4.15: Density and velocity scatterplots for the reconstructions based on the *PSCz* survey and a sample of Abell/ACO clusters. For clarity only $\sim$ 1000 out of 1878 gridpoints within a sphere of radius 120 h^{-1}Mpc, having $|b| \geq 20°$, are plotted. The upper panel shows the δ–δ comparison. The velocity–velocity comparison in the lower panel refers to the SGY–component of the velocity. The parameters in the legend refer to the χ^2 fits discussed in the text (see also Table 4.3). The errorbars give the mean 1–σ errors in the two model fields.

Table 4.3: The cluster/*IRAS* galaxy relative bias parameter, b_c. The top and bottom rows give results with and without applying the cluster collapsing procedure. Column 1: N_t^δ, the number of gridpoints used for the regression; column 2: $N_{d.o.f.}$, the number of independent volumes for the regression; column 3: b_c^δ from the δ-δ regression and it 1-σ error; column 4: A_δ, the zero point offset in the δ-δ regression and its 1-σ error; column 5: $S^\delta = \chi^2_{eff.}/N_{dof}$ from the δ-δ regression; column 6: b_c^δ from the v_y-v_y regression and its 1-σ error; column 7: A_{v_y}, the zero point offset in the v_y-v_y regression and its 1-σ error; column 8: $S^{v_y} = \chi^2_{eff.}/N_{dof}$ from the v_y-v_y regression.

N_t	$N_{d.o.f.}$	b_c^δ	A_δ	S^δ	$b_c^{v_y}$	A_{v_y}	S^{v_y}
6427	54	4.4 ± 0.6	0.06 ± 0.07	1.14	4.7 ± 0.6	-16 ± 90	1.55
6527	55	4.5 ± 0.6	0.12 ± 0.07	1.15	4.6 ± 0.6	8.2 ± 91	1.57

in which case we would obtain $b_c^{v_y} = 4.0 \pm 0.6$. Note that a 1σ agreement between b_c^δ and $b_c^{v_y}$ is obtained whether or not the cluster errors have been effectively underestimated. It is worth emphasizing that the agreement of the δ–δ and v_y–v_y comparisons is not trivial. The δ-δ comparison is local; it is hardly affected by problems related to filling in masked regions but is potentially prone to the cluster core weighting problem. The v_y-v_y comparison, on the other hand, involves the distribution of objects within the entire sample and thus is much more strongly affected by the unknown mass distribution within the zone-of-avoidance and beyond the sample's edge. We might therefore expect the two comparisons to be affected by different biases. The agreement in the estimate of b_c from the two analyses suggests that systematic biases have been properly taken into account and that the linear biasing assumption is a good approximation, at least on scales larger than our $20\,h^{-1}$Mpc smoothing.

4.6 The bulk velocity vector

4.6.1 The model bulk flow

The basis for our treatment of random and systematic errors in the bulk velocity vector are, again, the mock *PSCz* catalogues described in § 4.3.1. From each mock catalogue we generate a model velocity field using Methods 1 and 2 of § 4.3.1.The field is then smoothed onto a 64^3 cubic grid of side $192\,h^{-1}$Mpc using a $12\,h^{-1}$Mpc Gaussian filter. Such a large smoothing is chosen in order to obtain an error estimate appropriate to the homogeneous, quantitative comparisons with the Mark III and SFI bulk velocity data that

we will perform in § 4.6.2. We measure the cumulative bulk velocity vector in the CMB frame by averaging over the peculiar velocities measured at gridpoints:

$$\mathbf{V}_B(R) = \sum_{(i,j,k)<R} v_{i,j,k} \Big/ \sum_{(i,j,k)<R} , \tag{4.14}$$

where $v_{i,j,k}$ is the predicted velocity vector in the CMB frame at gridpoint (i,j,k). The sum $\sum_{(i,j,k)<R}$ extends over all the gridpoints contained within a sphere of radius R. The same exercise is then repeated using the original N–body velocity field. This gives an unbiased estimate of the true bulk velocity in the mock catalogue and the comparison between the true and reconstructed bulk velocities provides an estimate of the error in the reconstruction.

The filled circles in Fig. 4.16a show the mean difference between the amplitude of the cumulative bulk flow reconstructed using Method 1 and the true bulk flow, averaged over the different mock catalogues and measured at different radii. The mean value indicates the systematic error in the reconstruction while the errorbars, which give the variance around the mean, measure the random uncertainty. Very similar results are obtained if the reconstruction is carried out using Method 2. Note that the random errors decrease with distance (from ~ 80 km s^{-1}at $10\,h^{-1}$Mpc to ~ 50 km s^{-1}at $100\,h^{-1}$Mpc), while the systematic errors increase with distance and become comparable to the random noise at large radii. Systematic errors come mainly from two sources: the filling–in procedure for the zone-of-avoidance and the modelling of the Local Group velocity. Since our two reconstruction methods work in the Local Group frame, the predicted Local Group velocity vector, obtained from the dipole of the galaxy distribution, must be added to the model velocities. As a result, errors in the determination of the dipole (arising, for example, from shot noise, finite volume and the rocket effect) affect the model bulk velocity vector. The uncertainties due to the filling–in procedure may be minimized by restricting attention to the SGY component of the bulk velocity. As shown by the open symbols in Fig. 4.16a the improvement is quite dramatic, reducing the systematic error to < 20 km s^{-1}.

The errors displayed in Fig. 4.16a cannot readily be used to make quantitative corrections to the *PSCz* model bulk flow since their amplitude depends on β, the only free parameter in the model velocities. However, we can take advantage of the fact that, to first approximation, the model velocities scale linearly with β. Thus, the ratio between the reconstructed and true bulk velocities should be independent of β. This ratio, averaged over our mock catalogues, is shown by filled circles in Fig. 4.16b, as a function of distance, with errorbars representing the relative variance. Since it is independent of β, this ratio may be used as a multiplicative factor to correct the predicted *PSCz* bulk flow amplitudes for systematic errors. As expected, the corrections become very small when considering the SGY component (open circles). We have performed a similar analysis to estimate errors in the *PSCz* bulk velocity obtained using Method 2 and in the 1.2-Jy bulk flow model, obtained using Method 1.

We are now ready to estimate *PSCz* and 1.2-Jy model bulk flows and their uncertain-

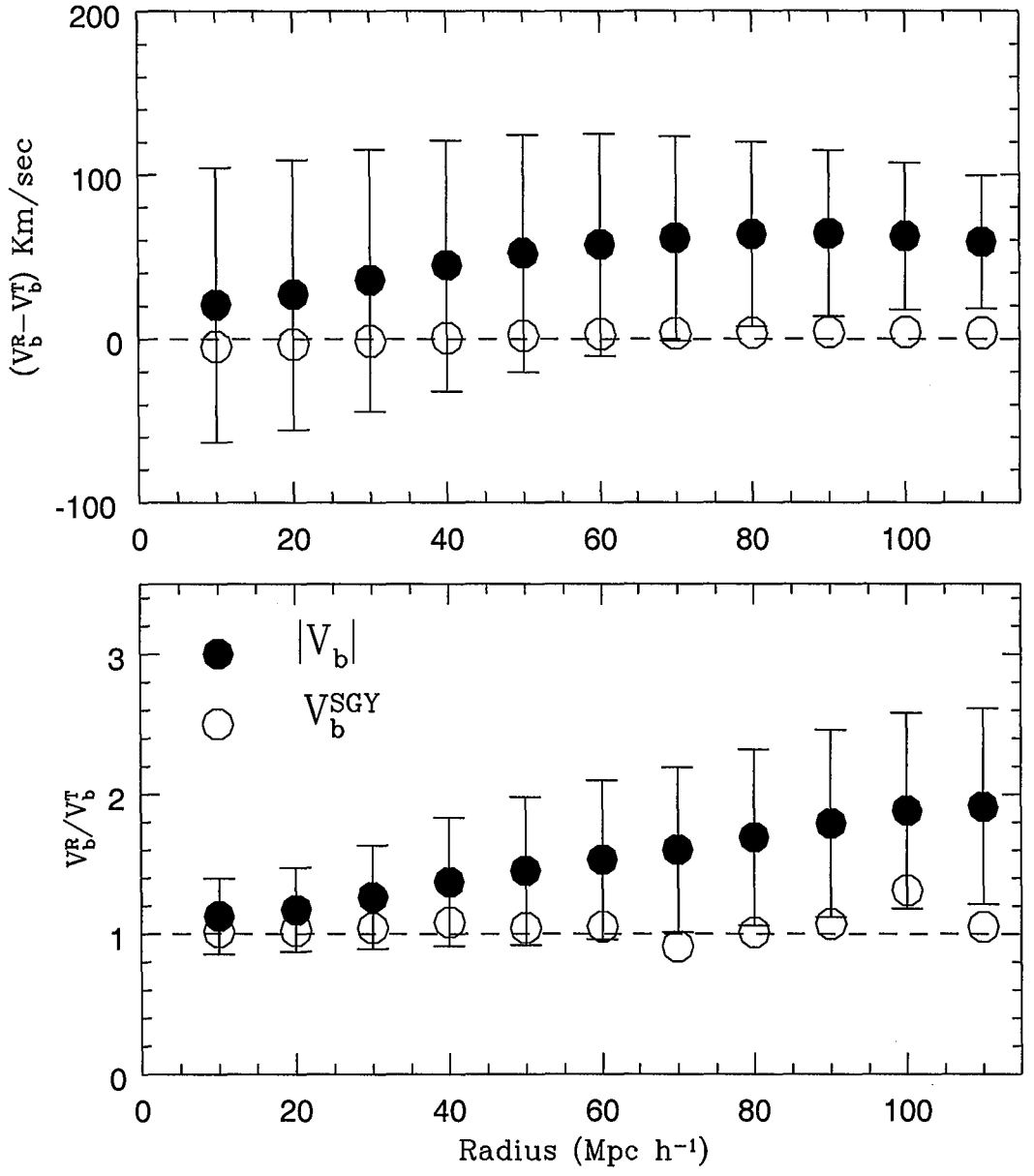

Figure 4.16: Random and systematic errors in the model bulk flow derived from analysis of the mock *PSCz* catalogues. The upper panel shows the difference between the true amplitude of the cumulative bulk flow at different radii and the values reconstructed using Method 1. The lower panel shows the ratio of these two amplitudes. In both panels the circles give mean values and the errorbars standard deviations around the mean. Filled circles refer to the total bulk velocity and open circles to its SGY–component only.

ties. Fig. 4.17a shows the amplitude of the cumulative bulk velocity vector, predicted using various methods and redshift surveys. The velocities are normalized to $\beta = 1$. Open and filled circles show *PSCz* results using Methods 1 and 2 respectively, and filled squares show results from the 1.2-Jy survey, all corrected for systematic errors as discussed in the preceding paragraph. For clarity only the 1–σ error bars from Method 1 are plotted. The filled triangles show the bulk velocity computed from the Abell/ACO model velocity field, rescaled by $b_c = 4.4$ (see § 4.5.2). There is remarkably good agreement between the cumulative bulk flows computed from the different sets of mass tracers, with typical deviations of less than $\sim 20\%$ from the mean in the amplitude from the different surveys and analysis methods. The directions of the cumulative bulk flow vectors, measured within $60\,h^{-1}$Mpc, are plotted in Fig. 4.17b. The *PSCz* model bulk flow aligns within 1σ, with the direction of both the 1.2-Jy and Abell/ACO model bulk flows. The direction of the CMB dipole, indicated by the asterisk, is plotted for reference at the centre of the figure.

So far we have modelled bulk velocities in the nearby universe by considering only the effect of the mass distribution within $200\,h^{-1}$Mpc, as traced by *IRAS* galaxies or Abell/ACO clusters. Bulk flows, however, are sensitive to the mass distribution on scales larger than those probed by our samples. We can correct for this missing large-scale contribution in a statistical fashion, assuming linear theory and using eqn. (3.16). The correction factor is the ratio

$$F(P(k), k_{min}) = \frac{\int_0^\infty P(k)W(kR)^2 dk}{\int_{k_{min}}^\infty P(k)W(kR)^2 dk}. \qquad (4.15)$$

The numerator in this equation is the mean true bulk flow, while the denominator is the mean bulk flow generated only by density fluctuations on scales smaller than $r_{max} = 2\,\pi/k_{min}$. In our case, $r_{max} \sim 200\,h^{-1}$Mpc. Note that the ratio depends only on the spectral shape and on k_{min}, while the dependency on β has cancelled out. Since the bulk flow obeys a Maxwellian distribution, we can estimate the uncertainty in this correction and add it in quadrature to the error in our estimate of the bulk flow calculated from the mock catalogues. In computing F we assume a CDM model with spectral shape $\Gamma = 0.25$, as suggested by a wide variety of data on the large-scale galaxy distribution (e.g. Baugh 1996)

We have applied the correction of eqn. 4.15 to the *PSCz* bulk velocity reconstructed using Method 1. The resulting cumulative bulk velocity (for $\beta = 1$) is shown in Fig. 4.17a as a dot–dashed line labelled M1L. We regard this as our best estimate of the β–dependent bulk flow.

4.6.2 Model vs. observed bulk flow

In this Section, we compare our best estimate of the predicted bulk flow velocity from the *PSCz* survey with recent observational estimates. Such a comparison serves two pur-

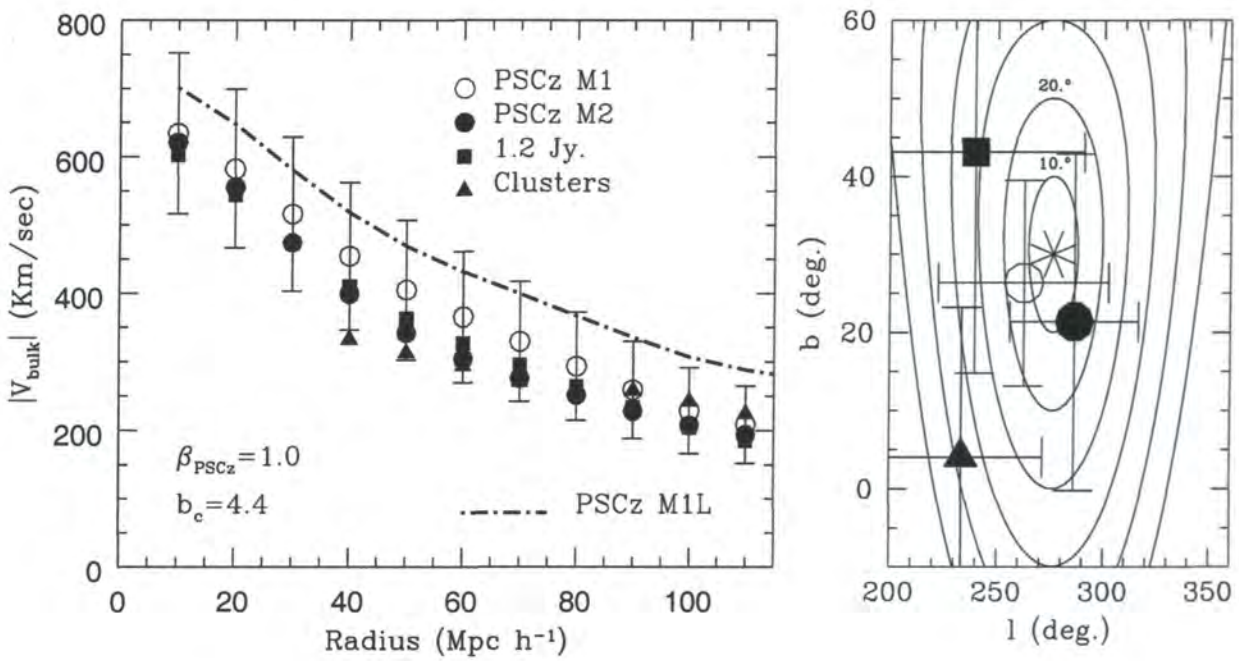

Figure 4.17: The amplitude (left) and direction (right) of the cumulative bulk velocity vector predicted in different models. The circles give results from the *PSCz* survey using Method 1 (open circles) and Method 2 (filled circles); the filled squares give results from the 1.2-Jy survey; the triangles give results from the Abell/ACO cluster sample. For the models based on *IRAS* galaxies, the amplitudes have been normalized to $\beta = 1$, while for the cluster model the velocities have been normalized assuming a relative bias, $b_c = 4.4$. The errorbars give $1\text{–}\sigma$ uncertainties obtained from the *PSCz* survey using Method 1. The dot–dashed line shows the *PSCz* reconstruction using Method 1, but including the contribution to the velocity from density fluctuations on scales larger than $200\,h^{-1}$Mpc. The right-hand panel gives the direction of the predicted cumulative bulk flow at $60\,h^{-1}$Mpc in galactic coordinates (l, b). The asterisk at the centre corresponds to the direction of the CMB dipole. Errorbars are $1\text{–}\sigma$ uncertainties derived from the analysis of the mock catalogues. The contours are set at constant misalignment angle from the apex of the CMB dipole, in steps of $\Delta\theta = 10°$.

poses. Firstly, consistency between predicted and observed velocities lends support to the hypothesis that structure grew by gravitational instability and gives confidence in the integrity of the observational data. Secondly, the comparison allows an estimate of the parameter $\beta = \Omega_0^{0.6}/b$.

The determination of bulk flows from peculiar velocity surveys is prone to systematic errors. For example, zero-point errors in the calibration of the distance indicators coupled with limited sky coverage may mimic a bulk flow. Similarly, the coupling of large intrinsic errors in distance measurements with inhomogeneities in the density distribution (the inhomogeneous Malmquist bias) also results in a spurious outflow. Thus to perform an unbiased comparison with theoretical predictions requires full-sky, homogeneous surveys of peculiar velocities and an accurate model of the survey's window function.

In Fig. 4.18 we plot observational determinations of bulk flows derived from four (almost) independent datasets. The black triangles (taken from Strauss 1997) represent the cumulative bulk flow in the *Mark*III catalogue (Dekel 1997). The sparse and noisy *Mark*III velocities have been smoothed assuming that the velocity field is irrotational. This guarantees that a unique three–dimensional velocity field is derivable from the observed radial velocities, as in the POTENT method (Dekel, Bertschinger & Faber 1990). The resulting three–dimensional peculiar velocity field, smoothed with a $12\,h^{-1}$Mpc Gaussian, and defined on a regular grid is directly comparable to our model prediction. The black square shows the estimate by da Costa *et al.* (1996) of the bulk velocity on a scale of 60 h^{-1}Mpc, derived from the SFI catalogue of peculiar velocities (Giovanelli *et al.* 1997a, 1997b), using a POTENT–smoothing technique similar to the one applied to the *Mark*III data. The open pentangle is the bulk velocity inferred from 44 supernovae Type Ia by Riess, Press & Kirshner (1995), as reported by Dekel (1997). The effective radius of this last measurement is much smaller than the depth of the sample because the data were weighted by the inverse of the errors. Finally, the open circle at large distance shows the bulk velocity derived by LP94 from a sample of brightest cluster galaxies. The directions of the observed bulk velocity vectors are given in Fig. 4.18b. For the *Mark*III and supernovae estimates, they have been estimated from data within $50\,h^{-1}$Mpc, and for the SFI from data within $60\,h^{-1}$Mpc. The direction of the Lauer & Postman (1994, LP94) bulk flow is taken from Strauss (1997) and refers to a depth of $\sim 90\,h^{-1}$Mpc.

Except for the LP94 result, there is excellent agreement between the various determinations of the bulk flow in Fig. 4.18. These may be compared with the bulk flows predicted by the *PSCz* survey, indicated by the shaded region which encloses the 1–σ allowed range. The lower panel shows the cumulative bulk flow as a function of distance, normalized to $\beta = 0.76$ while the upper panel shows its SGY component only, this time normalized to $\beta = 0.55$. The filled circle in Fig. 4.18b marks the direction of the model bulk velocity vector within $50\,h^{-1}$Mpc.

Requiring that the amplitude of the predicted bulk flow should match the directly

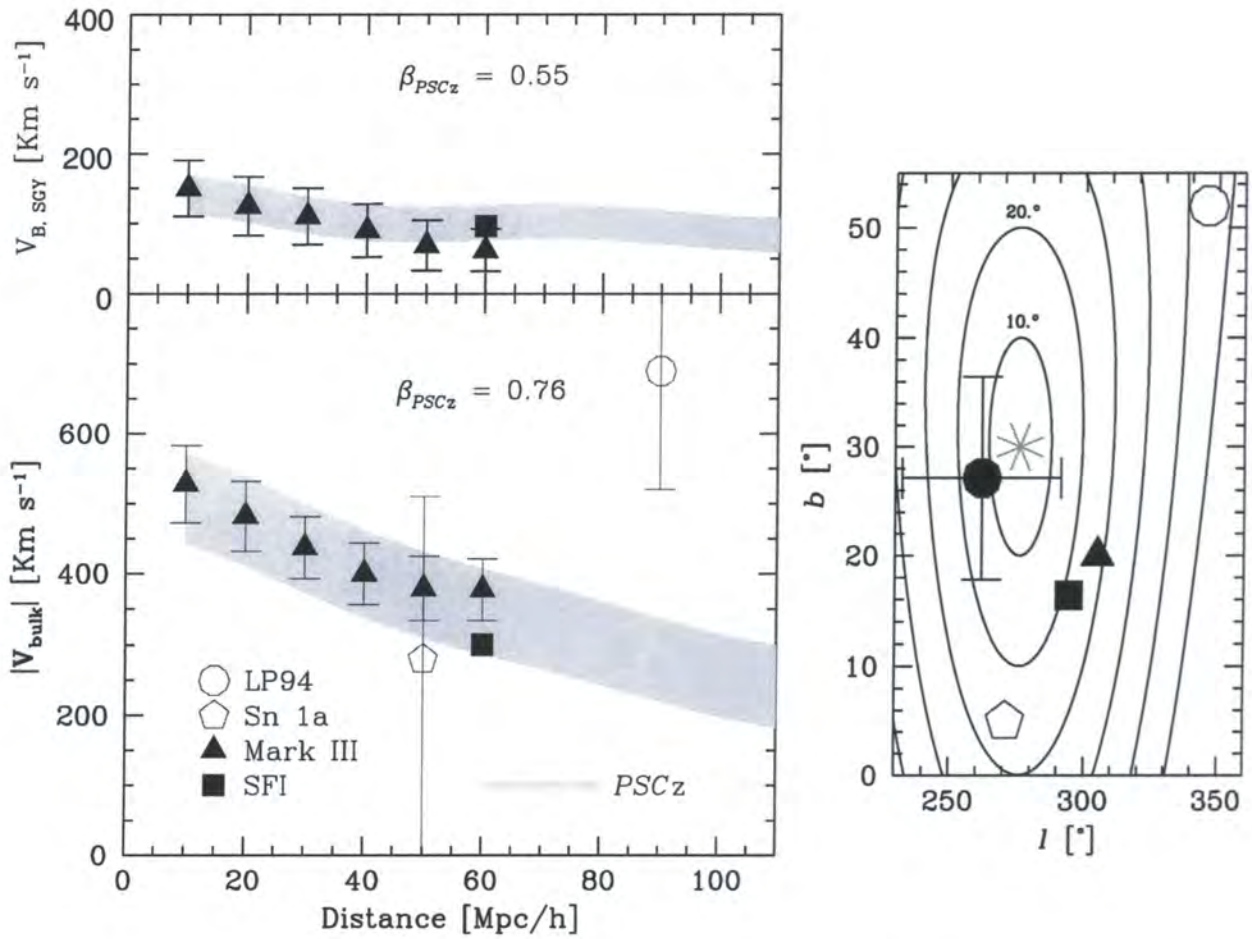

Figure 4.18: The amplitude (left) and direction (right) of the cumulative bulk velocity vector. The bottom–left panel refers to the total velocity and the top–left panel to the SGY–component only. The filled triangles show the bulk velocity measured in the *Mark*III catalogue and the filled square the bulk velocity measured in the SFI catalogue. The empty pentagon shows the bulk flow inferred from a survey of 44 Type Ia supernovae by Riess, Press & Kirshner (1995), while the empty circle gives the bulk velocity derived by Lauer & Postman (1994) from a survey of brightest cluster galaxies. The shaded region is the 1–σ range of the bulk velocity predicted from the *PSCz* gravity field using Method 1 corrected to include the effect of long-wavelength modes. In the lower panel the model predictions are normalized to $\beta = 0.76$, while in the upper panel they are normalized to $\beta = 0.55$. In the right-hand panel, the asterisk marks the direction of the CMB dipole in galactic coordinates and the filled circle the direction of the bulk velocity at $50\,h^{-1}$Mpc obtained from the corrected Method 1 and the *PSCz* survey. The other symbols correspond to those in the left-hand panel, to a distance of $50\,h^{-1}$Mpc in the case of the *Mark*III catalogue.

measured value gives an estimate of β. In obtaining this estimate we shall ignore the discrepant LP94 result which Strauss *et al.* (1995b) and Watkins and Feldman (1995), amongst others, have argued is inconsistent with currently acceptable cosmological models. This is also inconsistent for our model bulk flow which only relies on the gravitational instability and linear biasing hypotheses. As shown in Fig. 4.18, matching the amplitude of the LP94 bulk flow would require a value of $\beta = 1.87$, which is not only incompatible with all the current measurements (e.g. Table 1 in Dekel 1997) but also does not help in reducing the very large misalignment of 70° between the two vectors.

Recent analyses of existing peculiar velocity catalogues show some inconsistencies in the calibration of distance indicators which may result in spurious bulk flow signals (Willick and Strauss 1998). For this reason we limit our comparison of model and observed bulk flows by imposing a series of restrictions designed to minimize possible systematic errors. This should return an unbiased, if somewhat less accurate, estimate of β. These restrictions are:

– We consider only *Mark*III and SFI bulk velocities which, like the *PSCz* model velocity field, have been smoothed onto a regular grid and filtered on a similar scale. This ensures that the comparison is as homogeneous as possible.

– We exclude scales below $20\,h^{-1}$Mpc since small differences in the smoothing procedures applied to model and observed velocities in the the nearby region can bias the comparison.

– We do not consider *Mark*III velocities at distances greater than 30 h^{-1}Mpc because beyond this distance, doubts have been expressed about the integrity of the *Mark*III data by Davis, Nusser & Willick (1996) and by Willick & Strauss (1998). At smaller distances, on the other hand, there is no evidence for any systematic effects in the *Mark*III data and, furthermore, the bulk flow inferred from them agrees well with that inferred from the SFI data, as shown in Fig. 4.18.

From these considerations, the most reliable estimate of β is obtained by comparing the amplitude of the *Mark*III cumulative bulk flow at $30\,h^{-1}$Mpc (440 ± 45 km s^{-1}) with the *PSCz* model bulk velocity returned by Method 1 at this same distance ($(576 \pm 84)\beta$ km s^{-1}). This gives $\beta = 0.76 \pm 0.13$, where the errors are 1–σ. Performing the comparison between the model and SFI bulk velocities at $60\,h^{-1}$Mpc gives a consistent result, $\beta = 0.67 \pm 0.16$. This consistency is reassuring because the SFI data, unlike the *Mark*III data, show no systematic differences with the 1.2-Jy gravity field (da Costa *et al.* 1996). These β estimates have been obtained after correcting for systematic errors in the predicted bulk flow that we have obtained from the *PSCz* mock catalogues. As shown above, systematic uncertainties in the model bulk flows are greatly reduced when we consider its SGY component which is the least affected by the zone-of-avoidance. To minimise the uncertainties associated with this empirical correction we compare the SGY component of the *Mark*III cumulative bulk flow (110 ± 40 km s^{-1}) with the *PSCz* model bulk velocity ($(202 \pm 49)\beta$ km s^{-1}) at $30\,h^{-1}$Mpc . This returns a value of $\beta = 0.55 \pm 0.25$ ($\beta = 0.54 \pm 0.28$ if the SFI bulk

velocity is compared instead) which, given the large uncertainties, is still consistent with the one previously obtained at $1\text{-}\sigma$ level.

4.7 Discussion and conclusions

The recently completed *PSCz* redshift survey of *IRAS* galaxies represents an almost ideal dataset for studying the mass distribution and the gravity field in the local universe. In this chapter we have used the *PSCz* survey to develop a nonparametric model of the local cosmic velocity field which supersedes results derived from the shallower 1.2-Jy and the sparser QDOT surveys. Our reconstructions are based on the assumptions that cosmic structure has grown by gravitational instability and that fluctuations in the galaxy distribution are proportional to fluctuations in the mass distribution. We have paid particular attention to a careful estimation of random and systematic errors using a suite of mock *PSCz* catalogues constructed from large cosmological N–body simulations. As a further check on the validity of our results, we have implemented two independent methods for reconstructing the *PSCz* model velocity fields, both of which give consistent results.

Because of the large size of the *PSCz* survey, the density and velocity fields can be reliably reconstructed out to a depth of $150\,h^{-1}$Mpc. We have presented maps of the galaxy distribution which, with a smoothing radius of only $6\,h^{-1}$Mpc, clearly show the relative sizes of the main structures that characterize our local universe. The two largest peaks in our neighbourhood are the Great Attractor, made up of the Hydra–Centaurus and Pavo–Indus–Telescopium superclusters, and the Perseus–Pisces supercluster located in roughly the opposite direction on the Supergalactic plane. The Local, Coma-A1367, and Camelopardalis superclusters as well as the Cetus Wall are clearly visible in our maps, and the giant Shapley concentration appears near the edge of the survey, behind the Great Attractor. The largest underdensity in our vicinity is the well-known Sculptor void, but this is almost matched in size by a void in the background of the Camelopardalis supercluster. Three more underdense regions that exert an important influence on the local dynamics are the voids in the foreground of Coma, in the background of the Perseus–Pisces complex, and behind the Great Attractor.

The local velocity field implied by the *PSCz* density field is complex. The dominant features are the large infall patterns towards large mass concentrations in the Great Attractor, Perseus–Pisces and Coma regions. Superimposed upon these are impressive coherent flows along a ridge between Cetus and Perseus–Pisces and along the Camelopardalis–Virgo–Great Attractor–Shapley direction. We see no prominent back-infall onto the Great Attractor. Instead, the flow in this region results from the interplay between the compressional push of two nearby voids and the pull of the Shapley Concentration on much larger scales.

The *PSCz* reconstruction agrees well with results from the 1.2-Jy survey within $80\,h^{-1}$Mpc,

the region in which the latter provides adequate sampling. The only noticeable difference is the predicted bulk velocity vectors (in the CMB frame) which differ in the two surveys by $\sim 130\beta$ km s^{-1}in each Cartesian component. This discrepancy arises from uncertainties in the way in which the zone-of-avoidance is filled in and from errors in the transformation of the predicted peculiar velocities from the Local Group to the CMB frame. While the former affect the *PSCz* and 1.2-Jy results equally, the latter are more severe in the 1.2-Jy case because of the larger shot noise. Thus, the misalignment between the Local Group acceleration and the CMB dipole vectors is $\sim 25°$ for the 1.2-Jy survey compared with only $\sim 15°$ in the *PSCz* survey (Schmoldt *et al.* 1998).

As we saw in § 4.5.1, the density and velocity fields inferred from the *PSCz* survey agree well with those inferred from a sample of Abell/ACO clusters. This is perhaps surprising since clusters are selected in a very different way from galaxies, but it is reassuring and suggests that systematic errors are under control in both cases. Comparison of the two model density and velocity fields, smoothed on the same cubic grid, out to a distance of $140\,h^{-1}$Mpc, gives the relative linear bias, b_c, between the rich cluster and *PSCz* galaxy populations. A χ^2 analysis of the density–density and velocity–velocity comparisons gives very similar results in both cases, $b_c = 4.4 \pm 0.6$ and $b_c = 4.7 \pm 0.6$, respectively. These values are consistent with the estimate, $b_c = 4.5$, obtained by Peacock and Dodds (1994) from an analysis of phenomenological power spectra. A more detailed comparison of the relative bias field of clusters and galaxies will be presented in Plionis *et al.* (1999).

Finally, from the reconstructed *PSCz* peculiar velocity field we have estimated the bulk velocities of concentric spheres around us. Comparison of these bulk flows with independently measured peculiar velocities yields an estimate of the parameter $\beta = \Omega^{0.6}/b$. In order to perform a homogeneous comparison while minimizing possible biases due to the *Mark*III–*IRAS* mismatch discussed above, we restricted this comparison to the amplitude of the *PSCz* model and the *Mark*III bulk velocities at $30\,h^{-1}$Mpc. This gave our best estimate, $\beta = 0.76 \pm 0.13$. A similar comparison, but using the bulk flow measured in the SFI survey at $60\,h^{-1}$Mpc (Giovanelli *et al.* (1997a, 1997b), returned a consistent estimate of β. To further minimize possible biases in the predicted bulk flow we also compared the SGY components of the *PSCz* and the *Mark*III bulk flow vectors, resulting in a lower value of $\beta = 0.55 \pm 0.25$ still consistent with the previous one within $1\text{–}\sigma$ level. These estimates of β are also consistent with results from analyses of the *PSCz* dipole (Schmoldt *et al.* 1998, Rowan–Robinson *et al.* 1999), and with the most recent determinations of β from velocity–velocity comparisons (Davis, Nusser & Willick 1996, da Costa *et al.* 1996, Willick *et al.* 1997b, Willick & Strauss 1998).

A determination of β to 15% accuracy is possible by comparing the peculiar velocity field inferred from the *PSCz* survey with measured peculiar velocities at independent locations. An analysis of this kind based on the likelihood VELMOD technique (Willick *et al.* 1997b) is currently in progress.

Chapter 5

PSCz – 1.2-Jy Comparison.

5.1 Introduction

In the context of linear gravitational instability (GI) theory and linear biasing a comparison between the predicted and observed peculiar velocity provides us with a combination of the mean density parameter, Ω_0, and the linear biasing parameter, b, given by:

$$\beta \equiv \frac{\Omega_0^{0.6}}{b}. \tag{5.1}$$

Recently, several analyses comparing the *IRAS* 1.2-Jy gravity field with the *Mark*III velocity field have been carried out by Davis, Nusser & Willick (1996), Willick *et al.* (1997b), Willick and Strauss (1998), Sigad *et al.* (1998) and Dekel *et al.* (1998b). These studies show that both fields are qualitatively rather similar, supporting the assumption that the growth of the large scale structure is due to gravity (although other mechanisms are also possible to explain the correlation between observed velocities and predicted gravity *cf.* Babul *et al.* 1994). Detailed quantitative comparisons are however, at present, less satisfactory. Davis, Nusser & Willick (1996) in applying the method introduced by Nusser & Davis (1995) (ITF analysis) found coherence in the residuals between the *IRAS* 1.2Jy and *Mark*III data which prevents a conclusive determination of β. Willick *et al.* (1997b) find a better agreement using the rather different *VELMOD* technique. However they only applied it to the *Mark*III galaxies within the redshift limit[1] $s = 3\,000\,\mathrm{km\,s^{-1}}$. In a more recent paper, Willick & Strauss (1998) show that it is possible to find good agreement for galaxies within a redshift limit $s = 7\,500\,\mathrm{km\,s^{-1}}$ if the Tully–Fisher relation for various subsamples going into *Mark*III catalogue are re-calibrated. However, such calibrations are inconsistent with the original work of Willick *et al.* (1997a) placing the objects belonging to two of the samples which make-up *Mark*III 8% closer.

The main goal of this chapter is to check if the discrepancies between the 1.2-Jy predictions and the measured velocities in *Mark*III are intrinsic to the predicted velocity

[1] Throughout this chapter we apply the convention $s \equiv cz_{\,LG}$

field. Thus, we compare the overdensity and radial peculiar velocity fields inferred from the *IRAS PSCz* survey with those inferred from 1.2-Jy (henceforth we are going to use the *PSCz* and 1.2-Jy to denote *IRAS PSCz* and *IRAS* 1.2-Jy surveys, respectively). Since the former dataset is deeper and better sampled, such comparison may give us clues as to whether or not improved redshift surveys might provide a better match to the *Mark*III data-set than Davis, Nusser and Willick (1996) found.

In § 5.2 we describe how to compare the velocity and overdensity fields inferred from redshift surveys with different spatial sampling. The galaxy catalogues are introduced in § 5.3. Section § 5.4 describes the overdensity inferred from both redshift surveys. The predicted radial velocity fields from both *IRAS* surveys are described in § 5.5, including a detailed study of the first three spherical harmonics coefficients. Finally, section § 5.6 contains a discussion of the results and suggestions for future work.

5.2 Spherical Harmonic Coefficients of the Overdensity and Velocity fields.

Our analysis relies on a spherical harmonics expansion, $Y_{lm}(\hat{\mathbf{s}})\{l = 0, .., \infty; |m| \leq l\}$, of the overdensity, $\delta(\mathbf{s})$, and radial peculiar velocity, $u(\mathbf{s})$, fields in redshift space. The spherical coefficients $\psi_{lm}(s)$ of an arbitrary field $\psi(\mathbf{s})$ are related by:

$$\psi_{lm}(s) = \int \psi(\mathbf{s}) Y^*_{lm}(\hat{\mathbf{s}}) d\Omega \tag{5.2}$$

$$\psi(\mathbf{s}) = \sum_{l=0}^{\infty} \sum_{m=-l}^{l} \psi_{lm}(s) Y_{lm}(\hat{\mathbf{s}}). \tag{5.3}$$

Where * indicates a complex conjugate. Since the overdensity and peculiar velocity fields are real, we use the real–valued spherical harmonics $\mathcal{Y}_{lm}\ (\hat{\mathbf{s}})\{l = 0, .., \infty; |m| \leq l\}$ following Baker *et al.* (1998) and Bunn (1995) (see also Jackson 1962). For a given l these special functions are normalized by the value of $\mathcal{Y}_{l0}$ at the North Galactic Pole. Thus, the amplitude of the l^{th}–multipole, $\psi_l(s)$, is simply the quadrature sum over the $(2l + 1)$-spherical coefficients:

$$\psi_l(s) = \left[\sum_{m=-l}^{m=l} \psi'^2_{lm}(s) \right]^{\frac{1}{2}}. \tag{5.4}$$

Where $\psi'_{lm}(s)$ are the spherical harmonic coefficients as we replace $Y_{lm}(\hat{\mathbf{s}})$ by $\mathcal{Y}_{lm}(\hat{\mathbf{s}})$ in eqns. (5.2) and (5.3).

5.2.1 Peculiar velocity and overdensity fields from the Distribution of Galaxies in Redshift Space

Nusser & Davis (1994) show that in linear gravitional instability (GI) theory the peculiar velocity field in redshift space is irrotational and thus can be expressed in terms of a poten-

tial: $\mathbf{v(s)} = -\nabla\Phi(\mathbf{s})$. As already discussed in previous chapters, the angular dependencies of the potential velocity field and the galaxy overdensity field (both measured in redshift space and expanded in spherical harmonics, $\Phi_{lm}(s)$ and $\hat{\delta}_{lm}(s)$, respectively) are related by a modified Poisson equation:

$$\frac{1}{s^2}\frac{d}{ds}\left(s^2\frac{d\Phi_{lm}}{ds}\right) - \frac{1}{1+\beta}\frac{l(l+1)\Phi_{lm}}{s^2} = \frac{\beta}{1+\beta}\left(\hat{\delta}_{lm} - \frac{1}{s}\frac{d\ln\phi}{d\ln s}\frac{d\Phi_{lm}}{ds}\right), \qquad (5.5)$$

where $\phi(s)$ is the selection function. To solve this differential equation we first compute the density field on an angular grid using cells of equal solid angle and 52 bins in redshift out to $s = 18\,000\,\mathrm{km\,s^{-1}}$.

Since our aim is to compare fields (for instance, density fields) inferred from two different datasets, we must perform the computations on a grid with the same spatial resolution. Thus, the radial bin sizes are set proportional to the 1.2-Jy interparticle separation, $\sigma_{1.2}(s) = [\bar{n}_{1.2}\phi_{1.2}(s)]^{-1/3}$, because this survey is the more sparse of the two. Henceforth the subscripts 1.2 and 0.6 denote 1.2-Jy and *PSCz*, respectively. To estimate the mean density of the catalogue j $\{j = 0.6, 1.2\}$ we consider

$$\bar{n}_j = \frac{1}{V_j}\sum_i \frac{1}{\phi_j(s_i)}. \qquad (5.6)$$

Where the sum is over the objects within the sample volume V_j. These volumes are computed in the following way: first, we estimate the 1.2-Jy mean density accounting for galaxies within $s_{\max 1.2} = 8\,000\,\mathrm{km\,s^{-1}}$; second, we repeat the same estimation but using the *PSCz* galaxies within a radius for which this survey's interparticle separation, $\sigma_{0.6}(s) = [\bar{n}_{0.6}\phi_{0.6}(s)]^{-1/3}$, is that of the 1.2-Jy at $8\,000\,\mathrm{km\,s^{-1}}$. From Fig. 4.2 it is straightforward to verify that such a radius is $s_{\max 0.6} = 12\,000\,\mathrm{km\,s^{-1}}$. The Gaussian–smoothed galaxy overdensity field at a grid point n, for a catalogue j $\{j = 0.6, 1.2\}$ is given by:

$$1 + \hat{\delta}_j(\mathbf{s}_n) = \frac{1}{(2\pi)^{3/2}\sigma_{1.2n}^3}\sum_i^{N_j}\frac{1}{\phi(s_i)}\exp\left[-\frac{(\mathbf{s}_n - \mathbf{s}_i)^2}{2\sigma_{1.2n}^2}\right] \qquad (5.7)$$

where the sum is over all galaxies within the catalogue j, N_j. The Gaussian smoothing width for the cell n at redshift s_n, $\sigma_{1.2n}$, is given by $\sigma_{1.2n} = \sigma_{1.2}(s_n)$ (or $100\,\mathrm{km\,s^{-1}}$ when such a length is smaller than this). This smoothing scheme is tailored to keep the uncertainties caused by shot-noise in the inferred $\hat{\delta}_{1.2}(s)$ roughly constant throughout the volume of the 1.2-Jy redshift survey, since of the two inferred density fields this is the most affected by this source of uncertainty. This scheme is analogous to the optimal Wiener filtering procedure (Lahav *et al.* 1994; Fisher *et al.* 1995b)

In eqn. (5.5) we assume linear theory and a one-to-one mapping between distance and redshift along any line of sight. Such assumptions are not valid in clusters where the smoothed density field still shows appreciable triple-valued regions around clusters. Thus, we apply the same procedure as Yahil *et al.* (1991) for collapsing the fingers of God associated with the six nearby clusters present in their Table 2.

5.3 Datasets

PSCz is a collaboration involving several British institutions (Durham, Oxford, Edinburgh and Cambridge) which have recently finished a catalogue containing some 15500 *IRAS* PSC (Point Source Catalogue) galaxies with a 60 μm flux larger than 0.6-Jy. The average depth of this survey is $\sim$ 100 h^{-1}Mpc covering 80% of the sky. The unobserved parts of the sky are filled-in with the same cloning procedure which we applied in the two previous chapters. The reader can find further details of this survey in chapters § 3 and § 4. The 1.2-Jy catalogue (Fisher *et al.* 1995a) contains 5321 *IRAS* PSC galaxies with a 60 μm limit of 1.2-Jy which cover 87.6% of the sky. The median redshift is 84 h^{-1}Mpc. In this chapter we use a version of this catalogue which Yahil *et al.* (1991) have supplemented with "synthetic" objects in the ZoA and other excluded regions. This filling-in of the masked regions was performed without biasing the statistics of the galaxy distribution. The reader should notice that this version is slightly different to the one extensively used in chapter § 4, as we apply slightly different filling-in procedures. In all datasets or sub-datasets which we consider, the redshifts are in the Local Group frame. The selection function parameters and the mean number density of both surveys are shown in Table (5.1).

5.4 The *IRAS PSCz* and 1.2-Jy Overdensity Fields

We have reconstructed our overdensity fields, in redshift space, for all galaxies within a sphere of 18 000 km s^{-1}. The harmonics are computed up to $l_{\max} = 16$. This truncation produces an effective angular resolution of $\Delta\theta \approx \frac{\pi}{l_{\max}}$ radians (cf. Peebles 1980) which at redshift s corresponds to a maximum spatial resolution of $\Delta s \approx \frac{\pi s}{l_{\max}}$. Within $s \approx$ 6 000 km s^{-1} this is slightly smaller than $\sigma_{1.2}(s)$ of our smoothing procedure, eqn. (5.7). We apply a correction factor to account for part of the Gaussian-weighted volumes which fall outside the survey cut-off.

5.4.1 Overdensity Maps

Figs. 5.1–5.3 show Aitoff projections of the redshift space overdensity field in three radial Gaussian–shells at s = 1 000, 3 000 and 5 000 km s^{-1}, respectively. The radial size of such shells is defined by the width applied to Gaussian-smooth the overdensity field at the radial position of the shell. The overdensity maps are plotted in Galactic coordinates.

The most obvious feature common to the three Gaussian-shells is that the *PSCz* overdensity field is in general larger than its 1.2-Jy analogue, (*cf.* bottom panels of Figs. 5.1–5.3 where the positive values of the residuals, $\delta_{res}(s) = \delta_{0.6}(s) - \delta_{1.2}(s)$, encompass a larger area of the sky than the negative ones). Baker *et al.* (1998) in their comparison of the *IRAS* 1.2-Jy and ORS galaxies in redshift space show the same features present in our

maps: the Supergalactic Plane where clusters like Hydra, Centaurus, Perseus and Pisces rest and extended voids like the Local Void and Sculptor Void.

In Fig. 5.1 the contours in the two top panels are equally spaced at $\Delta\delta = 1.0$ while $\Delta\delta_{res} = 0.25$ in the bottom panel. The Virgo cluster, ($l \simeq 240°$, $b \simeq 75°$), is the most prominent overdensity and spans over $\sim 60°$ in the northern Galactic hemisphere. Fornax, ($l \simeq 237°$, $b \simeq -54°$), appears as the only overdensity in the South hemisphere and it is connected to Virgo across the Galactic Plane. The observed elongation on the isocontours around Virgo at ($l \simeq 145°$, $b \simeq 66°$) is due to the Ursa Major cluster. For a Gaussian smoothing of $345\,\mathrm{km\,s^{-1}}$ on this shell the overdensity field of both surveys is rather similar at the location of the identified overdensities. However, the large void that is seen in 1.2-Jy centered at $0° < l < 180°$, is not found in the *PSCz* overdensity field. Instead, in *PSCz* there are two voids at ($l \simeq 180°$, $b \simeq 0°$) and ($l \simeq 60°$, $b \simeq -50°$) separated by a small overdensity which is an extension of the Ursa Major cluster across the Galactic plane at $l \simeq 120°$. The residuals' map, lower panel, features positive values over most of the sky. The two major peaks are at ($l \simeq 0°$, $b \simeq 0°$) with $\delta_{res} \sim 2.75$ and at ($l \simeq 100°$, $b \simeq 0°$) where $\delta_{res} \sim 1.25$ within the Zone of Avoidance (ZoA). The former coincides with the widest part of the *PSCz* mask whilst the latter coincides with the extension of Ursa Major over the Galactic plane in the *PSCz* maps. On this shell the residuals only assume negative values around the Virgo cluster where $\delta_{res} \sim -0.5$. There is the possibility that the cloning procedure applied to *PSCz* might exaggerate the contribution of structures close to the Galactic plane. In the innermost regions the incompleteness of the faint galaxies may also be a source of uncertainty in the density field (Rowan-Robinson *et al.* 1990). To account for this problem we set the *PSCz* selection function equal to unity within $600\,\mathrm{km\,s^{-1}}$.

In Fig. 5.2, $s = 3\,000\,\mathrm{km\,s^{-1}}$, the isocontours are $\Delta\delta = 0.5$ and $\Delta\delta_{\mathrm{res}} = 0.25$ in the top two panels and bottom panel, respectively. The applied Gaussian filter has a characteristic smoothing length of $550\,\mathrm{km\,s^{-1}}$. On this redshift slice even though both inferred overdensity fields are qualitatively similar, the residuals have positive values across most of the sky. The clusters Hydra ($l \simeq 270°$, $b \simeq 20°$) and Centaurus ($l \simeq 300°$, $b \simeq 20°$) are clearly seen. The Hydra–Centaurus system runs across the Galactic Plane out to Pavo–Indus–Telescopium ($l \simeq 270°$, $b \simeq -30°$), while the back-side of Fornax appears at ($l \simeq 210°$, $b \simeq -30°$). The Supergalactic Plane is visible near $l \simeq 135°$ all across the Northern Galactic Hemisphere. The positive isocontour at very high Galactic latitude near $l \simeq 240°$ can be identified with Leo. There are also some large voids extending across the sky: at ($l = 5°$, $b = 10°$) and the so-called Local Void (Tully 1987) at $l = 265°$, $b = -50°$. The magnitude of the differences between the fields *PSCz* and 1.2-Jy density fields show the same trend as in the innermost shell.

At $s = 5\,000\,\mathrm{km\,s^{-1}}$, Fig. 5.3, the smoothing length is $815\,\mathrm{km\,s^{-1}}$. The two largest clusters, Perseus-Pisces, at ($l = 140°$, $b = -25°$) and Pavo–Indus, at ($l = 330°$, $b < -20°$) are very alike in the two surveys. The background of Hydra at $l = 280°$, $b \simeq 10°$ also shows a similar appearance in both fields. However, Cancer ($l = 190°$, $b = 25°$) and

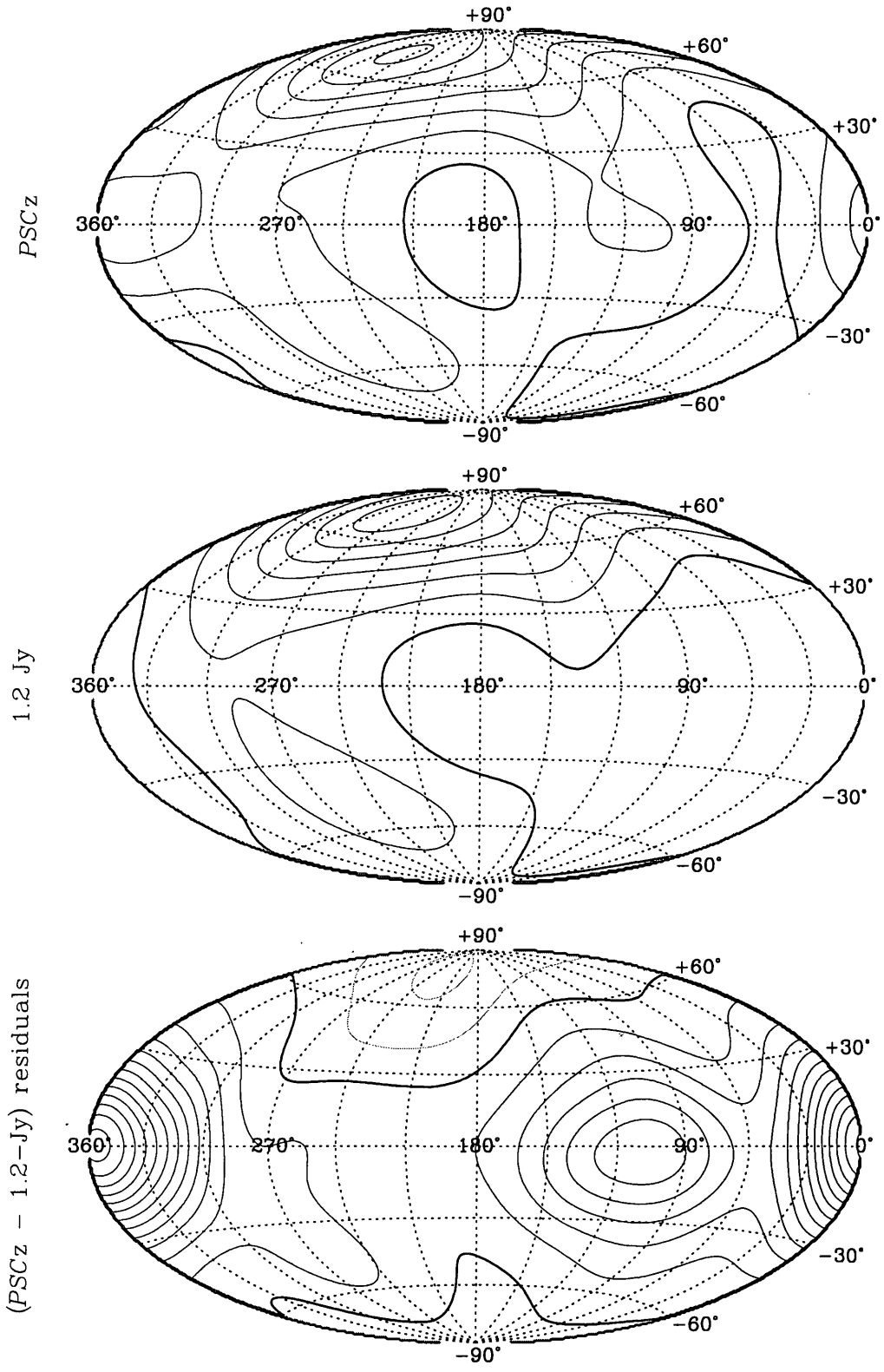

Figure 5.1: Comparison between the *PSCz* smooth overdensity field (top panel) and the 1.2–Jy analogue (middle panel) in a Gaussian–shell at $s = 1\,000\,\mathrm{km\,s^{-1}}$. The residuals appear in the bottom panel. The Gaussian smoothing width is $\sigma_{1.2} = 345\,\mathrm{km\,s^{-1}}$. The contour spacing is 1.0 in the two top panels and 0.25 in the bottom one. Grey and black lines show $\delta < 0$ and $\delta \geq 0$, respectively. Heavy black lines represent the $\delta = 0$ or $\delta_{res} = 0$ contour.

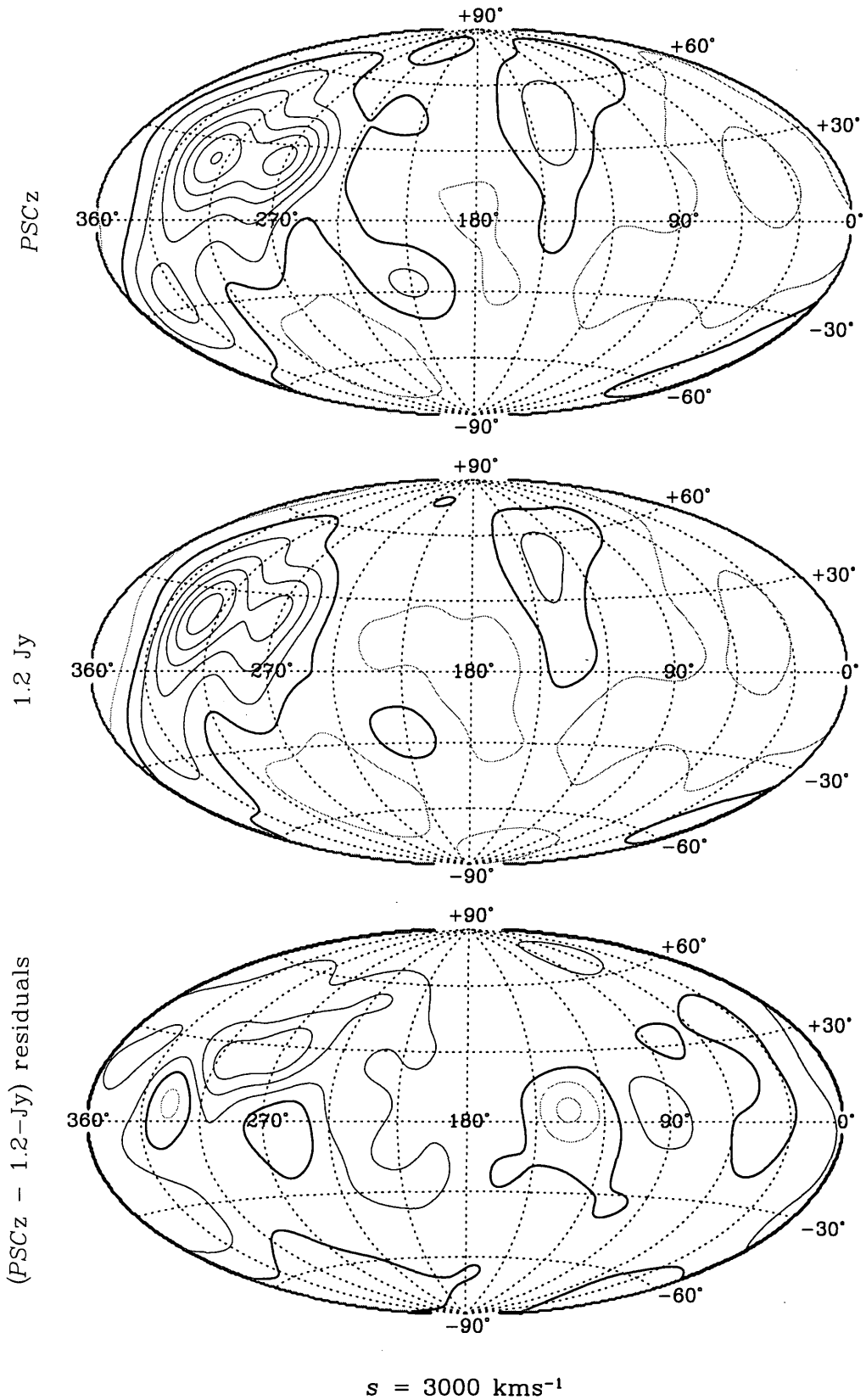

Figure 5.2: Comparison between the *PSCz* smooth overdensity field (top panel) and the 1.2–Jy analogue (middle panel) in a Gaussian–shell at $s = 3\,000\,\mathrm{km\,s^{-1}}$. The residuals appear in the bottom panel. The Gaussian smoothing width is $\sigma_{1.2} = 550\,\mathrm{km\,s^{-1}}$. The contour spacing is 0.5 in the two top panels and 0.25 in the bottom one. Grey and black lines show $\delta < 0$ and $\delta \geq 0$, respectively. Heavy black lines represent the $\delta = 0$ or $\delta_{res} = 0$ contour.

Orion ($l = 190°$, $b = -25°$) which in the 1.2-Jy survey look like separate identities, in the *PSCz* density field appear as extensions of the Perseus–Pisces supercluster. At this level of smoothing the small amplitude of the residuals over most of the sky confirms the good visual agreement between both overdensity fields.

5.4.2 Radially Averaged Overdensity and Density Contrast

To understand the systematically all larger values of the *PSCz* overdensity field relative to the 1.2-Jy counterpart, we compute the overdensity in spheres of increasing redshift, $\bar{\delta}(s)$. We estimate $\bar{\delta}_j(s)$ $\{j = 0.6, 1.2\}$ directly from the redshift distribution:

$$\bar{\delta}_j(s) = \frac{1}{V_{1j}\bar{n}_{1j}} \sum_{i=1}^{N_{p,j}} \frac{W_{\bar{\delta}}(s, \mathbf{s}_i)}{\phi_j(s_i)} - 1, \tag{5.8}$$

where $W_{\bar{\delta}}(s, \mathbf{s}_i) \equiv H(s - s_i)H(|b_i| - 10°)$ represents the window function and H indicates the Heaviside function. The sum is over the $N_{p,j}$ galaxies belonging to the catalogue j which has a selection function $\phi_j(s)$. V_{1j} is the sample volume used to compute the mean number density $\bar{n}_{1j}$ defined by $V_{1j} \equiv \int_0^{s_{\max j}} W_{\bar{\delta}}(s, \mathbf{s}')d^3s'$, where $s_{\max j} = 12\,000$ and $8\,000\,\mathrm{km\,s^{-1}}$ for the *PSCz* and 1.2-Jy, respectively. Since V_{1j} does not contain the ZoA we may verify whether the inferred $\bar{\delta}_j(s)$ $\{j = 0.6, 1.2\}$ are intrinsically different, without uncertainties caused by the filling-in procedure of the ZoA. Fig. 5.4a illustrates the estimates of $\bar{\delta}(s)$ for both catalogues as function of s in spheres of radius ranging from 0 to $15\,000\,\mathrm{km\,s^{-1}}$ in steps of $200\,\mathrm{km\,s^{-1}}$, solid -thick and -thin lines represent *PSCz* and 1,2-Jy datasets, respectively. Although the *PSCz* estimate is systematically larger than 1.2-Jy counterpart, within $s = 8\,000\,\mathrm{km\,s^{-1}}$, both survey's estimates show a qualitative similar radial dependence: an overdensity larger than 1.5 at very small radial distance; another peak at $s \approx 1500\,\mathrm{km\,s^{-1}}$ showing the presence of the Virgo and Fornax clusters; a minimum at $s \approx 4\,000\,\mathrm{km\,s^{-1}}$ which is due to Sculptor Void; and a large enhancement about $s \approx 5\,000\,\mathrm{km\,s^{-1}}$ which illustrates the presence of the "Great Attractor" and Perseus–Pisces.

The overdensity in shells of identical thickness $(\delta\rho/\bar{\rho})_j$ can be estimated by:

$$\left(\frac{\delta\rho}{\bar{\rho}}\right)_j(s) = \frac{1}{V_j\bar{n}_j} \sum_{i=1}^{N_{p,j}} \frac{W_{\delta\rho/\bar{\rho}}(s, s_i, \Delta s)}{\phi_j(s_i)} - 1, \tag{5.9}$$

where the sum is over all $N_{p,j}$ galaxies within the catalogue j while $W_{\delta\rho/\bar{\rho}}(s, s_i, \Delta s) \equiv H(s + \Delta s/2 - s_i)H(s_i + \Delta s/2 - s)$ is the window function. Fig. 5.4b shows $(\delta\rho/\bar{\rho})_j$ estimated from the redshift distribution of both surveys up to $s = 15\,000\,\mathrm{km\,s^{-1}}$ in shells of constant thickness, set equal to $\Delta s = 200\,\mathrm{km\,s^{-1}}$. The coarse -thick and -thin lines illustrate *PSCz* and 1.2-Jy, respectively. The former has systematically larger overdensities within $s = 6\,000\,\mathrm{km\,s^{-1}}$. The major features of this field coincide in both surveys and have already been described when analysing $\bar{\delta}(s)$: there is a local overdensity larger than 1.5 at $s \leq 200\,\mathrm{km\,s^{-1}}$; Virgo and Fornax are apparent $s \sim 11\,00\,\mathrm{km\,s^{-1}}$ where $\delta\rho/\bar{\rho} \geq 1.0$; in both surveys $\delta\rho/\bar{\rho}$ assumes negative values, ≤ -0.1, at about $s \sim 3\,500\,\mathrm{km\,s^{-1}}$ which

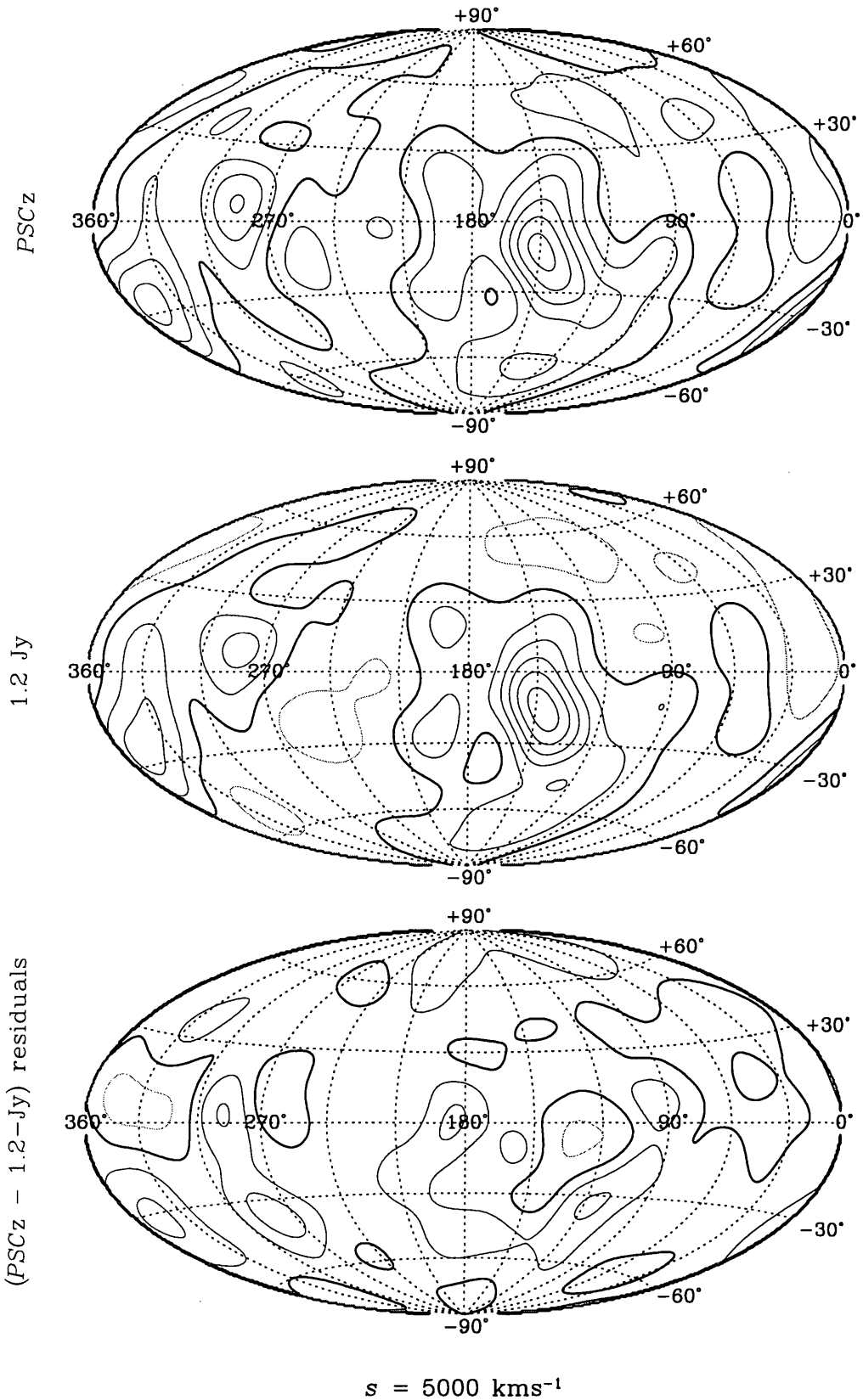

Figure 5.3: Comparison between the *PSCz* smooth overdensity field (top panel) and the 1.2–Jy analogue (middle panel) in a Gaussian–shell at $s = 5\,000\,\mathrm{km\,s^{-1}}$. The residuals appear in the bottom panel. The Gaussian smoothing width is $\sigma_{1.2} = 815\,\mathrm{km\,s^{-1}}$. The contour spacing is 0.5 in the two top panels and 0.25 in the bottom one. Grey and black lines show $\delta < 0$ and $\delta \geq 0$, respectively. Heavy black lines represent the $\delta = 0$ or $\delta_{res} = 0$ contour.

illustrates the presence of the Sculptor Void and finally, Perseus-Pisces and the "Great Attractor" are clearly seen at about $s \sim 5\,000$ km s^{-1} where the shell overdensity field is larger than 0.2. In Fig. 5.4b we also show the smoothed $\delta_{l=0,\ m=0}(s)$ inferred in our spherical harmonic analysis (*PSCz* –thick continuous line; 1.2-Jy – dashed line). Recall that the monopole, $l = 0$, $m = 0$, term of a field on a shell is by definition the mean value of the considered field over such a volume. The differences between the estimates derived from the considered surveys are also evident in Fig. 5.4b. The *PSCz* estimates are systematicaly larger than their 1.2-Jy counterparts within $s = 6\,000\,\mathrm{km\,s^{-1}}$.

5.5 The *IRAS PSCz* and 1.2-Jy Radial Peculiar Velocity Fields

Since we know the overdensity field we may obtain the potential of the peculiar velocity field by solving eqn. (5.5). We integrate this modified Poisson equation numerically setting $\beta = 0.6$ for both *IRAS* surveys. This is consistent with our previous analysis of the *PSCz* bulk flow, § 4, the Local Group acceleration (Schmoldt *et al.* 1998) and also the 1.2-Jy–POTENT dipole comparison (Nusser & Davis 1994).

5.5.1 Radial Peculiar Velocity Maps

Let us define $u_j(s)$, where $j = 0.6, 1.2$, as the radial peculiar velocity field, $u(\mathbf{s}) = \hat{\mathbf{s}} \cdot \nabla\Phi$, inferred from the survey j and $u_{res}(s) \equiv u_{0.6}(s) - u_{1.2}(s)$ as the residuals between both radial velocity fields. To obtain $u_j(s)$ maps we used $l_{\max} = 16$ while computing the sum over the velocity spherical harmonics coefficients. Figs. 5.5–5.7 show such maps in the same Gaussian-shells as the redshift shells used to illustrate the overdensity field. Although both inferred peculiar radial velocity fields seem qualitatively similar, the residuals plotted in the bottom panels of the figures, assume negative values over most of the sky. The grey and black lines represent positive and negative radial peculiar velocities, respectively, while the heavy black lines indicate the $u_j = 0$ or $u_{res} = 0$ contour level.

Fig. 5.5 shows the isocontours of the line-of-sight component of the velocity field at $s = 1\,000\,\mathrm{km\,s^{-1}}$. The contour spacing is $50\,\mathrm{km\,s^{-1}}$. The major feature of the *PSCz* and 1.2-Jy velocity fields is the dipole component which dominates the flow as a result of the motion of the LG, with infall towards ($l \approx 220°$, $b \approx 30°$) and outward flow in the opposite direction. The residuals between the fields, shown in bottom panel, have a dipolar-like pattern: the maximum and the minimum of such a map are in opposite parts on the sky, ($l \approx 220°$, $b \approx 0°$) and ($l \approx 40°$, $b \approx 0°$), respectively. The difference between the amplitude of these maxima and minima, $\approx -50\,\mathrm{km\,s^{-1}}$ and $\approx 150\,\mathrm{km\,s^{-1}}$, respectively, indicates that there also is a residual monopole component.

In the next redshift shell the dominance by the dipole component is still evident in the two surveys' velocity fields, as can be seen in the top two panels of Fig. 5.6. The

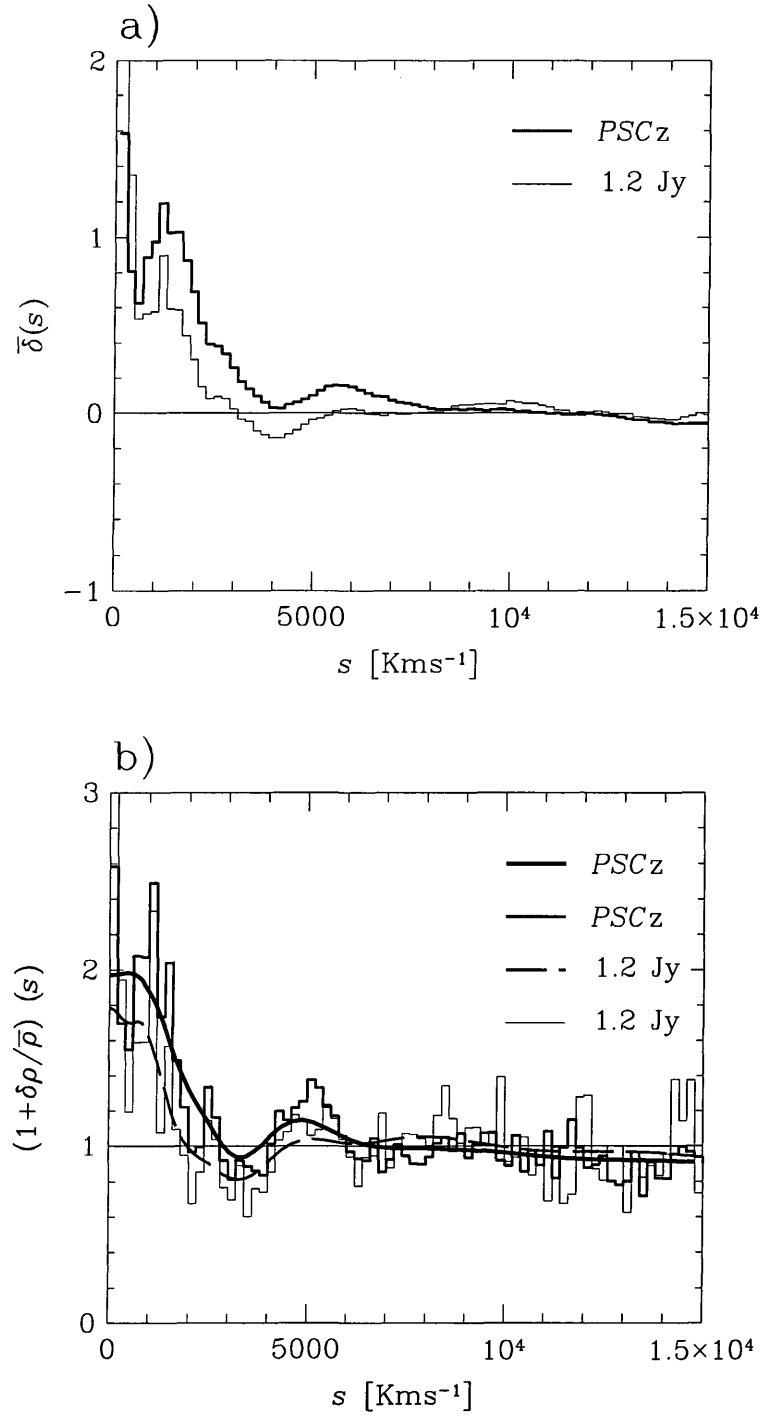

Figure 5.4: The *IRAS* spherical overdensity, $\bar{\delta}(s)$, and shell overdensity contrast, $1 + (\delta\rho/\bar{\rho})(s)$. a) The *PSCz* spherically averaged overdensity is represented by the heavy line while the 1.2-Jy's estimate is denoted by the solid line. b) The *PSCz* density contrast is represented by the coarse-thick line while the 1.2-Jy's estimate is denoted by the coarse-thin line. The thick (thin) smooth solid line illustates the *PSCz* (1.-Jy) density monopole ($\delta_{00}(s)$).

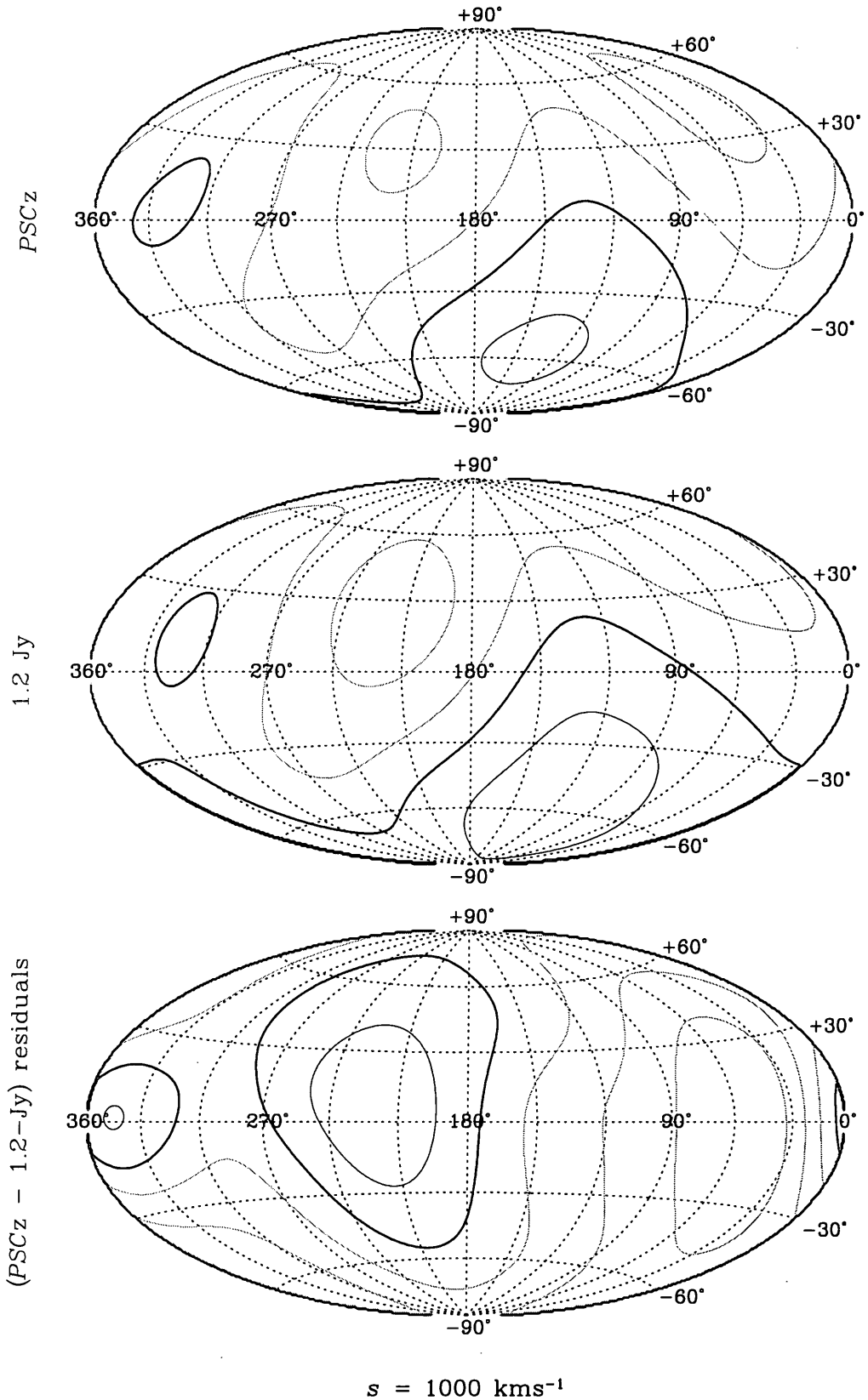

Figure 5.5: *IRAS* velocity field in a shell at $1\,000\,\mathrm{km\,s^{-1}}$. The contour spacing is $50\,\mathrm{km\,s^{-1}}$and the heavy solid lines represent the $u = 0$ or $u_{res} = 0$ contours.

contour spacing is 200 km s^{-1} and 50 km s^{-1} for the two top panels and the bottom panel, respectively. In the two velocity maps, there is an infall on the back side of Virgo and galaxies flowing away from us as they fall roughly into Perseus-Pisces, ($l \approx 120°$, $b \approx -40°$). The residuals show the same pattern as in the previous shell but with a larger monopole component. The largest ($l \approx 180°$, $b \approx 0°$) and smallest ($l \approx 320°$, $b \approx 0°$) values of the residuals are ≈ 0 km s^{-1} and ≈ -400 km s^{-1}, respectively.

At redshift $s = 5\,000$ km s^{-1}the velocity field maps of both surveys (two top panels of Fig. 5.7) again show the same dipole pattern as the two previous shells with galaxies flowing from us toward Perseus-Pisces and infalling on the opposite side of the sky. The residuals (bottom panel) assume negative values in almost all the sky, except in a small patch close of the South Galactic Pole where they roughly vanish. The minimum value of residuals is -400 km s^{-1} ($l \approx 310°$, $b \approx 0°$).

5.5.2 Velocity Multipoles

As was elegantly shown by Nusser & Davis (1994), the monopole ($l = 0$) and dipolar ($l = 1$) components of the radial peculiar velocity field, in the LG frame, are determined uniquely by specifying that the velocity should vanish at the origin. That is, the radial velocity at redshift **s**, when expanded in spherical harmonics to $l \leq 1$, is insensitive to the distribution of objects outside a sphere of radius s, where $s \equiv |\mathbf{s}|$. Thus a statistically significant disagreement between *PSCz* and the 1.2-Jy surveys predictions is a sign that there is something wrong or an incorrect treatment of some important non–linear flow or a systematic error in one or both datasets.

Our 1.2-Jy predictions for the various multipoles are similar to those by Baker *et al.* (1998). The monopole terms, $u_{00}(s)$, of both surveys are illustrated in Fig. 5.8. Heavy thick and thick dashed lines represent *PSCz* and 1.2-Jy, respectively. Although the inferred monopoles show the same features – three major turns at s$\approx$ 1 500, 4 000 and 6 000 km s^{-1} associated with Virgo/Fornax, the "Great-Attractor" and Perseus-Pisces, respectively – they are systematically different. The *PSCz* estimate is always negative within 12 000 km s^{-1} with a minimum value of -180 km s^{-1} at 2 000 km s^{-1}. The 1.2-Jy counterpart has an amplitude smaller that 50 km s^{-1} beyond 3 000 km s^{-1} and a minimum value of -100 km s^{-1} at $s \approx 1500$ km s^{-1}.

Fig. 5.9 displays the inferred dipole components. Solid thick and thick dashed lines represent *PSCz* and 1.2-Jy respectively. The *PSCz*' Y-component (top right panel of Fig. 5.9) agrees rather well with the 1.2-Jy component. The predicted X- and Z- components (top left and bottom right panels of the figure) respectively, show slight discrepancies, with the *PSCz* estimate being systematically smaller. Beyond $s \approx 6\,000$ km s^{-1}, the total amplitudes (bottom left panel) reflect such differences with *PSCz* having a smaller amplitude than the 1.2–Jy prediction. This discrepancy, along with the systematically negative value of the monopole mode within $s \approx 6\,000$ km s^{-1}, suggests in the *PSCz* redshift survey there

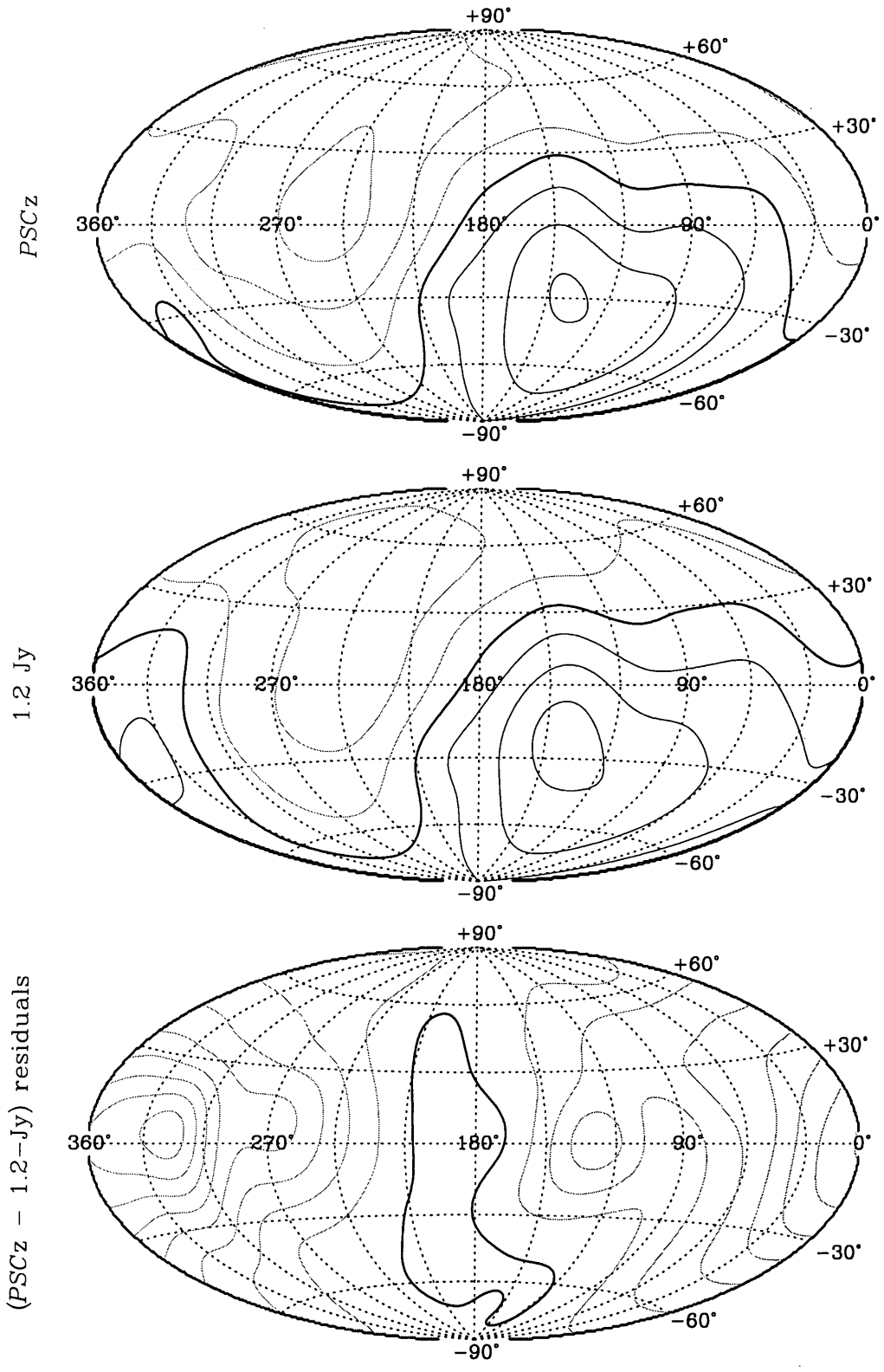

Figure 5.6: *IRAS* velocity field in a shell at $3\,000\,\mathrm{km\,s^{-1}}$. The contour spacing is $200\,\mathrm{km\,s^{-1}}$ and $50\,\mathrm{km\,s^{-1}}$ in the two top panels and bottom panel, respectively. The heavy black solid line represents the $u = 0$ or $u_{res} = 0$ contour.

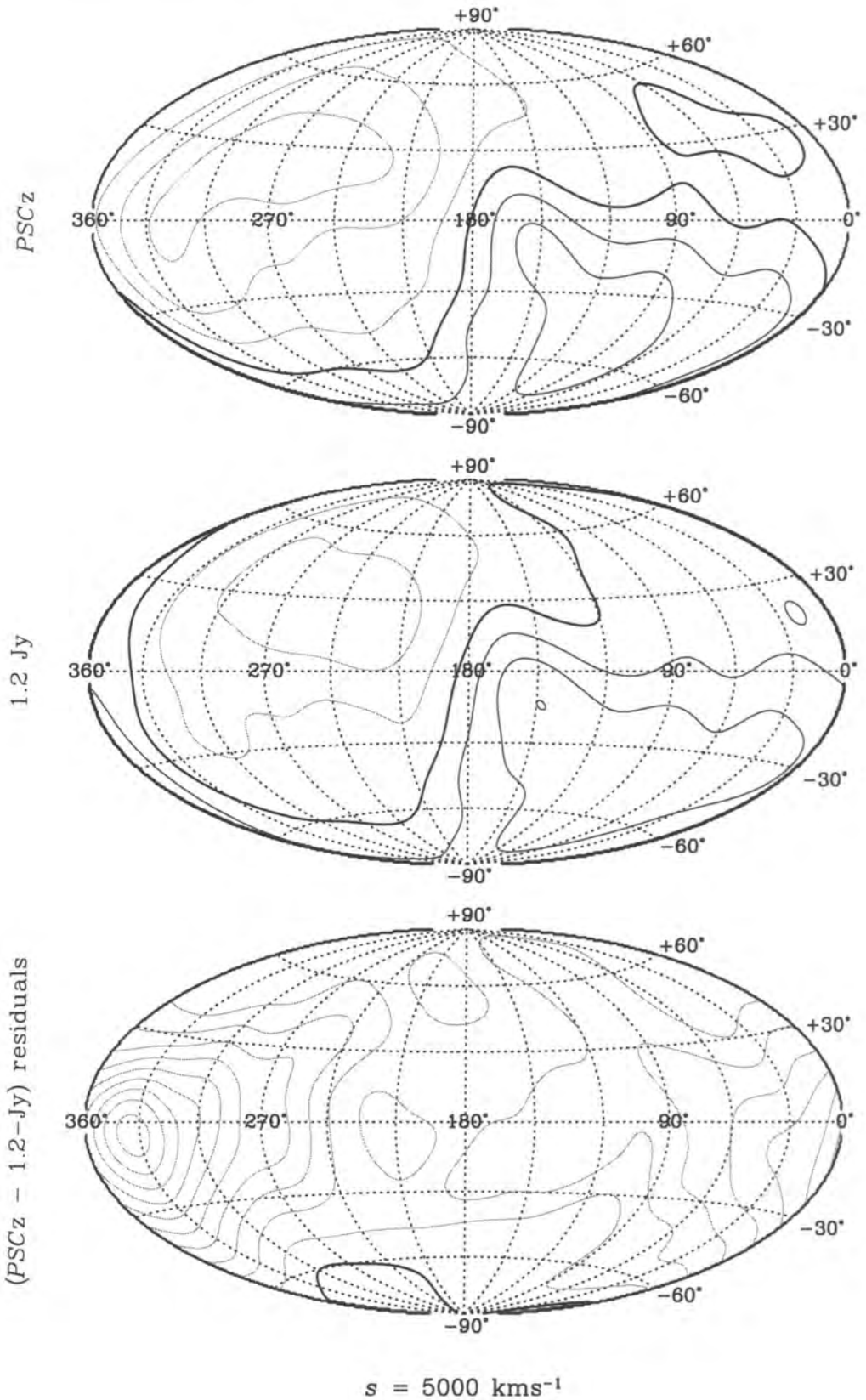

Figure 5.7: *IRAS* velocity field in a shell at $5\acute{0}00\,\mathrm{km\,s^{-1}}$.The contour spacing is $200\,\mathrm{km\,s^{-1}}$ and $50\,\mathrm{km\,s^{-1}}$ in the two top panels and bottom panel, respectively. The heavy black solid line represents the $u = 0$ or $u_{res} = 0$ contour.

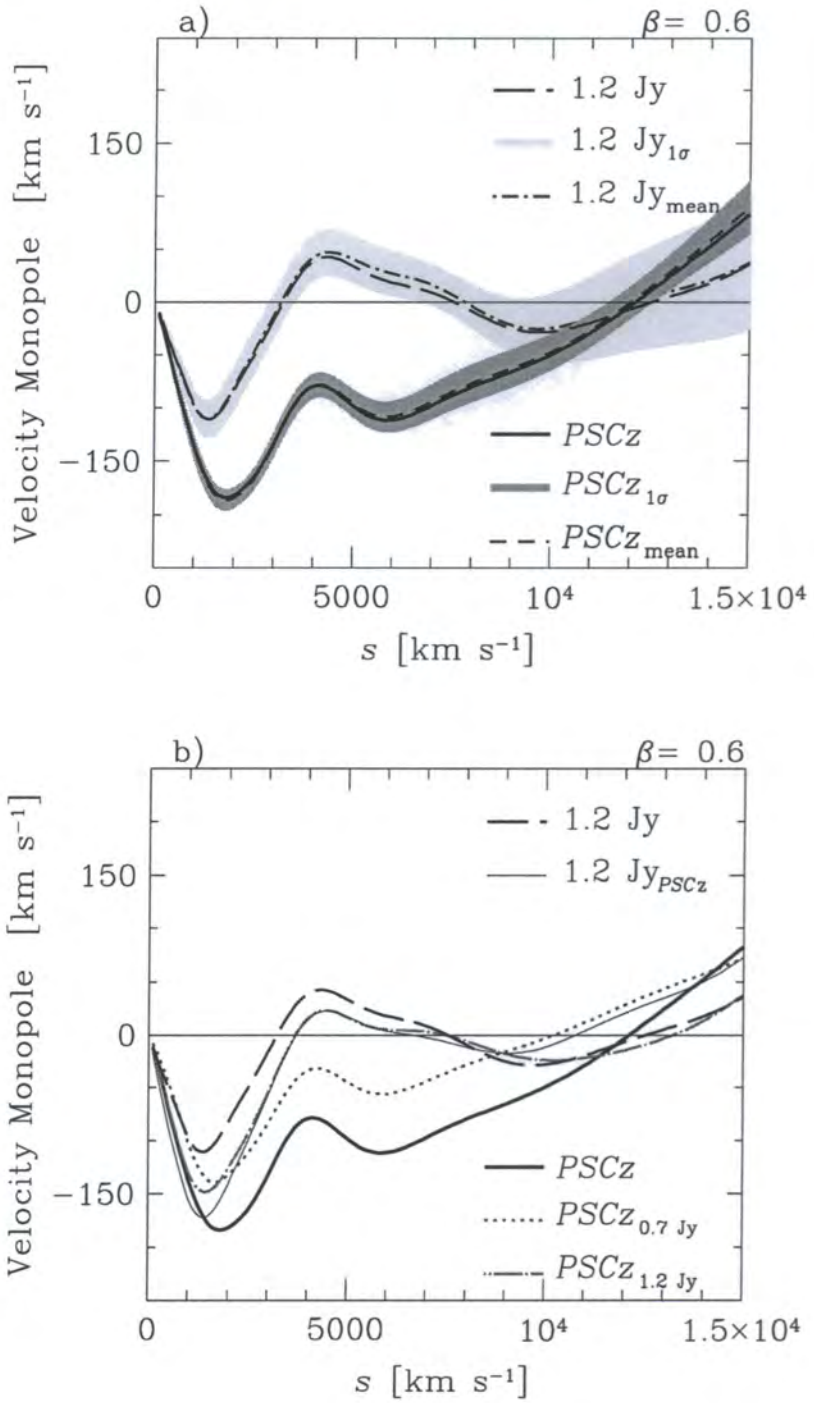

Figure 5.8: Monopole coefficient $u_{00}(s)$ estimated from *PSCz* and 1.2-Jy for $\beta = 0.6$. On both panels thick long-dashed (heavy solid) lines represent 1.2-Jy (*PSCz*) monopole modes of the velocity field. a) Dot-dashed and dashed lines give the mean of the monopole term in 20 Monte-Carlo bootstrap resampling realizations of the *PSCz* and 1.2-Jy surveys, respectively. Light- and Dark- shaded regions indicate the 1.2 Jy and *PSCz* $1-\sigma$ errors about $\bar{U}_{00}(s)$, respectively. b) Dotted, dot-dashed and solid lines represent *PSCz* $_{0.7}$, *PSCz* $_{1.2}$ and 1.2-Jy$_{PSCz}$, respectively.

is an excess of galaxies in the direction opposite to the Galactic centre, $l = 180°$.

Davis, Nusser & Willick (1996) were not able to obtain a conclusive value for β from their comparison between 1.2-Jy predicted and *Mark*III measured velocity fields because there is a clear mismatch between the Y-components of the velocity fields in question: the *IRAS* 1.2-Jy survey predicts a substantial reflex dipole while in the measured *Mark*III catalogue little is detected (see Fig 15 of Davis, Nusser & Willick 1996). Since the inferred Y-components in the 1.2-Jy and *PSCz* cases are very similar, the use of the *PSCz* would not ameliorate such a discrepancy.

Fig. 5.10 shows the quadrupole components, $u_{2m}(s)$ (where $m = -2, ..., 2$), inferred from both surveys. The $m = \pm 1$ components are in excellent agreement in both surveys while for $m = 0$ there is an evident disagreement as beyond Virgo ($s \approx 1\,800\,\mathrm{km\,s^{-1}}$) the *PSCz* prediction assumes the largest value of the two. The predicted $m = 2$ ($m = -2$)-components are very alike in both surveys within $s \approx 6\,000\,\mathrm{km\,s^{-1}}$. Beyond this redshift the 1.2-Jy prediction becomes slightly smaller than the *PSCz* estimate.

5.5.3 Estimating the Shot Noise Uncertainty

A possible source of discrepancy between the multipole terms inferred from both *IRAS* surveys are Poissonian fluctuations caused by discreteness, the so-called shot noise. We compute the shot noise uncertainty in the various multipoles by generating 20 bootstrap realizations of the "observed" *PSCz* and 1.2-Jy surveys by replacing each "observed" galaxy (including the "synthetic" galaxies within the masked regions) with a number of points drawn from a Poissonian distribution with the mean set equal to one and place them at the same location. We then obtain the peculiar velocity fields by applying the same algorithm used to predict the surveys' velocity fields.

Since the resampling realizations are performed at random, each of the p resampled datasets will have the same spherical coefficients as the original data. More precisely, if $\mathcal{U}^i_{lm}(s)$ is the $lm-$spherical coefficient for the i^{th} bootstrap sample, then the average value over our suite of bootstrap realizations:

$$\bar{\mathcal{U}}_{lm}(s) = \frac{1}{p}\sum_{i=1}^{p}\mathcal{U}^i_{lm}(s), \tag{5.10}$$

will tend asymptotically to the estimate inferred from the true dataset in the limit $p \to \infty$. The variance of the individual $\mathcal{U}^i_{lm}(s)$ about their mean value $\bar{\mathcal{U}}_{lm}(s)$ is an estimate of the internal variance

$$\sigma^2_{\bar{\mathcal{U}}_{lm}}(s) = \frac{1}{1+p}\sum_{i=0}^{p}\left[\mathcal{U}^i_{lm}(s) - \bar{\mathcal{U}}_{lm}(s)\right]^2. \tag{5.11}$$

The amplitude of the l-multipole $\bar{\mathcal{U}}_l(s)$ is then defined by the sum in quadrature over the

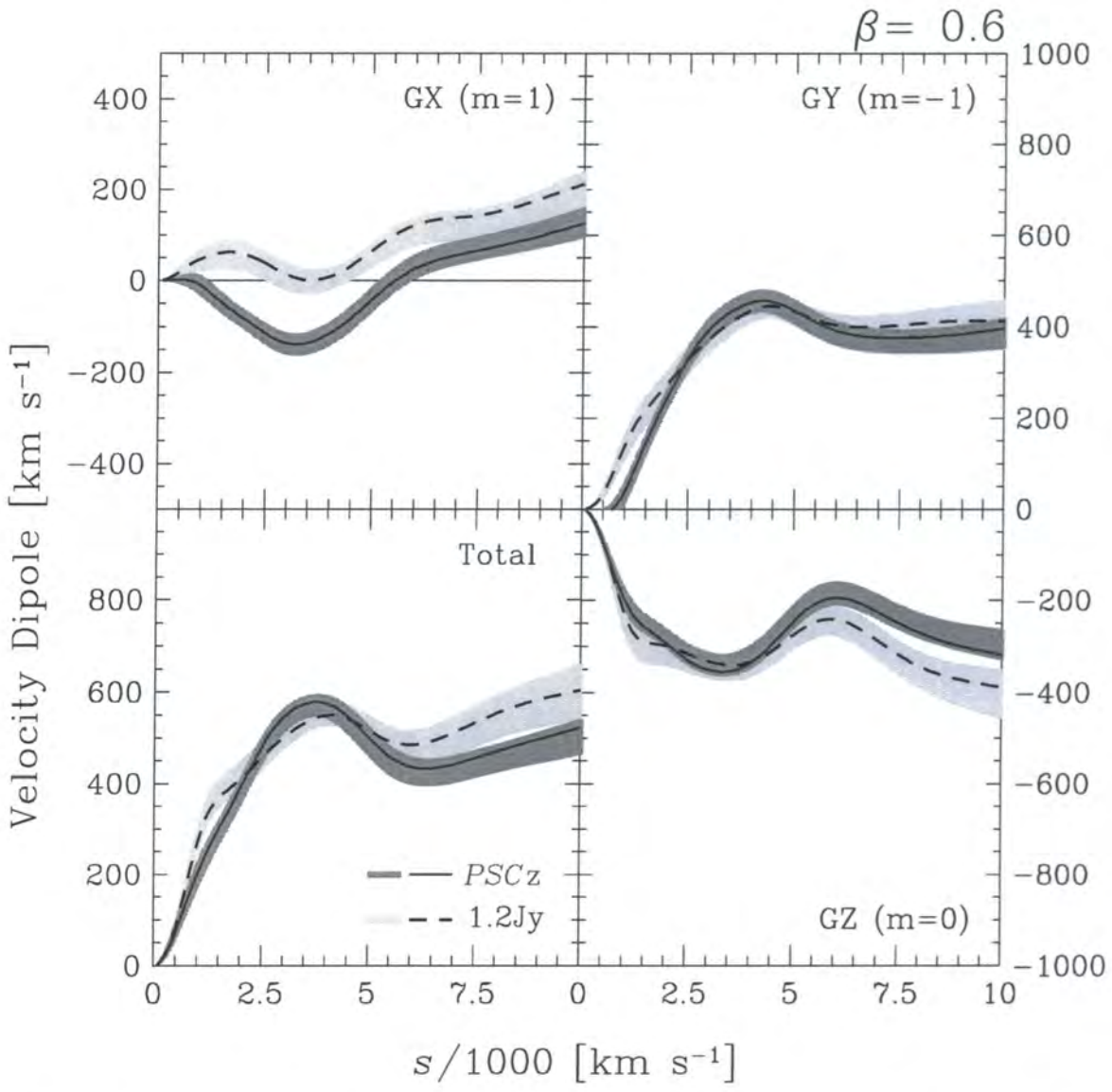

Figure 5.9: The dipole coefficients, $u_{1m}(s)\{m = -1, 0, 1\}$, inferred from *PSCz* and 1.2-Jy for $\beta = 0.6$. The solid and dashed lines in the various panels represent *PSCz* and 1.2-Jy dipoles, respectively. The *GX*, *GY*, *GZ* panels show the three Galactic components of the dipole and the bottom left is their quadrature sum. Light- and Dark- shaded regions indicate the 1.2 Jy and *PSCz* $1-\sigma$ errors about $\bar{u}_{1m}(s)\{m = -1, 0, 1\}$, respectively.

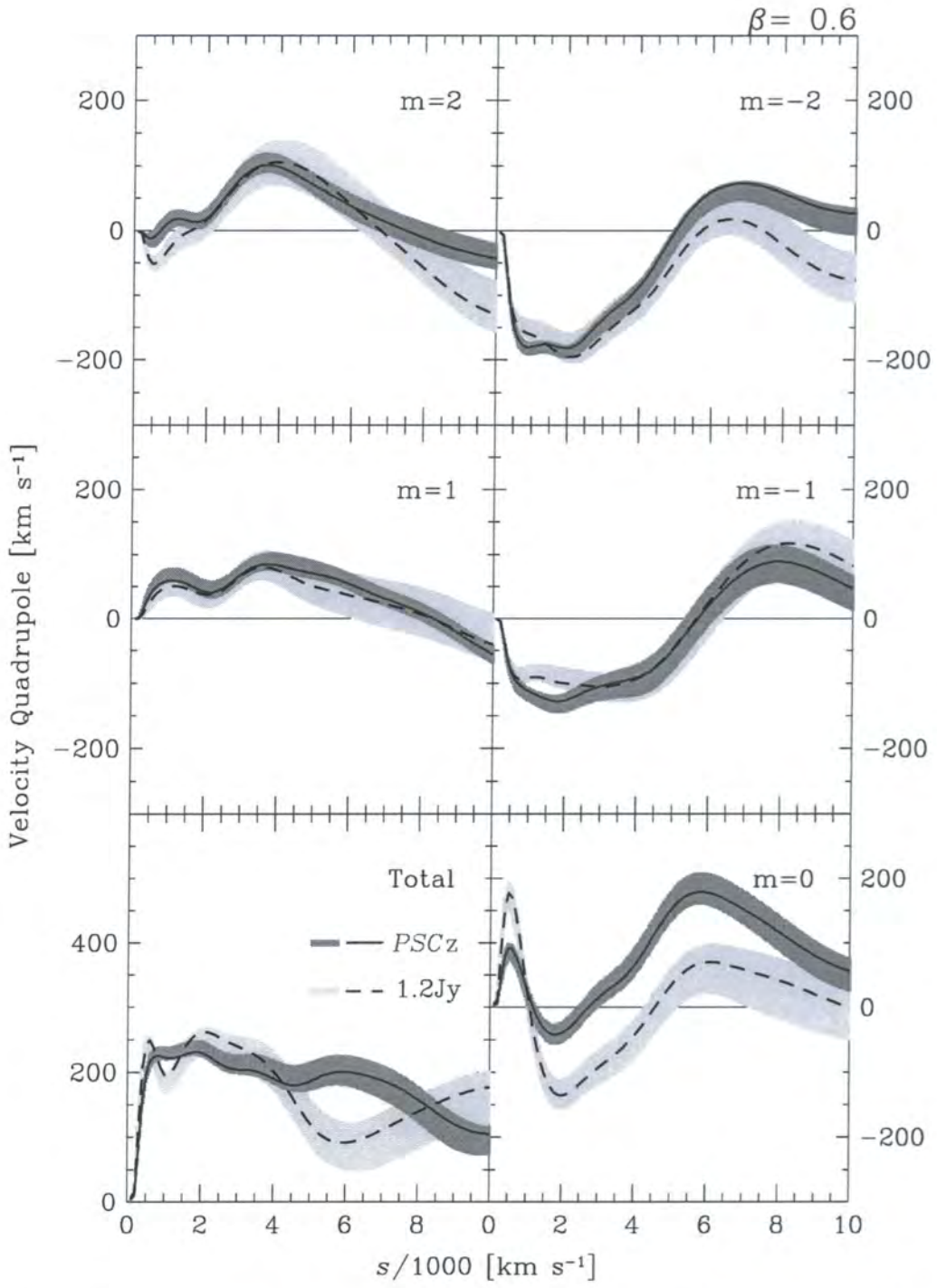

Figure 5.10: Quadrupole coefficients $u_{2m}(s)\{m = -2, ..., 2\}$ derived from *PSCz* and 1.2-Jy for $\beta = 0.6$. The solid and dashed lines in the various panels represent the *PSCz* and 1.2-Jy. The $m = -2, ..., 2$, panels show the five Galactic components of the quadrupole and the bottom left is their quadrature sum. Light- and Dark- shaded regions indicate the 1.2 Jy and *PSCz* $1 - \sigma$ errors about $\bar{u}_{2m}(s)\{m = -2, ..., 2\}$, respectively.

Table 5.1: Selection function parameters for eqn. (4.1)

Subsample	α	β	r_s $[h^{-1}\mathrm{Mpc}]$	$r_\star$ $[h^{-1}\mathrm{Mpc}]$	$\bar{n}$ $[h^3\mathrm{Mpc}^{-3}]$
PSCz	0.54	1.80	6.0	87.00	$5.76 \cdot 10^{-2}$
PSCz $_{0.7}$	0.57	1.80	6.0	79.71	$6.37 \cdot 10^{-2}$
PSCz $_{1.2}$	0.43	1.86	6.0	50.40	$4.54 \cdot 10^{-2}$
1.2-Jy	0.43	1.86	6.0	50.60	$4.64 \cdot 10^{-2}$
1.2-Jy $_{PSCz}$	0.43	1.86	6.0	50.40	$4.59 \cdot 10^{-2}$

$(2l+1)$- $\bar{U}^i_{lm}$'s, where $\{m = -l, ..., l\}$, and the total variance about $\bar{U}_l(s)$ is given by:

$$\sigma^2_{\bar{U}_l}(s) = \frac{1}{\bar{U}^2_l(s)} \left[\sum_{m=-l}^{m=l} \bar{U}^2_{lm}(s) \sigma^2_{\bar{U}_{lm}}(s) \right] \tag{5.12}$$

In Fig. 5.8a we illustrate $\bar{U}_{00}(s)$ inferred from the *PSCz* and 1.2-Jy bootstrap realizations (dashed and dot-dashed lines, respectively) and they are in excellent agreement with the monopole components computed from the redshift surveys. In the same figure we also show the $1-\sigma$ error of $\bar{U}_{00}(s)$: light- and dark- shaded regions represent the 1.2-Jy and *PSCz*, respectively. It is evident that the mismatch between both surveys' monopoles cannot be explained by shot noise.

Figs. 5.9 and 5.10 we illustrate the $1-\sigma$ error about the respective mean values for the two surveys. However, with the sake of simplicity we do not display $\bar{U}_{lm}(s)$ $\{l = 1, 2;\ m = -l, .., l\}$ inferred from the bootstrap realizations. Light- and dark- shaded regions indicate the 1.2-Jy and *PSCz*, respectively. As for the monopole term of the velocity field, the discrepancies for the higher moments cannot be explained by uncertainties due to shot noise.

5.5.4 Effects of Flux limit.

In this subsection we attempt to verify whether the velocity monopole predicted from the *PSCz* redshift survey is robust as we reconstruct the velocity field from subsamples whose flux limits are 0.7- and 1.2- Jy. To determine the selection function of our sub-datasets (*PSCz* $_{0.7}$ and *PSCz* $_{1.2}$, respectively) we use the same parametric maximum likelihood method applied in § 3 and § 4 (Yahil *et al.* 1991). The calculated parameters are displayed in Table (5.1). We compute the mean density within spheres of $s_{\max} = 8000$ and $s_{\max} = 10\,000\,\mathrm{km\,s^{-1}}$. Recall that to compute the mean number density of a survey we consider all galaxies within the radius for which the interparticle separation is the same as the 1.2-Jy at $s = 8\,000\,\mathrm{km\,s^{-1}}$. The velocity monopoles inferred from these two sub-

datasets are illustrated in Fig. 5.8b by dotted and long-dashed lines, respectively. They become gradually more like with 1.2-Jy prediction as we rise the value of the flux limit (dotted and dot-dashed lines). The largest disagreement between the $PSCz_{1.2-Jy}$ and the actual 1.2-Jy monopoles is at $s = 1\,500\,\mathrm{km\,s^{-1}}$ where the difference is $\sim 40\,\mathrm{km\,s^{-1}}$. This difference can be eliminated if we "observe" the 1.2-Jy survey through the same mask as *PSCz* and fill-in the unsurveyed regions with the prescription described in § 3. We then obtain a monopole term for the velocity field which agrees rather well with the 1.2-Jy data within $1\,000\,\mathrm{km\,s^{-1}}$ (thin solid line). In the calculation of the last velocity field we are assuming that the selection function of the initial 1.2-Jy data-set is still valid (see 5.1).

5.6 Discussion, Conclusions and Future Work

We have compared the velocity and overdensity fields of the recently completed *PSCz* survey and the shallower 1.2-Jy data set of *IRAS* galaxies in redshift-space. Our reconstructions are based on the assumptions that the Zeld'ovich approximation describes the growth of the large scale structure and that the galaxy distribution traces the underlying mass distribution according to the linear biasing prescription.

We have applied the algorithm introduced by Nusser & Davis (1994) to obtain the multipolar components and infer the maps of overdensity and radial peculiar velocity fields in redshift space.

The overdensity fields are reconstructed with a smoothing proportional to the 1.2-Jy inter-galaxy separation. The two redshift surveys exhibit the same major peaks (Virgo, Hydra-Centaurus and Perseus-Pisces). However, the $\langle\delta\rangle > 0$ of the *PSCz* sample is slightly larger than the 1.2-Jy counterparts. More specifically, we show that within $6\,000\,\mathrm{km\,s^{-1}}$ the *PSCz* overdensity field has a systematically larger monopole component than the 1.2-Jy counterpart.

The overall radial velocity field in the LG frame has a dipole-like appearance, with galaxies flowing away from us towards Perseus-Pisces and infalling in the opposite part of the sky in both surveys. The maps of the velocity residuals are on average negative within $s \approx 6000\,\mathrm{km\,s^{-1}}$ showing that the *PSCz* survey predicts a larger infall than the 1.2-Jy survey.

The velocity spherical harmonics analysis clearly shows a discrepancy between the monopole components of the velocity fields (as expected from the discrepancy in the density monopole). The 1.2-Jy estimate is systematically larger than the *PSCz* counterpart within $s \approx 10\,000\,\mathrm{km\,s^{-1}}$. The higher order moments exhibit good agreement within the same region, except u_{11} and u_{20} which show discrepancies of $100\,\mathrm{km\,s^{-1}}$ beyond $s = 1500\,\mathrm{km\,s^{-1}}$.

We have paid particular attention to the estimation of the shot noise uncertainties. In § 5.5.3 we show that uncertainties due to shot-noise cannot explain the discrepancies between the velocity multipoles of the two surveys.

If incompleteness of the *PSCz* galaxies fainter than 0.7 Jy can explain the mismatch between the velocity monopoles of the surveys then this estimator inferred from the *PSCz* $_{0.7}$ would be in good agreement with the 1.2-Jy counterpart. In Fig. 5.8b) we show that this is not the case (dotted line). We also demonstrate, in the same figure, that not even the *PSCz* $_{1.2}$ resolves such a discrepancy(dot-dashed line). The *PSCz* $_{1.2}$ monopole term of the velocity field only agrees with the 1.2-Jy estimate if this sample is masked with a *PSCz*-like mask (*cf.* Fig. 5.8b, thin solid line).

A better understanding of the mismatch between the monopoles of the two surveys will require a careful comparison between *PSCz* and 1.-Jy mock catalogues. This will allow us to access the importance of the systematic errors.

Davis, Nusser and Willick (1996) found discrepancies between the *SGY*-components of the 1.2-Jy and *Mark*III dipoles. Such discrepancies are not resolved because the *SGY*-component, of the *PSCz* and 1.2-Jy redshift surveys are very similar.

Bibliography

Abell, G.: 1958, *ApJS* **3**, 211

Abell, G., Corwin, H., and Olowin, R.: 1989, *ApJS* **70**, 1

Adler, R.: 1981, *The Geometry of Random Fields*, (New York: Wiley)

Andrews, H. and Hunt, B.: 1977, *Digital Image Restoration*, (Englewood Cliffs, NJ: Pretence-Hall)

Babul, A., Weinberg, D., Dekel, A., and Ostriker, J.: 1994, *ApJ* **427**, 1

Bahcall, N. and Soneira, R.: 1983, *ApJ* **270**, 20

Baker, J., Davis, M., Strauss, M., Lahav, O., and Santiago, B.: 1998, *astro-ph/9802713/*

Balkowski, C. and Kraan-Korteweg, R.: 1994, in *ASP Conf. Ser. 67: Unveiling Large-Scale Structures Behind the Milky Way*

Bardeen, J., Bond, J., Kaiser, N., and Szalay, A.: 1986, *ApJ* **304**, 15

Bardeen, J., Steinhardt, P., and Turner, M.: 1983, *Phys. Rev. D* **28**, 679

Baugh, C.: 1996, *MNRAS* **280**, 267

Bernardeau, F.: 1992, *ApJ* **390**, L15

Bernardeau, F., Chodorowski, M., Lokas, E., Stompor, R., and Kudlicki, A.: 1999, *MNRAS* submitted, *astro-ph/9901057*

Bertschinger, E. and Dekel, A.: 1989, *ApJ* **336**, L5

Branchini, E., Plionis, M. Zehavi, I., and Dekel, A.: 1997, *submitted*

Branchini, E. and Plionis, M.: 1996, *ApJ* **460**, 569

Branchini, E., Teodoro, L., Schmoldt, I., Frenk, C., and Efsthatiou, G.: 1998, *in preparation*

Brown, M. and Peebles, P.: 1987, *ApJ* 317

Bunn, E. F.: 1995, *Ph.D. thesis*, (Berkeley: University of California)

Cole, S., Fisher, K., and Weinberg, D.: 1994, *MNRAS* **267**, 785

Cole, S., Hatton, S., Weinberg, D. H., and Frenk, C. S.: 1998, *MNRAS* **submitted**, astro

Cole, S., Weinberg, D. H., Frenk, C. S., and Ratra, B.: 1997, *MNRAS* **289**, 37

Coles, P.: 1993, *MNRAS* **262**, 1065

Coles, P. and Lucchin, F.: 1995, *Cosmology. The origin and evolution of cosmic structure*, (Chichester: Wiley)

Cornish, N., Spergel, D., and Starkman, G.: 1998, *Classical Quantum Gravity* **15**, 2657

Couchman, H.: 1991, *ApJ* **368**, L23

da Costa, L., Freudling, W., Wegner, G., Giovanelli, R., Haynes, M., and Salzer, J.: 1996, *ApJ* **468**, L5

Davis, M., Efstathiou, G., Frenk, C., and White, S.: 1985, *ApJ* **292**, 371
Davis, M. and Huchra, J.: 1982, *ApJ* **254**, 437
Davis, M., Nusser, A., and Willick, J.: 1996, *ApJ* **473**, 22
Davis, M. and Peebles, P.: 1983, *ARA&A* **21**, 109
Davis, M., Strauss, M., and Yahil, A.: 1991, *ApJ* **372**, 394
Dekel, A.: 1994, *ARA&A* **32**, 371
Dekel, A.: 1997, *IAU Symposia* **183**, E11
Dekel, A., Bertschinger, E., and Faber, S. M.: 1990, *ApJ* **364**, 349
Dekel, A., Bertschinger, E., Yahil, A., Strauss, M. A., Davis, M., and Huchra, J. P.: 1993, *ApJ* **412**, 1
Dekel, A., Eldar, A., Kolatt, T., Yahil, A., Willick, J. A., Faber, S. M., Courteau, S., and Burstein, D.: 1998b, *submitted astro-ph/9812197*
Dekel, A. and Lahav, O.: 1998a, *submitted astro-ph/9812193*
Djorgovski, S. and Davis, M.: 1987, *ApJ* **313**, 59
Dressler, A.: 1980, *ApJ* **236**, 351
Dressler, A.: 1988, *ApJ* **329**, 519
Dressler, A., Lynden-Bell, D., Burstein, D., Davies, R., Faber, S. M., Terlevich, R., and Wegner, G.: 1987, *ApJ* **313**, 42
Eke, V., Cole, S., and Frenk, C.: 1996, *MNRAS* **282**, 263
Faber, S. and Jackson, R.: 1976, *ApJ* **20**, 668
Fisher, K., Huchra, J., Strauss, M., Davis, M., Yahil, A., and Schlegel, D.: 1995a, *ApJS* **100**, 69
Fisher, K., Lahav, O., Hoffman, Y., Lynden-Bell, D., and Zaroubi, S.: 1995b, *MNRAS* **272**, 219
Freudling, W., da Costa, L., and Pellegrini, P.: 1994, *MNRAS* **268**, 493
Giavalisco, M., Mancinelli, B., Mancinelli, P., and Yahil, A.: 1993, *ApJ* **411**, 9
Giovanelli, R., Haynes, M., Herter, T., Vogt, N., da Costa, L., Freudling, W., J.J.Salzer, and Wegner, G.: 1997b, *AJ* **113**, 53
Giovanelli, R., Haynes, M., Herter, T., Vogt, N., Wegner, G., Salzer, J., da Costa, L., and Freudling, W.: 1997a, *AJ* **113**, 22
Giovanelli, R. *et al.*: 1998, *in preparation*
Gramann, M.: 1993a, *ApJ* **405**, 449
Gramann, M.: 1993b, *ApJ* **405**, L47
Guzzo, L., Strauss, M. A., Fisher, K. B., Giovanelli, R., and Haynes, M. P.: 1997, *ApJ* **489**, 37
Han, M. and Mould, J.: 1990, *ApJ* **360**, 448
Heath, D. J.: 1977, *MNRAS* **179**, 351
Hudson, M.: 1993a, *MNRAS* **265**, 43
Hudson, M.: 1993b, *MNRAS* **265**, 72
Hudson, M.: 1994b, *MNRAS* **266**, 475
Hudson, M., Dekel, A., Courteau, S., Faber, S., and Willick, J.: 1995, *MNRAS* **274**, 305
Jackson, J.: 1962, *Classical Electrodynamics*, (New York: Wiley)

Kaiser, N.: 1984, *ApJ* **284**, L9

Kaiser, N.: 1987, *MNRAS* **227**, 1

Kaiser, N.: 1988, *MNRAS* **231**, 149

Kaiser, N., Efstathiou, G., Ellis, R., Frenk, C., Lawrence, A., Rowan-Robinson, M., and Saunders, W.: 1991, *MNRAS* **252**, 1

Kaiser, N. and Lahav, O.: 1989, *MNRAS* **237**, 129

Kaiser, N. and Stebbins, A.: 1991, in D.Latham and N. da Costa (eds.), *Large Scale Scructure ans Motions in the Universe* , p. 111, (San Francisco: Ast. Soc. Pacif. Conf. Ser.)

Kibble, T.: 1985, *Nucl. Phys. B, Part. Phys.* 227

Kogut, A., Banday, A. J., Bennett, C. L., Gorski, K. M., Hinshaw, G., Smoot, G. F., and Wright, E. I.: 1996, *ApJ* **464**, L5

Kolatt, T., Dekel, A., Ganon, G., and Willick, J.: 1996, *ApJ* **458**, 419

Kolb, E. and Turner, M.: 1990, *The Early Universe*, (Reading, MA: Addison-Wesley)

Kraan-Korteweg, R. C., Koribalski, B., and Juraszek, S.: 1998, in R. Morganti and W. Couch (eds.), *Looking Deep in the Southern Sky, astro-ph/9804066*

Kraan-Korteweg, R. C., Woudt, P. A., Cayatte, V., Fairall, A. P., Balkowski, C., and Henning, P. A.: 1996, *Nat* **379**, 519

Lahav, O., Fisher, K., Hoffman, Y., Scharf, C., and Zaroubi, S.: 1994, *ApJ* **423**, L93

Lahav, O., Lilje, P., Primack, J., and Rees, M.: 1991, *MNRAS* **251**, 128

Lauer, T. and Postman, M.: 1994, *ApJ* **425**, 418

Lightman, A. P. and Schechter, P. L.: 1990, *ApJS* **74**, 831

Lineweaver, C. H., Tenorio, L., Smoot, G. F., Keegstra, P., Banday, A. J., and Lubin, P.: 1996, *ApJ* **470**, 38

Lynden-Bell, D., Faber, S., Burstein, D., Davies, R., Dressler, A., Terlevich, R., and Wegener, G.: 1988, *ApJ* **326**, 19

Mo, H. J. and White, S. D. M.: 1996, *MNRAS* **282**, 347

Moscardini, L., Matarrese, S., Lucchin, F., and Messina, A.: 1991, *MNRAS* **248**, 424

Narayanan, V. K. and Weinberg, D.: 1998, *ApJ* **508**, 440

Nusser, A. and Davis, M.: 1994, *ApJ* **421**, L1

Nusser, A. and Davis, M.: 1995, *MNRAS* **276**, 1391

Nusser, A. and Dekel, A.: 1992, *ApJ* **391**, 443

Nusser, A. and Dekel, A.: 1993, *ApJ* **405**, 437

Nusser, A., Dekel, A., Bertschinger, E., and Blumenthal, G.: 1991, *ApJ* **379**, 6

Paczyncki, B. and Piran, T.: 1990, *ApJ* **364**, 341

Padmanabhan, T.: 1993, *Structure Formation inthe Universe*, (Cambridge: Cambrige University Press)

Peacock, J. and Dodds, S.: 1994, *MNRAS* **267**, 1020

Peacock, J. and Heavens, A.: 1985, *MNRAS* **217**, 805

Peacock, J. A., Heavens, A. F., and Davies, A. T.: 1990, in *Proceedings of the 36th Scottish Universities Summer School in Physics, Edingburgh, July 24 - August 11, 1989, Bristol: IOP Publication Adam Hilger, 1990, edited by Peacock, John A.; Heavens, Alan F.;*

Davies, Andrew T.

Peebles, P.: 1980, *The Large Scale Structure of the Universe*, (Princeton: Princeton Univ. Press)

Peebles, P.: 1988, *PASP* **100**, 670

Peebles, P.: 1989, *ApJ* **344**, L53

Peebles, P.: 1990, *ApJ* **362**, 1

Peebles, P.: 1993, *Principles of Physical Cosmology*, (Princeton: Princeton University Press)

Peebles, P.: 1994, *ApJ* **429**, 43

Peebles, P. J. E.: 1982, *ApJ* **258**, 415

Plionis, W. *et al.*: 1999, *in preparation*

Riess, A., Press, W., and Kirshner, R.: 1995, *ApJ* **438**, L17

Rowan-Robinson, M., Lawrence, A., Saunders, W., Crawford, J., Ellis, R., Frenk, C., Parry, I., Xiaoyang, X., Allington-Smith, J., Efstathiou, G., and Kaiser, N.: 1990, *MNRAS* **247**, 1

Rowen-Robinson, W. *et al.*: 1999, *in preparation*

Rubin, V. C. and Coyne, G. V.: 1988, in *Large Scale Motions in the Universe: A Vatican Study Week*, p. 624, (Princeton, NJ: Princeton University Press)

Rybicki, G. and Press, W.: 1992, *ApJ* **398**, 169

Sahni, V. and Coles, P.: 1995, *Phys. Rept.* **262**, 1

Santiago, B., Strauss, M., Lahav, O., Davis, M., Dressler, A., and Huchra, J.: 1995, *ApJ* **446**, 457

Santiago, B., Strauss, M., Lahav, O., Davis, M., Dressler, A., and Huchra, J.: 1996, *ApJ* **461**, 38

Saunders, W., Oliver, S., Keeble, O., Rowan-Robinson, M., Canavezes, A., Maddox, S., Sutherland, W., Efstathiou, G., MCMahon, R., Springel, V., White, S., Tadros, H., Frenk, C., Branchini, E., Taylor, A., Ballinger, B., and Heavens, A.: 1998, in *Wide Field Surveys in Cosmology, 14th IAP meeting held May 26-30, 1998, Paris. Publisher: Editions Frontieres. ISBN: 2-8 6332-241-9*, p. 71

Saunders, W. *et al.*: 1999, *in preparation*

Schaeffer, R., Silk, J., Spiro, M., and Zinn-Justin, J.: 1996, in *ASP Conf. Ser. 24: Cosmology and Large-scale Structure in the Universe*

Schechter, P.: 1980, *AJ* **85**, 801

Schmoldt, I., Branchini, E., Teodoro, L., Efstathiou, G., Frenk, C., Saunders, W., Sutherland, W., Rowan-Robinson, M., White, S., Oliver, S., Keeble, O., Maddox, S., and Tadros, H.: 1998, *MNRAS* accepted

Shaya, E., Peebles, P., and Tully, B.: 1994, in F. Bouchet and M. Lachiéze-Rey (eds.), *Cosmic Velocity Fields*, p. 393, (Gif-sur-Yvette: Editions Frontières)

Shaya, E., Peebles, P., and Tully, R.: 1995, *ApJ* **454**, 15

Shaya, E., Tully, R., and Pierce, M.: 1992, *ApJ* **391**, 16

Sigad, Y., Eldar, A., Dekel, A., Strauss, M., and Yahil, A.: 1998, *ApJ* **495**, 516

Springel, V. and White, S. D. M.: 1998, *MNRAS* **298**, 143

Stebbins, A.: 1994, in F. Bouchet and M. Lachiéze-Rey (eds.), *Cosmic Velocity Fields*, p. 253, (Gif-sur-Yvette: Editions Frontières)

Strauss, M.: 1997, in N. Turok (ed.), *Critical Dialogues in Cosmology*, p. 423, (Singapore: World Scientific)

Strauss, M., Cen, R., Ostriker, J., Lauer, T., and Postman, M.: 1995b, *ApJ* **444**, 507

Strauss, M. and Davis, M.: 1988, in V. Rubin and G. Coyne (eds.), *Large Scale Motions in the Universe: A Vatican Study Week*, p. 256, (Princeton, NJ: Princeton University Press)

Strauss, M., Davis, M., Yahil, A., and Huchra, J.: 1990, *ApJ* **361**, 49

Strauss, M., Davis, M., Yahil, A., and Huchra, J.: 1992, *ApJ* **385**, 421

Strauss, M. and Willick, J.: 1995a, *Phys. Rep.* **261**, 271

Strauss, M. A., Ostriker, J. P., and Cen, R.: 1998, *ApJ* **494**, 20

Sugiyama, N.: 1995, *ApJS* **100**, 281

Taylor, A. and Rowan-Robison, M.: 1993, *MNRAS* **265**, 809

Tegmark, M. and Bromley, B.: 1995, *ApJ* **453**, 533

Tully, R.: 1987, *ApJ* **321**, 280

Tully, R. and Fisher, J.: 1977, *A&A* **54**, 661

Vaucouleurs, G.: 1948, *Ann. d'Astrophisique* **11**, 247

Wagoner, R. V.: 1973, *ApJ* **179**, 343

Walker, T. P., Steigman, G., Kang, H., Schramm, D. M., and Olive, K. A.: 1991, *ApJ* **376**, 51

Watkins, R. and Feldman, H.: 1995, *ApJ* **453**, L73

Webster, M., Lahav, O., and Fisher, K.: 1997, *MNRAS* **287**, 425

Weinberg, D.: 1989, *Ph.D. thesis*, (Princeton: Princeton University)

Weinberg, D.: 1992, *MNRAS* **254**, 315

Weinberg, D.: 1994, in S. Maddox and A. Aragón-Salamanca (eds.), *Wide-Field Spectroscopy and the Distant Universe*, p. 129, (Singapore: World Scientific)

Weinberg, S.: 1972, *Gravitation and cosmology:Principles and applications of the general theory of relativity*, (New York: Wiley)

Wilkinson, D.: 1988, in J.Audouze, M.-C. Pelletan, and A.Slalay (eds.), *Large Scale Structures of the Universe, IAU Conference Symposium 130*, p. 7, (Dordrecht:Reidel)

Willick, J., Courteau, S., Faber, S., Burstein, D., and Dekel, A.: 1995, *ApJ* **446**, 12

Willick, J., Courteau, S., Faber, S., Burstein, D., Dekel, A., and Kolatt, T.: 1996, *ApJ* **457**, 460

Willick, J., Courteau, S., Faber, S., Burstein, D., Dekel, A., and Strauss, M.: 1997a, *ApJS* **109**, 333

Willick, J. and Strauss, M.: 1998, *ApJ* **507**, 64

Willick, J., Strauss, M., Dekel, A., and Kolatt, T.: 1997b, *ApJ* **486**, 629

Yahil, A., Strauss, M., Davis, M., and Huchra, J.: 1991, *ApJ* **372**, 380

Zaroubi, S., Hoffman, Y., and Dekel, A.: 1998, *submitted* astro-ph/9810279

Zaroubi, S., Hoffman, Y., Fisher, K., and Lahav, O.: 1995, *ApJ* **449**, 446

Zeldovich, Y. and Novikov, I.: 1983, *Relativistic Astrophysics Vol. 2*, (Chicago: Univ. of

Chicago Press)
Zeldovich, Y. B.: 1970, *A&A* **2**, 20